



Seismic plus energy upgrading of masonry buildings using advanced materials

Analysis of a combined structural and thermal retrofitting

Kouris, L., Bournas, D., Pohoryles, D., Valsamos, G.,
Savvas, T., Maduta, C.

2024



This document is a publication by the Joint Research Centre (JRC), the European Commission's science and knowledge service. It aims to provide evidence-based scientific support to the European policymaking process. The contents of this publication do not necessarily reflect the position or opinion of the European Commission. Neither the European Commission nor any person acting on behalf of the Commission is responsible for the use that might be made of this publication. For information on the methodology and quality underlying the data used in this publication for which the source is neither Eurostat nor other Commission services, users should contact the referenced source. The designations employed and the presentation of material on the maps do not imply the expression of any opinion whatsoever on the part of the European Union concerning the legal status of any country, territory, city or area or of its authorities, or concerning the delimitation of its frontiers or boundaries.

Contact information

Name: Dionysios Bournas

Address: Via E. Fermi, 2749, I-21027 Ispra (VA), Italy

Email: Dionysios.BOURNAS@ec.europa.eu

EU Science Hub

<https://joint-research-centre.ec.europa.eu>

JRC123617

EUR 30563 EN

PDF ISBN 978-92-76-28603-5 ISSN 1831-9424 doi:10.2760/66556

KJ-NA-30563-EN-N

Luxembourg: Publications Office of the European Union, 2024

© European Union, 2024



The reuse policy of the European Commission documents is implemented by the Commission Decision 2011/833/EU of 12 December 2011 on the reuse of Commission documents (OJ L 330, 14.12.2011, p. 39). Unless otherwise noted, the reuse of this document is authorised under the Creative Commons Attribution 4.0 International (CC BY 4.0) licence (<https://creativecommons.org/licenses/by/4.0/>). This means that reuse is allowed provided appropriate credit is given and any changes are indicated.

For any use or reproduction of photos or other material that is not owned by the European Union permission must be sought directly from the copyright holders.

How to cite this report: European Commission, Joint Research Centre, Kouris, L., Bournas, D., Pohoryles, D., Valsamos, G., Sawvas, T. and Maduta, C., *Seismic plus energy upgrading of masonry buildings using advanced materials*, Publications Office of the European Union, Luxembourg, 2024, <https://data.europa.eu/doi/10.2760/66556>, JRC123617.

Contents

Abstract.....	1
Foreword.....	2
Acknowledgements	3
1 Introduction.....	4
1.1 Problem statement and Review of Integrated Retrofitting in the Literature	4
1.2 Context of relevant EU policies.....	6
2 State-of-the-art on the experimental performance of the textile-reinforced mortar (TRM).....	7
2.1 Performance of TRM	7
2.2 In-plane performance of the hybrid system.....	8
2.3 Out-of-plane performance of the hybrid system.....	9
3 Homogenisation of masonry properties.....	11
3.1 Overview of homogenisation.....	11
3.2 Gradient elastic theory.....	12
3.3 Gradient homogenisation model (GREHM).....	14
3.3.1 Homogenised masonry elastic modulus E_v perpendicular to mortar bed joints (vertical).....	15
3.3.2 Homogenised masonry elastic modulus E_h parallel to mortar bed joints (horizontal).....	15
3.3.3 Homogenised masonry shear elastic modulus G	16
3.3.4 Homogenised masonry Poisson's ratios ν_{xy} and ν_{yx}	16
3.3.5 Normalised graphs for the estimation of the homogenised properties.....	17
3.4 Verification of the proposed homogenisation model.....	19
3.4.1 Comparison with numerical homogenisation models.....	19
3.4.2 Comparison with analytical homogenisation models	25
4 Numerical simulations and analyses of reinforced masonry with TRM.....	29
4.1 Implicit simulation of TRM reinforced masonry.....	29
4.1.1 Description of the model.....	29
4.1.1.1 Parameters of TRM layers	29
4.1.1.2 Parameters of masonry	31
4.1.2 Calibration of the model for out-of-plane loads.....	33
4.1.2.1 Calibration of masonry properties	33
4.1.2.2 Calibration of the textile bond behaviour.....	34
4.1.3 Empirical equations for the reduction coefficients.....	35
4.1.4 Analyses for out-of-plane quasi-static loads	38
4.2 Explicit simulation of TRM reinforced masonry.....	40
4.2.1 Parameters of the model.....	40
4.2.2 Calibration of the model	41
4.2.3 Analysis for dynamic loading from explosions.....	43
5 Assessment of the combined retrofitting in city scale.....	45

5.1	Studied cities and buildings' population.....	45
5.2	Energy performance.....	49
5.3	Seismic performance.....	52
5.4	Combined performance.....	55
6	Conclusions.....	58
	References.....	59
	List of abbreviations and definitions.....	68
	List of boxes.....	69
	List of figures.....	70
	List of tables.....	72

Abstract

Upgrading existing masonry buildings in the EU has become very important due to their poor performance during earthquakes resulting in significant human and economic losses, and on the other hand, their low energy performance which significantly increases their energy consumption. Therefore, a holistic approach with a concurrent seismic and energy retrofitting is necessary and has been explored in this project. Namely, SPEctRUM investigated a hybrid structural-plus-energy retrofitting solution to achieve cost effectiveness, which combines inorganic textile-based composites with thermal insulation systems for masonry building envelopes. Specifically, textile reinforced mortar (TRM) composites are used to reinforce unreinforced masonry (URM) buildings enhancing their seismic capacity, while thermal insulation is added to improve the buildings' energy performance. The EU policy context of energy efficiency and sustainability and safeguarding of cultural heritage is benefitted by the project as discussed in chapter 1.

Firstly in chapter 2, a thorough review of the experimental investigations applying textiles in inorganic mortars is carried out and conclusions are drawn regarding its efficiency. A substantial increase in the in-plane and the out-of-plane strength and displacement capacity can be seen in all the test campaigns despite the different expermental techniques and strengthening materials. Moreover, the hybrid composite material made of layers of TRM and thermal insulation was found advantageous and capable to fulfil its structural and energy targets if the various layers are carefully bonded.

Then, in chapter 3, numerical models and design solutions were developed to facilitate the application of the proposed system. The investigation in the first place focused on a new homogenisation model for masonry to reduce the complexity of the simulation. Indeed, in a retrofitted masonry wall there exist at least four different materials (masonry units, masonry mortar, strengthening mortar and textile) built in-situ with an internal structure which has many imperfections. Therefore, there are a lot of interaction levels and parameters which are not easily to predict in a micro-modelling approach. The homogenisation of masonry offers a viable solution to simplify masonry in one material. To this end, the proposed homogenisation model includes a gradient term to represent the internal structure of masonry. The proposed gradient elastic homogenisation model (GREHM) is furnished with easy-to-apply charts to simplify its application on masonry walls.

In the following chapter 4 the numerical modelling of the strengthened masonry with TRM is attempted. Two approaches for a detailed modelling are followed: (i) an implicit model for quasi-static loading and, (ii) an explicit model for dynamic loading. The former model includes the homogenised properties of masonry to limit the numerical cost of the analysis. Moreover, the interaction of the textile with the inorganic matrix is accounted for introducing in the model effective material properties with the aid of an empirical equation specifically designed for this aim. This empirical equation has been calibrated using an experimental campaign on the out-of-plane performance of masonry walls strengthened with TRM. It can distinguish between coated and uncoated textiles. Parametric investigations show that the capacity can be increased substantially even when less strong textiles from natural fibres are used. The explicit model on the contrary, is able to treat simulations with higher non-linearities and in this regard, a distinct simulation of masonry units and mortar joints was adopted. Based on this latter model the response of strengthened walls in blast loads has been investigated and it was found that TRM layers offer high safety from explosions for the occupants.

In Chapter 5, the cost effectiveness of the proposed retrofitting system has been explored in a large-scale investigation across various locations in Europe. A number of cities with different seismic risk and climatic conditions were selected and their building stock was investigated. The seismic hazard varies from low to high risk characterised by the expected PGA and the climatic conditions were classified into four zones (warm to cold) characterised by the heating degree-days. Then, archetype buildings, i.e. buildings with typical architectural and structural characteristics were defined and the building stock was classified in the respective categories. The renovation of the building population of the selected cities was examined assuming target annual renovation rates from 1 to 3%. Then, the payoff period was estimated. Relativley short payoff times have been found generally which decrease when high seismic risk combines with old masonry structures. Finally, the last chapter summarises the conclusions.

Foreword

This is the final report of the SPEctRUM project funded by Marie Skłodowska-Curie Actions concluding its main findings. This project has been inspired by the always more demanding need to upgrade the existing masonry EU buildings due to their poor seismic performance resulting in severe human and economic losses and their low energy performance which significantly increases their energy consumption. The issue of upgrading the unreinforced masonry (URM) buildings is of great importance since they are unengineered vernacular structures and far from the levels of the current standards for seismic capacity and energy consumption. Moreover, the latter combined with deterioration due to ageing of materials, environmental degradation, experience of several earthquakes and lack of maintenance, yield to even higher structural and energy deficiencies. Every recent moderate to high seismic shaking has caused damage ranging from cracks to partial or total collapse with a high death toll and economic loss. Therefore, this project aimed to confront both deficiencies in an integrated manner by exploring innovative techniques and advanced materials. The synergy of this project with the JRC institutional project iRESIST+ which focused on the upgrading of old RC buildings, tried to address the problem for the most common building typologies providing viable solutions in the context of EU regulations for energy savings of buildings and protection of cultural heritage.

A simultaneous seismic and energy retrofitting of the masonry building stock can be realised integrating advanced strengthening and insulating materials. In masonry buildings however, there are some more requirements for the set targets of the retrofitting apart from the structural and energy performance related to their traditional nature; these can be summarised in the reversibility and compatibility of the strengthening materials. Moreover, cost effectiveness remains an important aspect which should be added to them.

SPEctRUM explored a hybrid structural-plus-energy retrofitting solution which combines inorganic textile-based composites with thermal insulation systems for masonry building envelopes to meet all the aforementioned requirements. Analytical models and design solutions were developed to facilitate the investigation and the application of the proposed system. Parametric analyses showed that the capacity can be increased substantially with the use of various strength textiles. The cost efficiency of the combined retrofitting system was explored in a large-scale investigation across Europe and rather short payoff times were found especially in regions of moderate to high seismicity as those in the Mediterranean region.

Acknowledgements

The fund received from the Marie Skłodowska-Curie Actions - Individual Fellowships of the Call H2020-MSCA-IF for the project SPEctRUM (No. 799593) is gratefully acknowledged.

The kind help of Dr A Anthoine and Dr FA Kariou is thankfully acknowledged.

Authors

Leonidas Alexandros S. Kouris, Dionysios A. Bournas, Daniel A. Pohoryles

Georgios N. Valsamos, Savvas P. Triantafyllou, Carmen Maduta

1 Introduction

1.1 Problem statement and Review of Integrated Retrofitting in the Literature

Large parts of the built infrastructure need repair or strengthening due to ageing, rehabilitation, or obsolete design. The issue of upgrading the existing unreinforced masonry (URM) structures is of great importance and priority for all EU countries as most of them are unengineered vernacular structures. URM buildings suffer from low seismic capacity and high energy consumption. Moreover, the deterioration due to ageing of materials, environmental degradation, experience of several earthquakes and lack of maintenance, contribute to an evolving higher vulnerability and lower energy efficiency. Every moderate to high seismic shaking causes damage ranging from cracks to partial or total collapse with a high death toll and economic loss (Indirli et al., 2013; Penna et al., 2014b). In the Mediterranean region the existing masonry building stock is susceptible to a significant seismic hazard. Given that part of these URM buildings constitutes the famous EU built cultural heritage which is at a high stake and whole traditional settlements have been devastated in strong earthquakes (Kouris et al., 2010), their structural health monitoring and conservation (Rossi and Bourmas, 2023) comprises priority for the EU.

On the other hand, the low energy performance of masonry buildings increases their energy consumption which is mainly attributed to the no or low thermal insulation of their envelopes. At EU level, buildings consume 40% of energy and release 36% of related greenhouse gas (GHG) emissions, with most existing buildings built before energy efficiency standards were established. The Energy Performance of Buildings Directive (EPBD) fosters requirements to improve the energy performance of both new and existing buildings. The 2024 recast EPBD introduces minimum energy performance standards for non-residential buildings and mandates progressive renovation pathways for residential buildings, aiming for a zero-emission building stock by 2050 (European Commission, 2024). This goal can be particular challenging for older masonry buildings, as it may require significant investments in energy efficiency and on-site renewable technologies, which can be at risk due to natural hazards like earthquakes. While demolition and new construction might be considered sometimes, they are not fully in line with the EU's emphasis on resource efficiency and sufficiency principles (Maduta et al., 2022). Therefore, focusing on renovation is crucial for reducing vulnerability to hazards, reducing environmental impact, and improving indoor environmental quality in existing buildings. Renovation also supports job creation, boosts industry competitiveness, and strengthens energy security (Zangheri et al., 2020).

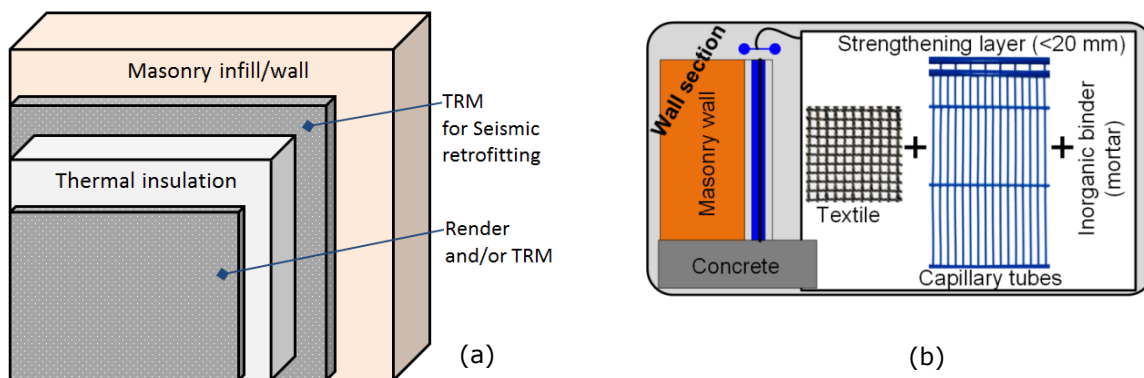
Extensive research has been carried out to upgrade URM structures in terms of strength and deformation capacity using composites as they cause minimum invasion. Numerous structures have been efficiently strengthened with fibre-reinforce polymers (FRP), which achieve sufficient bond with masonry substrates through an organic, commonly epoxy, agent e.g. (Bakis et al., 2002; Carozzi et al., 2017; Kreaikas and Triantafillou, 2005; Triantafillou, 1998). Despite the fact that force transfer is probably sufficiently secured if surfaces are adequately prepared, during actual application there are a series of disadvantages related to the epoxy adhesives:

- *Irreversibility*: polymeric resins cannot be detached without damaging masonry.
- *Damp incompatibility*: it is not possible to apply epoxies on humid surfaces whereas freeze problems may appear during application from isolated water.
- *Lack of vapour permeability*: organic resins are not vapour permeable, hence in a case of frescoes existing at the opposite side of the walls problems is possible to arise.
- *Thermal compatibility problems*: a different thermal coefficient with masonry substrate cause strain incompatibility; in addition, it is hard to employ epoxies at low temperatures.
- *Lack of fire resistance*: polymer composites cannot resist high temperatures.
- *Working and environmental hazard*: toxicity of epoxy resin can harm workers or, the environment when uncautiously worked.
- *High cost*: the cost of epoxies is relatively high.
- *Poor bond with rough masonry surfaces*: the substrate roughness and irregularity increase the workmanship cost and can cause a premature delamination and reduce the quality of the intervention.

The replacement of organic matrices with inorganic ones, that is the use of textile reinforced mortar (TRM) instead of FRP, offers an effective solution to the shortcomings listed above, especially for heritage structures, where the limited invasiveness and compatibility aspects are extremely important.

TRM jacketing has minimal, if any, thermal insulation capacity. Therefore, to tackle the problem of a concurrent seismic plus energy retrofitting, TRM can be combined with thermal insulation to form a structural-plus-thermal upgrading of existing buildings (Figure 1, (Bournas, 2018)). A wide range of internal and external insulations can achieve high energy savings together with a quick and easy application and low cost (Anastaselos et al., 2009). Various types of thermal insulation boards can be combined with TRM layers and used externally and internally, for instance made from mineral wool or expanded polystyrene/polyurethane. The finishing involves placing continuous insulation boards using mineral renders and coatings, although some kinds of discontinuous tile finishing could also be applied (Jelle, 2011).

Figure 1. Seismic plus energy retrofitting system: (a) TRM Jacket + insulation material on a masonry wall; (b) TRM + heating system on the masonry infill of RC framed structure.



Source: (Bournas, 2018)

Box 1. Advantage of TRM over FRP for retrofitting masonry buildings

The replacement of organic matrices with inorganic ones, that is the use of textile reinforced mortar (TRM) instead of FRP, offers an effective solution, especially for heritage structures, where the limited invasiveness and compatibility aspects are extremely important.

Integrated seismic and energy retrofitting of buildings has been increasingly investigated in the scientific literature from both, a theoretical and an experimental, point of view. A recent study provided a state-of-the-art review and analysis of integrated retrofitting interventions (Pohoryles et al. 2022), dividing them into four different broad groups: (1) integrated exoskeleton solutions; (2) integrated interventions on the existing building envelope; (3) replacement of the existing envelope with better performing materials; and (4) interventions on horizontal elements.

Research into exoskeleton solutions includes BRB-braces with solar shading and diagrids with thermal panels. Auxiliary structures feature insulated RC walls and RC frames with thermal panels or masonry infills. Shear-wall solutions support energy retrofits with external steel structures, accommodating green facades, photovoltaics, or shading devices, and can expand living space. These solutions are highly invasive, significantly altering the building's exterior. For more details, see in Di Lorenzo et al. 2020.

Instead of adding external structures, existing buildings can be upgraded by strengthening walls with composite materials like TRM and adding thermal insulation (as described in Fig. 1a). TRM-based retrofitting is less disruptive, cost-effective, and environmentally friendly. Prefabricated TRM or TRC panels with insulation or capillary tubes (Baek et al. 2022, 2024), and Cross-laminated timber (CLT) panels with insulation (Smiraldo et al. 2023, Kallioras et al. 2024), offer reduced construction time and modularity. Implementing low-carbon retrofits, such as mass timber, is key to decarbonizing buildings and achieving climate neutrality by 2050. Finally, strengthening URM walls with new windows and structural frames improves both structural integrity and thermal performance.

Another approach is replacing external walls of masonry-infilled RC buildings with stronger, thermally insulating bricks or deformable infill walls decoupled from the RC frame. Additional thermal insulation is

usually needed, but sustainable or insulated bricks can enhance energy efficiency. Though invasive and disruptive, this method is typically low-cost (Pohoryles et al. 2022).

Finally, a study by Gkatzogias et al. 2022 analyzed the potential impacts of integrated renovation across EU regions, considering cost-benefit ratios and reductions in losses and energy use. Integrated renovation showed significant economic and safety benefits, reducing both fatalities and energy consumption at EU level.

The following chapters present a a systematic investigation of the concurrent retrofitting of masonry structures. This includes a review comparing TRM structural properties, model development through analytical studies, and a final analysis of loss mitigation benefits across the EU.

1.2 Context of relevant EU policies

The ageing European building stock requires remarkable renovation efforts to improve its energy performance and ensure structural integrity during extreme loadings and natural disasters such as earthquakes. The impact of the existing buildings stock on the environment is a topic of growing importance at international level. At EU level, buildings consume about 40% of the final energy consumption and are responsible for about 36% related greenhouse gas (GHG) emissions (European Commission, 2023). These large GHG emissions and high energy consumption are largely linked to the old stock of buildings in Europe, with a third of buildings being over 50 years (Filippidou and Jimenez Navaro, 2019). Currently, only a small portion of the existing building stock is renovated annually, with the rate estimated at 1% in 2020 (European Commission, 2020). To achieve the EU's ambitious goals of a zero-emission building stock and a climate-neutral society by 2050, there is a pressing need to significantly accelerate the rate of building renovations.

Box 2. Boost EU policies implementation

Integrating energy efficiency upgrading with seismic strengthening will incentivise renovation further and boost EU policies implementation.

Renovation and retrofit strategies are required to upgrade the ageing building stock in the developed countries of the world since demolition and rebuilding are neither an economically viable nor an environmentally friendly solution at large scale. That is why comprehensive energy and climate policy packages have been introduced to progressively improve the energy performance of EU buildings (Economidou et al., 2020). The Green Deal strategy sets the ambitious target of transforming the EU into the first climate-neutral continent by 2050, emphasizing the importance of a cross-sectoral approach (European Commission, 2019). The Renovation Wave strategy aims to at least double the annual building renovation rate by 2030 and promotes deep renovation. In 2021, the Commission introduced the Fit for 55 package to align EU laws with the target of reducing GHG emissions by 55% by 2030, compared to 1990 levels, which is a stepping stone toward the 2050 climate neutrality goal (European Parliament, 2021).

One of the key legislative instruments is the Energy Performance of Buildings Directive (EPBD), the main legal instrument for boosting energy efficiency in EU buildings. First introduced in 2002, the EPBD has been revised several times to align with the more ambitious EU energy and climate targets. The 2018 amendment placed a strong emphasis on an integrated renovation approach, introducing strengthened provisions to support building renovations (European Commission, 2018). The directive encouraged Member States to adopt highly energy-efficient measures, while also addressing risks related to seismic activity, which can affect energy efficiency renovations and the lifespan of buildings. In response, several Member States incorporated seismic risk mitigation into their Long-Term Renovation Strategies (LTRSs). An evaluation of the LTRs by (Castellazzi et al., 2022) revealed that many countries positively received the recommendation to integrate seismic strengthening with energy efficiency upgrades. Although not a mandatory requirement, several national strategies addressed this issue, with a few countries providing specific measures (e.g., Croatia, Cyprus, Hungary, Italy, Romania, Slovenia, and Spain).

The 2024 recast EPBD introduces a formal definition for deep renovation and recognizes it as a prime opportunity to increase building resilience against disaster risks, including earthquakes, create better indoor conditions, and increase climate resilience besides reducing energy consumption (European Commission, 2024). The importance of this cross-sectoral approach is highlighted by a growing body of literature over the past decade, which highlights its potential for delivering holistic solutions to complex challenges (Pohoryles et al., 2022, Kakoulaki et al., 2023). This trend is expected to further evolve as the focus on integrated policies continues to expand. Further research is needed to explore how renovation strategies can address safe and healthy indoor environments, energy and resource efficiency with a view of minimizing the life-cycle impacts of buildings (Maduta et al., 2023).

2 State-of-the-art on the experimental performance of the textile-reinforced mortar (TRM)

2.1 Performance of TRM

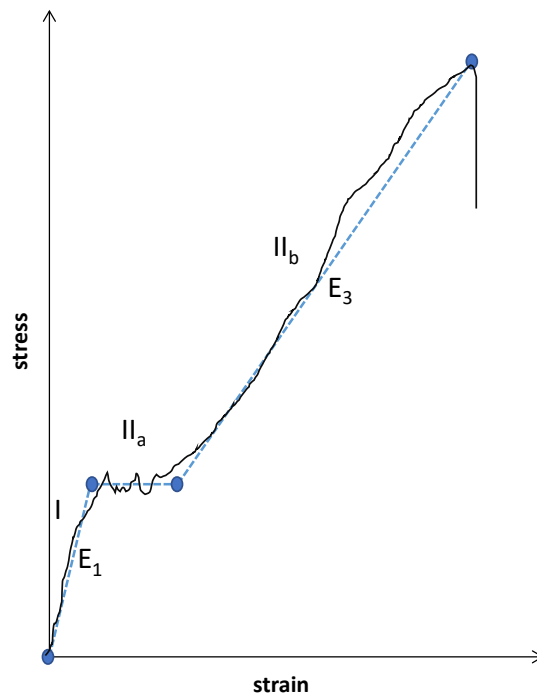
TRM is a composite material consisting of textiles embedded in an inorganic matrix as a replacement of the organic resins. Commonly, the fibres are made of high strength industrial materials such as glass, carbon, basalt, aramid, polypropylene (PP), polyparaphenylene benzobisoxazole (PBO), steel etc. (Brameshuber, 2016; Gries et al., 2016; T.C. Triantafillou, 2016) but also less strong natural materials from plant or animal fibres such as abaca, coir, flax, hemp, jute, sisal, hemp etc. (Cevallos et al., 2015; Gkournelos et al., 2022; Habibi et al., 2019; Olivito et al., 2016, 2014; Valluzzi et al., 2014), can be applied. The most common matrix is cement-based, but also hydraulic lime mortars which are more compatible with traditional masonries can be used, e.g. (Mechtcherine et al., 2016). Several experimental campaigns have investigated the performance of TRM as a strengthening material. The effectiveness and appropriateness of TRM as a strengthening and retrofitting material for unreinforced masonry structures is due to the high strength-to-weight ratio, minimal invasiveness, resistance at high temperatures, applicability at low temperatures, applicability on high dampness and irregular surfaces, vapour permeability, easy and safe application for workers and the environment, chemical and mechanical compatibility with various masonry substrates, and a high level of reversibility which is an important issue for cultural heritage structures. As it will be shown below, the effective combination of a TRM jacket with thermal insulation boards without side effects on their performance is a top advantage as it achieves cost savings due to the same nature of workmanship (scaffolding, preparation of the substrate etc.) and minimum invasiveness during application.

Generally, the binder system of TRM, being of inorganic and mineral nature, present a looser adhesion to the substrate in respect to organic resins of FRPs provided that the textile is properly bonded and depending on the surface preparation (Bellini and Mazzotti, 2017) no matter what the fibre chemical and mechanical properties are. The inorganic matrix is a fresh material and cannot achieve the same level of bonding of an epoxy. However, the bond mechanism between textile and matrix is complicated in the case of TRMs and presents a pseudo-ductile behaviour due to gradual cracking and textile pull-out phenomena which is actually preferable in the case of seismic performance as it can absorb energy.

The bond at the textile-mortar interface is a macroscopic mechanism which at a micro level is responsible for the stress transferred between the filaments within a yarn and between the yarn and the matrix. Simulating the bonding mechanism explicitly in a model is a very challenging task (Düreth et al., 2020) since most of the interactions have a random nature. To this end, in this report an empirical expression is derived based on experimental and numerical data (Kouris et al., 2023). The key element during the bond mechanism is that the inorganic matrix is not able to fully penetrate between the filaments that constitute the fabric yarns, because the cement grain dimensions are too large compared to the space among the filaments. Therefore, a stochastic penetration appear which leads a different yarn inner and outer bond. The bond failure mechanism is finally a “telescopic” one, involving several local failures in the micro level, including slippage and unequal stress levels among filaments (Donnini et al., 2016). The outer filaments carry a higher stress level compared to the inner filaments of the yarn and cause the telescopic failure. Hence, the achieved ultimate stress is lower than the nominal value of the material. Impregnation of the yarns into organic resin before embedment in the inorganic matrix, along with coating of the rovings with sand grains has been proposed in order to smooth the stress variations and improve bonding e.g. (Donnini et al., 2016), albeit at the expense of limiting the ability to apply the materials on elements with high curvature. Studies have shown that the more layers of textiles the higher the actual bond of the fibers achieved (Askouni and Papanicolaou, 2019; Makashev et al., 2023).

To derive the basic material mechanical properties of TRM, rectangular coupon specimens should be tested in tension monotonically, e.g. (ICC Evaluation Service, 2013). A tensile coupon is made in a flat mold by applying successive layers of mortar (3-4 mm thick) and textiles in sandwich-type manner. A typical stress – strain curve is illustrated in Figure 2 and an idealised trilinear form can be defined, where E_1 , E_2 and E_3 are the elastic moduli in phases I, IIa and IIb, respectively e.g. (De Santis et al., 2017; Kouris and Triantafillou, 2018; T.C. Triantafillou, 2016; Thanasis C. Triantafillou, 2016). The strains are measured either by digital image correlation which can capture a high resolution and nonuniformly distributed strain field (Bilotta et al., 2017) or applying conventional measurement systems (i.e. strain gauges and LVDTs).

Figure 2. Response of TRM in tension: experimental behaviour and trilinear idealisation.



2.2 In-plane performance of the hybrid system

In-plane failure of masonry members is the result of actions parallel to the walls. Typical seismic actions include bending and shear, with or without axial force. Diagonal in-plane shear failure in masonry is typical in shear wall-type elements. On the contrary, a flexural failure appears in slender piers. Strengthening can be provided by applying TRM jackets so that a “truss” mechanism may be activated (in analogy to the way shear is carried by reinforced concrete members).

TRM-based strengthening of masonry walls subjected to in-plane cyclic loads has been studied experimentally by Papanicolaou et al. (Papanicolaou et al., 2007). In this study it was shown that TRM overlays provide an extremely high gain in strength and deformation capacity, comparable - if not higher - to that provided by equivalent FRP systems. Namely, slender and squat piers and spandrel beams have been tested and their strength and deformation capacity has been found to increase several times.

In-plane diagonal compression tests were performed in various types of specimens, such as: two-leaf brick walls (Benedetti, 2019; Ismail and Ingham, 2016, 2014), one-leaf brick walls (Babaeidarabad et al., 2014b; Koutas et al., 2014), tuff volcanic masonry walls (Del Zoppo et al., 2019; Marcari et al., 2017; Prota et al., 2006), brick masonry walls (Sagar et al., 2017). In-plane tests on cantilever piers and spandrel beams have also been performed by Papanicolaou et al. (Papanicolaou et al., 2007), who tested one-leaf brickwork walls with various aspect ratios and axial load levels. The structural integrity during loading was achieved with TRM. The increase of the capacity was substantial in all the cases which reached even more than 100% of the unreinforced capacity limited by the compressive strength of masonry. Double-sided jackets offer a higher strength increase albeit at the expense of a lower ductility (Del Zoppo et al., 2019).

Moreover, pier-spandrel assemblages have been tested to study the critical interaction between reinforced spandrels and unreinforced piers (Augenti et al., 2011; Ismail and Ingham, 2016; Parisi et al., 2011). In all cases, the improved behaviour of URM with TRM in terms of strength and deformation capacity has been demonstrated. Moreover, the better performance of TRM versus FRP with regards to deformation capacity has been reported (Papanicolaou et al., 2011). In cyclic loading the improved deformation capacity was accompanied by reduced strength degradation and high energy dissipation (Augenti et al., 2011).

Box 3. TRM strengthened masonry elements

In all the tests carried out on masonry elements strengthened with TRM and loaded in-plane, an increased strength and deformation capacity was noticed with improved performance in terms of strength degradation which can add significant ductility and energy dissipation during seismic oscillations.

The application of lime mortars which present a higher compatibility with old masonry walls has been tested and the strength capacity was increased twice as much (Benedetti, 2019). The external layer in this case is thicker than the one made of cementitious matrices.

The hybrid thermo-structural retrofitting has also been tested in in-plane cyclic loads (Baek et al., 2022; Gkournelos et al., 2020; Triantafillou et al., 2018). The position of the TRM layer has been investigated and interestingly, it was found that even if the thermal insulation is attached on the wall in between an external TRM layer, the capacity of the wall maintained similar strengths when a careful bonding of the various layers is realised. In this direction, the use of lightweight mortars with a higher thermal resistance can contribute also to the insulation of the wall and use of thinner thermal boards (Longo et al., 2020)

2.3 Out-of-plane performance of the hybrid system

TRM-based strengthening of masonry walls subjected to out-of-plane cyclic loads showed an extremely high gain in strength and deformation capacity, comparable - if not higher - to that provided by equivalent FRP systems (Harajli et al., 2010; Papanicolaou et al., 2008). The observed failure is due to either masonry cracking or textile failure (usually debonding or tensile breakage).

Out-of-plane four-point bending tests were carried out to investigate the improvement of the masonry performance in terms of strength and deformation capacity, due to the application of this strengthening technique (Gattesco and Boem, 2017). Three point bending (Kariou et al., 2018; Papanicolaou et al., 2008; Shermi and Dubey, 2017) or four point bending (Babaeidarabad et al., 2014a; Harajli et al., 2010; Kadam et al., 2015; Martins et al., 2015; Padalu et al., 2019; Sagar et al., 2017; Valluzzi et al., 2014) tests have been performed in various types of masonry walls made of natural, concrete or brick units. In all the cases, the capacity of the strengthened wall was several times larger than that of the URM wall.

A test campaign investigating plenty of parameters including the thickness of the masonry wall, three different textile materials, various number of layers, the coating of the textiles etc. carried out by (Kariou et al., 2018) and it is used in the next chapters as a benchmark to calibrate analytical models. The test campaign involved eighteen specimens in three-point bending including two control specimens (unstrengthened). The load was increasing monotonically at the mid-span of the masonry piers which had 18 courses of bricks units in a stretcher bond. Mortar joints were approximately 10 mm thick, and the specimens' dimensions were 1.34 m long × 0.44 m wide. Wall thickness was a parameter under investigation and therefore, the eight single wythe piers (S) were 0.1025 m thick, while the eight double wythe piers (D) were 0.215 m thick as they include one head mortar joint. Three different fibres were used: (i) carbon (C), (ii) glass (G) and (iii) basalt (B). In this study, only the carbon textile is investigated. The basic material properties details are presented in Table 1. Details about the epoxy resin and the impregnation process can be found in (Kariou et al., 2018). The thickness of the coat is 3 mm for the one-layer carbon textile.

Shaking table tests of a full scale U-formed specimen, sub-assembly of a real structure, were performed to study the out-of-plane high efficiency of a TRM system comprising of steel cords embedded in lime mortar (De Santis et al., 2016).

The hybrid system of the simultaneous retrofitting has been also tested in out-of-plane loads where the thermal insulation has been either attached on the layer of the structural reinforcement or placed between the wall and the TRM (Triantafillou et al., 2017). In the former case the insulation can protect TRM from fire (Triantafillou et al., 2017) whereas in the latter case there is a strength and deformation gain due to an increased lever arm provided that the bonding is sufficiently ensured (Gkournelos et al., 2020). However, in-plane cracking of the wall can reduce the capacity of the out-of-plane performance by 10% on in comparison to an intact member (Gkournelos et al., 2020). In such a case it was found that the hybrid system would not have the latter extra gain in respect to the merely TRM reinforced wall despite the increased lever arm due to a premature shear and debonding failure.

Table 1. Material properties: elastic modulus [GPa] and strength [MPa].

Material	Strength [MPa]	Elastic modulus [GPa]
Masonry	9.7	2.5
Reinforcing mortar (matrix)	6.0	0.8
Carbon	3800	225
Glass	1400	74
Basalt (coated)	1351	89

Source: (Kariou et al., 2018).

Box 4. The thermo-structural hybrid retrofitting of masonry elements

The hybrid system of the simultaneous retrofitting apart from a cost-effective solution which tackles two problems in one solution, offers a thermal protection to the TRM layer(s) in elevated temperatures and no matter the position of the layers the strength and deformation capacity is at least the same if not higher in respect to a wall with only structural reinforcement.

As it can be deduced from the previous, the simulation of masonry walls strengthened with jackets of TRM is a challenging task due to complex interactions of the various materials. A first simplification is the homogenisation of the properties of mortar joints and brick units which is described in the next chapter.

3 Homogenisation of masonry properties

3.1 Overview of homogenisation

The mechanical properties of vernacular masonry structures present a large discrepancy depending on the variety of materials, bonding properties, geometry of the layout, and other arrangements related to the craftsmanship of masons. Masonry material is, in fact, a multiphase continuum comprising variations, discontinuities, cracks and interfaces. In view of the real nature of the material during service, a detailed discrete micro-model should consider the exact arrangement of masonry units and mortar joints along with their distinct properties and those of the interfaces (Figure 3a). Due to the inherent complexity of such an approach its use is only limited to element-wise (local) analysis and they are neither feasible, nor applicable especially for the design of buildings (Lagomarsino et al., 2013) or, building aggregates (Formisano et al., 2015; Maio et al., 2015) since the additional computational effort is very high and the exact units and mortars geometry difficult to be accurately defined and meshed.

Therefore, the commonly applied design methods are based on homogenised macro-mechanical properties of masonry utilising either shell or beam elements i.e. the well-known equivalent frame model to describe the global behaviour of masonry structures (Belmouden and Lestuzzi, 2009; Chen et al., 2008; Kouris et al., 2014; Kouris and Kappos, 2012; Lagomarsino et al., 2013; Penelis, 2006; Penna et al., 2014a).

In the first place, the elastic moduli are needed for modelling masonry walls. The current codes however do not include physics or theoretical estimates. Instead, estimates of the elastic moduli of masonry walls are used based on either wallette experiments or, on empirical formulas involving the wallette compressive strength which in turn is also given by an empirical formula. Such an approach typically results in large discrepancies (Tomazevic, 1999). Clearly the consideration of a perfectly homogeneous and isotropic material with a single adjustment of the elastic modulus is far from being a realistic assumption. To this end, a new homogenization model was deemed necessary and developed here with a dual aim: (i) to achieve a higher accuracy in respect to the existing models, but also (ii) to be as practical and easy-to-apply as possible. For a more detailed description the reader is referred to (L. A. S. Kouris et al., 2020).

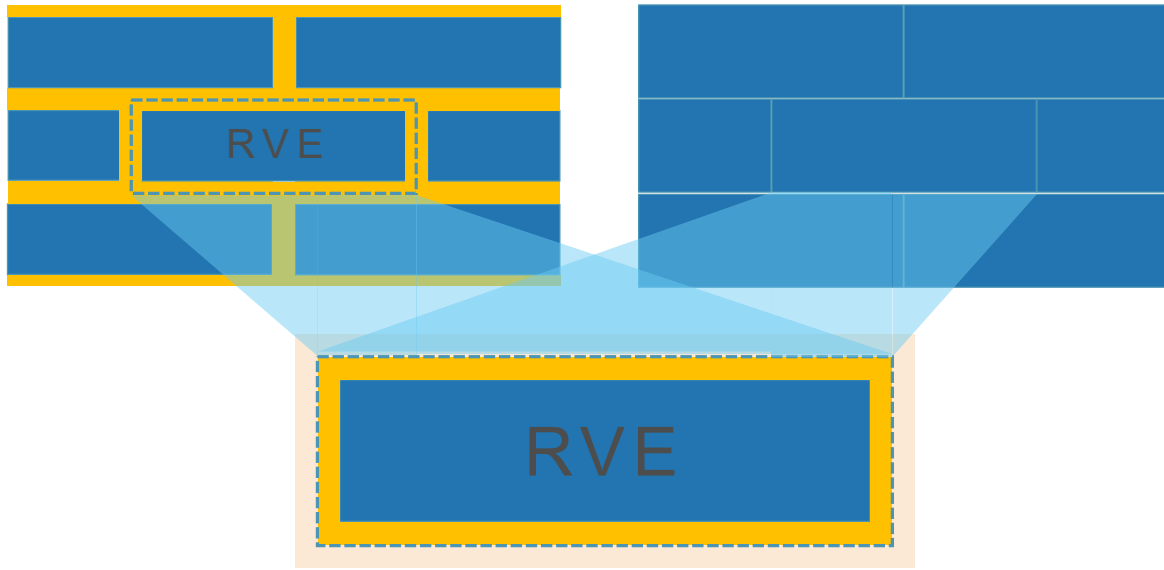
Box 5. Homogenisation model for masonry walls

The homogenised properties are commonly used in the simulation of masonry buildings. A new homogenization method is developed here aiming to achieve an accurate and a practical and easy-to-apply model.

Traditional masonry comprises brick or stone units bound together with mortar. When a masonry wall is loaded can fail in either constituent material or their interfaces. Therefore, a meticulous modelling approach of masonry is a distinct model of both brick units and mortar joints and all their interfaces. A first simplification can be to homogenise the mortar joints with the brick units while keeping their interaction. This proposed approach is a balance between a simplified smeared cracked approach with a continuum model and on the other hand, a detailed model with several interaction interfaces, thus, keeping the model affordable numerically.

In this modelling approach a representative volume element (RVE) is considered (Figure 3), i.e. the brick unit together with half mortar joint around it. The NL behaviour is attributed to the stiffness degradation based on two material models: (i) plasticity and, (ii) damage. The former is related to the post-yield response up to the maximum capacity and the latter to the material softening.

Figure 3. The homogenised modelling approach for masonry using the representative volume element; in light blue the interaction interfaces.



Source: (L. A. S. Kouris et al., 2020).

3.2 Gradient elastic theory

Under the assumption of periodicity, the RVE elastic properties can be determined experimentally from masonry prisms or, from the properties of the constituents and the application of a homogenisation rule which ideally should consider the orthotropic elastic properties (L. A. S. Kouris et al., 2020). Classical elasticity theory is extensively used in a wide range of design problems and applications in civil engineering. However, it fails to represent local heterogeneity phenomena. The incorporation into the classical linear elastic constitutive relation of strain ε_{kl} and stress σ_{ij} of the continuum media of the Laplacian of the strain can remedy this shortcoming of the elastic theory (Aifantis, 2003, 1992). Assuming a general elastic material the enhanced constitutive elasticity law between the stress σ_{ij} and the strain ε_{kl} tensors becomes as follows:

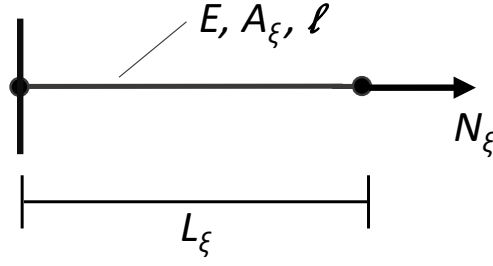
$$\sigma_{ij} = C_{ijkl} \left(\varepsilon_{kl} - \ell^2 \nabla^2 \varepsilon_{kl} \right) \quad (1)$$

where C_{ijkl} is the material elastic moduli fourth order tensor and ℓ is the internal non-local length. The larger the ℓ is the wider is the area affected by the local developed strain gradients.

Next, an axial single degree of freedom (SDOF) gradient elastic spring is assumed with cross-section area A_ξ and length L_ξ along the longitudinal axis ξ (Figure 4).

The considered element is assumed fixed at the one side ($\xi=0$) and free at the end ($\xi=L_\xi$) where the axial load N_ξ is applied.

Figure 4. Axial 1-D gradient elastic element.



Source: (L. A. S. Kouris et al., 2020).

Kinematic consistent boundary conditions (Eqs. (2)) are considered to estimate the constants; one classical condition for the displacement at the fixed end; two non-classical ones for the second derivative of the displacement at the fixed end and the other based on its vanishing of the derivative at the free end (Akintayo et al., 2012; Askes et al., 2008; Askes and Aifantis, 2011; Mousavi and Aifantis, 2016; Polizzotto, 2018, 2003; Ru and Aifantis, 1993; Tsepoura et al., 2002):

$$u_0 = 0; \frac{d^2 u_0}{d\xi^2} = 0; \frac{du_{L_\xi}}{d\xi} = 0 \quad (2a,b,c)$$

By substituting Eqs (2) in the constitutive Eq (1) and solving the third order ordinary differential equation (ODE) the displacement and axial force at the free end ($\xi=L_\xi$) are expressed as:

$$u_\xi = \frac{N_\xi L_\xi}{EA_\xi} \left[1 - \frac{\ell}{L_\xi} \tanh\left(\frac{L_\xi}{\ell}\right) \right] \quad (3a,b)$$

$$N_\xi = \frac{EA_\xi}{L_\xi} \left[1 - \frac{\ell}{L_\xi} \tanh\left(\frac{L_\xi}{\ell}\right) \right]^{-1} \cdot u_\xi$$

Thus, the axial stiffness k of the gradient elastic spring is given:

$$k_\xi = \frac{EA_\xi}{L_\xi^*} \quad (4a,b)$$

$$L_\xi^* = L_\xi \left[1 - \frac{\ell}{L_\xi} \tanh\left(\frac{L_\xi}{\ell}\right) \right]$$

In Eq. (4a) L_ξ^* is the effective 'gradient' quantity of the length L_ξ of the spring given by Eq. (4b). Obviously, the classical elastic spring and the gradient one differ only in the estimation of the spring length, i.e. the former's length L is the actual length of the spring, while the effective length L_ξ^* is given by a simple expression involving the ratio of the internal length ℓ to the geometric length L_ξ .

Following the same procedure, a gradient elastic shear spring can be established starting from Eqs. (1) and (2) and considering only shear stresses and strains for a shear element with dimensions $L \times H$, with y being the

vertical axis. Denoting τ the shear stress, γ the shear strain, A_s the shear cross section and G the shear modulus, the respective equations for the gradient elastic shear strain are:

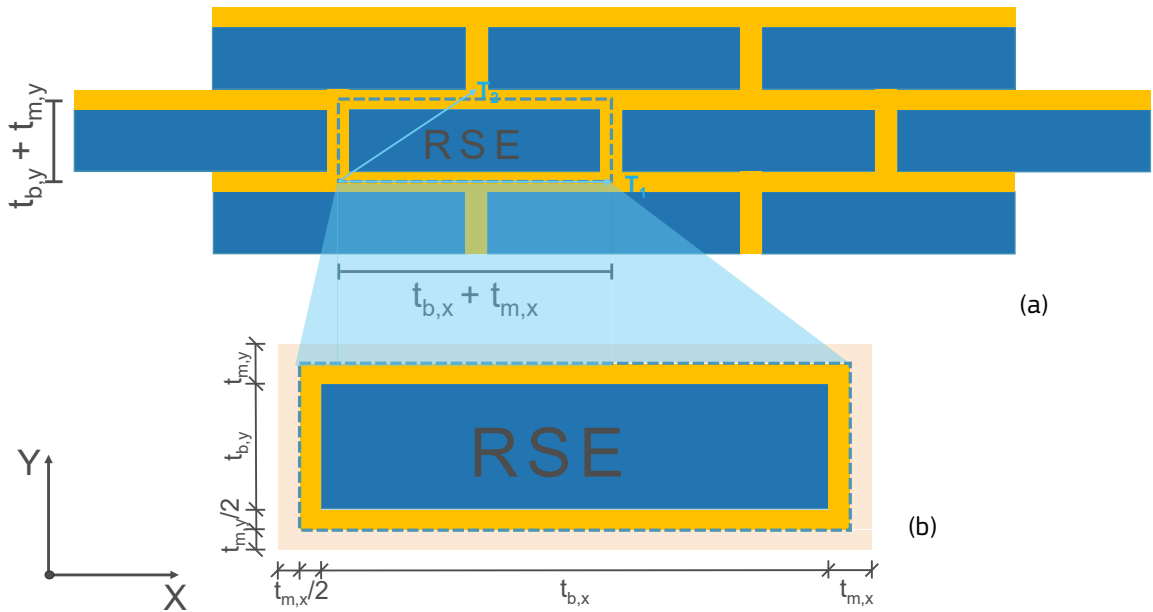
$$\begin{aligned}\tau &= G \left(\gamma - \ell^2 \frac{d^2 \gamma}{dy^2} \right) \\ k_s &= \frac{GA_s}{H^*} \\ H^* &= H \left[1 - \ell \tanh \left(\frac{H}{\ell} \right) \right]\end{aligned}\tag{5a,b,c}$$

where the shear strain is as usual equal to $\gamma = du/dy$.

3.3 Gradient homogenisation model (GREHM)

GREHM is developed for a running or a stack bond masonry but the methodology can be easily adapted to other masonry bonds. The representative element of the periodic masonry wall, which is the smallest repetitive cell, for these two bonds consists of one brick unit bounded by half thickness mortar joints as shown in Figure 5. This element is repeated throughout a masonry wall excluding boundaries.

Figure 5. The representative surface element (RSE) of running bond brickwork: (a) on the wall, (b) a close-up.



Source: (L. A. S. Kouris et al., 2020).

The periods of the spatial variation of the medium \mathbf{T} in the 2D dimensional space are equal to the respective dimensions of the representative surface element (RSE), namely the length and height of the brick and the mortar joint, respectively, i.e. $\mathbf{T} = [(t_{m,x} + t_{b,x}) (t_{m,y} + t_{b,y})]^T$ (see also Figure 5). The geometric and mechanical properties of masonry represented by the function \mathbf{J} fulfil the regular periodicity rule for composite media (Hassani and Hinton, 1998):

$$\mathcal{F}[\mathbf{x} + \mathbf{N}(b) \cdot \mathbf{T}] = \mathcal{F}(\mathbf{x}) \text{ where } \mathbf{x} = \begin{bmatrix} x_i \\ y_i \end{bmatrix} \text{ and } \mathbf{N}(b) = \begin{cases} \begin{bmatrix} 1/2 & 0 \\ 0 & 1 \end{bmatrix}, b=1 \\ \begin{bmatrix} 1 & 0 \\ 0 & 1 \end{bmatrix}, b=2 \end{cases} \quad (6)$$

In Eq. (6) \mathbf{x} is the coordinates vector of a certain i point, \mathbf{T} is the period vector and \mathbf{N} matrix depends on the bond $b = \{1 \text{ for running bond, } 2 \text{ for stack bond}\}$. It should be noted that the geometry of the RSE presents a double symmetry in the horizontal and vertical axes.

On the boundary of the RSE a uniform stress distribution is assumed which is valid for gravity loads. For dynamic loads the spatial stress variation is assumed very small and neglected in the RSE as normally the vector \mathbf{T} will be very small to the total dimensions of the wall. For the elastic response of the RSE the mortar joints are considered fully interconnected to the brick unit and no sliding is taken into account. Moreover, the thickness of the wall is assumed very thin compared to the other dimensions and the wall as a plane 2-D element. In the following elastic analysis the assumption that plane sections remain plane after deformation is also made and the Poisson effect is neglected. Based on gradient elasticity and these assumptions, the RSE is equivalent to a set of springs for the constitutive components respectively; brick units, mortar head and bed joints. The dimensions of the RSE are shown in Figure 5b. The thickness of mortar joints is denoted as $t_{m,x}$ for head joints and $t_{m,y}$ for bed joints. The brick units have dimensions $t_{b,x}$ and $t_{b,y}$ in the horizontal and vertical direction, respectively. A raised asterisk (\bullet^*) is used in the following to denote the gradient quantity of the respective dimension according to Eq. (4b).

The elastic modulus of mortar is denoted as E_m whereas hollow brick units generally present an orthotropic behaviour having two elastic moduli $E_{b,x}$ and $E_{b,y}$ in the two directions (solid units are isotropic). The longer dimension is typically on the horizontal x axis. The Poisson's ratios are for mortar ν_m and for the orthotropic bricks $\nu_{b,xy} = \nu_{b,yx} E_{b,x} / E_{b,y}$. The gradient elastic stiffness of the axial and shear springs representing the masonry elements is estimated according to Eqs. (4a) and (5a). The same notation applies to the horizontal and vertical stiffnesses of mortar $k_{m,x|y}$ and bricks $k_{b,x|y}$, respectively.

3.3.1 Homogenised masonry elastic modulus E_v perpendicular to mortar bed joints (vertical)

For the estimation of the homogenised elastic modulus E_v in the vertical direction perpendicular to mortar bed joints a simplification on RSE (Figure 5) is possible: it is sufficient to consider only the bed joints assuming that the load is uniformly distributed and $t_{m,x} < t_{b,x} / 10$. The homogenised modulus of elasticity E_v after substitution of the spring stiffnesses in Eq. (4) and some algebraic calculation can be found:

$$E_v = t_{tot,y} \frac{E_{b,y} E_m}{2 \left(\frac{t_{m,y}}{2} \right)^* E_{b,y} + t_{b,y}^* E_m} \quad (7)$$

where $t_{tot,y} = t_{b,y} + t_{m,y}$ is the total thickness of the representative volume in the respective direction.

3.3.2 Homogenised masonry elastic modulus E_h parallel to mortar bed joints (horizontal)

For the estimation of the homogenised elastic modulus E_h in the horizontal direction parallel to mortar bed joints the full RSE (Figure 5) should be taken into consideration as the omission of the latter results in larger difference. Therefore, a uniform stress is applied both on the mortar head and bed joints are loaded. Due to strain compatibility and the interaction between mortar bed joints and the brick units the stress field becomes more complicated. A simplification is possible due to the small thickness of the mortar joints: the stress distribution in the bed joints can be assumed uniform. The closer to unity is the ratio E_b / E_m and the smaller the

mortar thickness the more accurate is this assumption. By analogy with Eq. (7) the homogenised elastic modulus in the horizontal direction E_h will be:

$$E_h = t_{tot,x} \frac{E_c E_m}{2 \left(\frac{t_{m,x}}{2} \right)^* E_c + t_{b,x}^* E_m} \quad (8)$$

where $t_{tot,x} = t_{b,x} + t_{m,x}$ is the total thickness of the representative volume in the horizontal direction.

3.3.3 Homogenised masonry shear elastic modulus G

The shear elastic modulus of the homogenised masonry is estimated using the gradient elasticity law of Eq. (5a). When the simplified RSE (i.e. without the head joints, see Figure 5) is loaded with a horizontal shear force then in all the layers the same stress τ is developed. Obviously, the total shear strain of the RSE is equal to the addition of the three elements. It is noted that the shear springs are in row loaded by the same shear force. As a result, Eq. (7) are here transformed as follows:

$$G = t_{tot,y} \frac{G_b G_m}{2 \left(\frac{t_{m,y}}{2} \right)^* G_b + t_{b,y}^* G_m} \quad (9)$$

where G_b and G_m are the shear elastic moduli of the brick unit and the mortar joints respectively.

3.3.4 Homogenised masonry Poisson's ratios ν_{xy} and ν_{yx}

The Poisson's ratio ν_{yx} is defined as the ratio of the horizontal dilatation to the vertical deformation for a vertical stress σ_y of the RSE (Figure 5) and can be expressed as:

$$\nu_{yx} = - \frac{\sigma_x}{\sigma_y} \frac{E_v}{E_h} \quad (10)$$

The sign at the right-hand side of Eq. (10) is minus because the developed stresses for classical materials have opposite signs. The horizontal E_h and the vertical E_v elastic moduli are given by Eqs. (8) and (7), respectively, whereas the vertical stress is $\sigma_y = F_y / A_y = F_y / t_{b,x}$ and the horizontal stress $\sigma_x = F_x / A_x = F_x / (t_{b,y} + t_{m,y})$. The vertical springs are in series and thus, they carry an equal force: $F_y = F_{by} = F_{my}$. In the case that the brick unit is a hollow brick with an orthotropic behaviour it will have two Poisson's ratios $\nu_{b,xy}$ and $\nu_{b,yx}$. Therefore, combining the latter with Eqs. (7), (8) and (10) it is concluded that:

$$\begin{aligned} \nu_{yx} &= \frac{\nu_b t_{b,y}^* + 2\nu_m \left(\frac{t_{m,y}}{2} \right)^*}{t_{b,x}^*} \frac{t_{b,x}}{t_{b,y} + t_{m,y}} \frac{E_v}{E_h} \\ \nu_{xy} &= \frac{\nu_b t_{b,y}^* + 2\nu_m \left(\frac{t_{m,y}}{2} \right)^*}{t_{b,x}^*} \frac{t_{b,x}}{t_{b,y} + t_{m,y}} \end{aligned} \quad (11a,b)$$

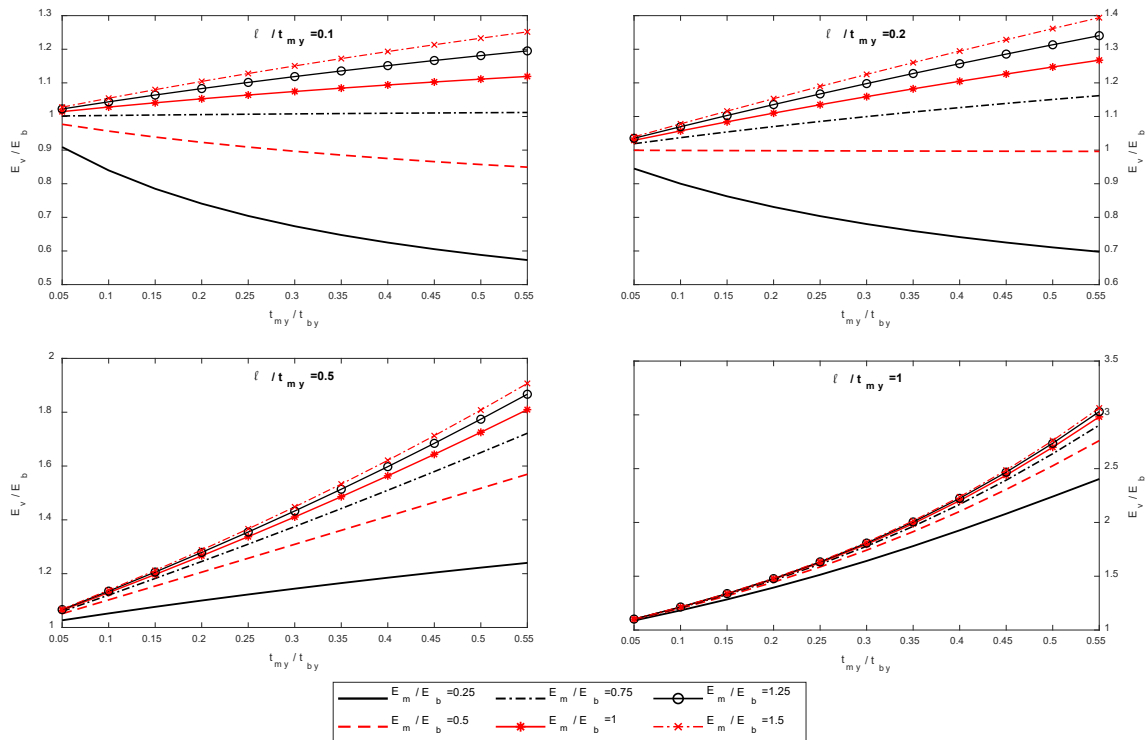
3.3.5 Normalised graphs for the estimation of the homogenised properties

The influence of the most important parameters on the orthotropic behaviour of masonry is investigated herein; these are (see Figure 5): (i) the internal length which is an internal non-local parameter of the model, (ii) the mortar joints and especially their thickness and, (iii) the comparative stiffness of the brick units to the one of the mortar which are the main physical parameters. Normalised plots for the elastic moduli are then provided.

- The thicker the joints are, the more affected is the macro-behaviour of masonry.
- The level of the influence depends on the mortar to brick modulus of elasticity ratio, E_m/E_b .
- The internal length is to limit this role. For example, a value of internal length ℓ equal to the mortar joint thickness leads to a much lower impact of the ratio E_m/E_b on the homogenised elastic moduli.

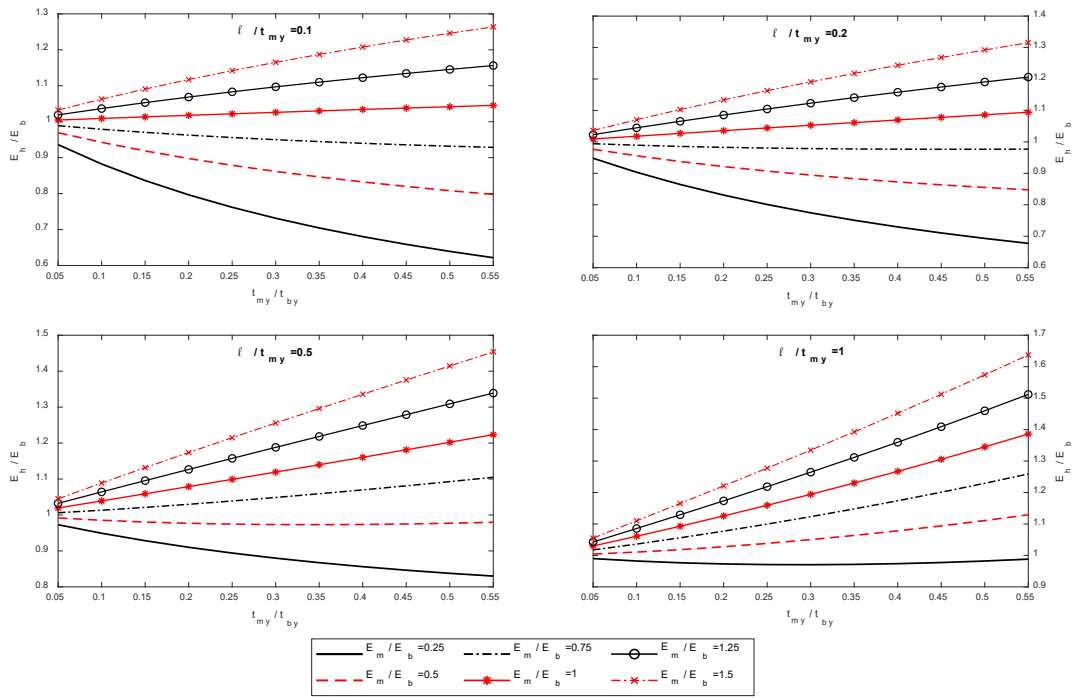
The influence of mortar joints in the vertical homogenised modulus is presented in Figure 6 where the thickness is represented in the horizontal axis, the ratio of E_m/E_b in various lines (see legend of Figure 6), and the internal length in successive plots. The normalised plots of the homogenised horizontal elastic modulus E_h and the homogenised shear modulus G are presented in Figure 7 and Figure 8 respectively. It is interesting to note that a soft mortar joint ($E_m/E_b = 0.25$) will affect the vertical elastic modulus up to a thickness $t_{my} = t_{by}$. Higher values of t_{my} will not have a significant impact on the mechanical properties which reach a stabilisation. This stabilisation thickness increases as the ratio E_m/E_b increases. Certainly, the ratio of E_m/E_b most predominantly rules the homogenised vertical modulus.

Figure 6. The (normalised) vertical elastic modulus E_v of masonry in respect to t_{my} / t_{by} for various ratios of E_m/E_b and ℓ/t_{my} .



Source: (L. A. S. Kouris et al., 2020).

Figure 7. The (normalised) horizontal elastic modulus E_h of masonry in respect to t_{my} / t_{by} for various ratios of E_m/E_b and ℓ/t_{my} .



Source: (L. A. S. Kouris et al., 2020).

Figure 8. The (normalised) shear elastic modulus G of masonry in respect to t_{my} / t_{by} for various ratios of E_m/E_b and ℓ/t_{my} .

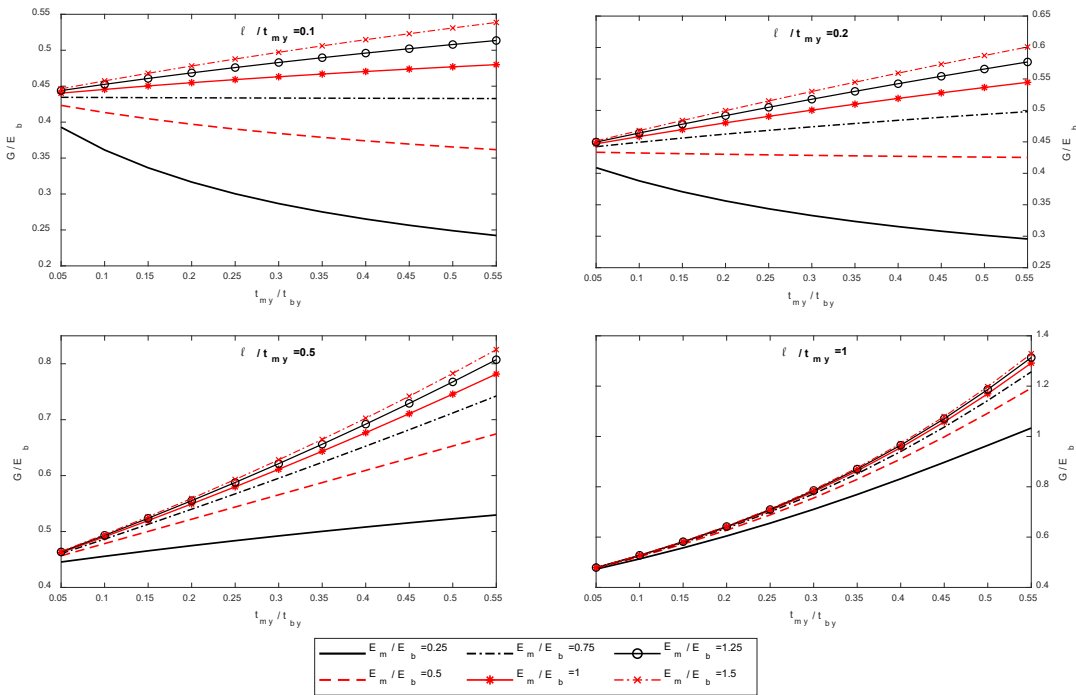
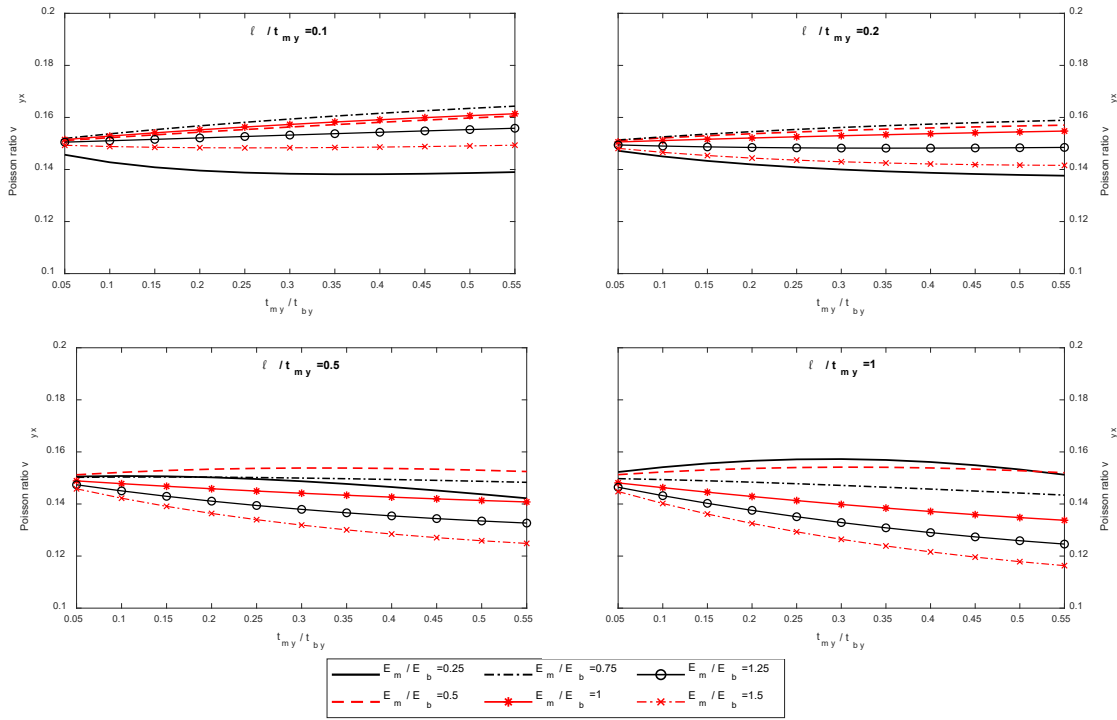


Figure 9. The Poisson's ratio ν_{yx} of masonry in respect to t_{my} / t_{by} for various ratios of E_m/E_b and ℓ/t_{my} .



Source: (L. A. S. Kouris et al., 2020).

Moreover, standard Poisson's ratios were assumed $\nu_b = 0.2$ for bricks and $\nu_m = 0.15$ for mortar and a ratio of the brick dimensions $t_{bx}/t_{by} = 3.25$ to plot the normalised graphs (which are the only fixed values that are included). The homogenised Poisson ratio ν_{yx} is presented in Figure 9 for various joint thicknesses and various internal lengths. It is noted that for the above assumed values of Poisson ratios for the bricks and mortar the typical value 0.25 of the codes is here the upper bound limit. An increasing trend is observed for the Poisson ratio as the internal length increases. This increasing trend is stronger when the ratio of mechanical properties of the two materials (E_m/E_b) is lower and for smaller thicknesses of the joints (which is the common case). The homogenised Poisson's ratio ν_{xy} can then be easily estimated using the formula $\nu_{xy} = \nu_{yx} E_h/E_v$ (Equation (11a,b)).

3.4 Verification of the proposed homogenisation model

3.4.1 Comparison with numerical homogenisation models

The proposed model is compared with a finite-element (FE) based homogenisation model (Anthoine, 1995) to verify the proposed equations and confirm the assumptions of the model. Apparently, the internal length in the FE comparisons is not playing a major role as the models are perfectly bonded and linear elastic apart from one case where the load creates a local singularity. The actual advantage of GREHM with the inclusion of an internal length will be shown in the next paragraph where the model is compared to experiments.

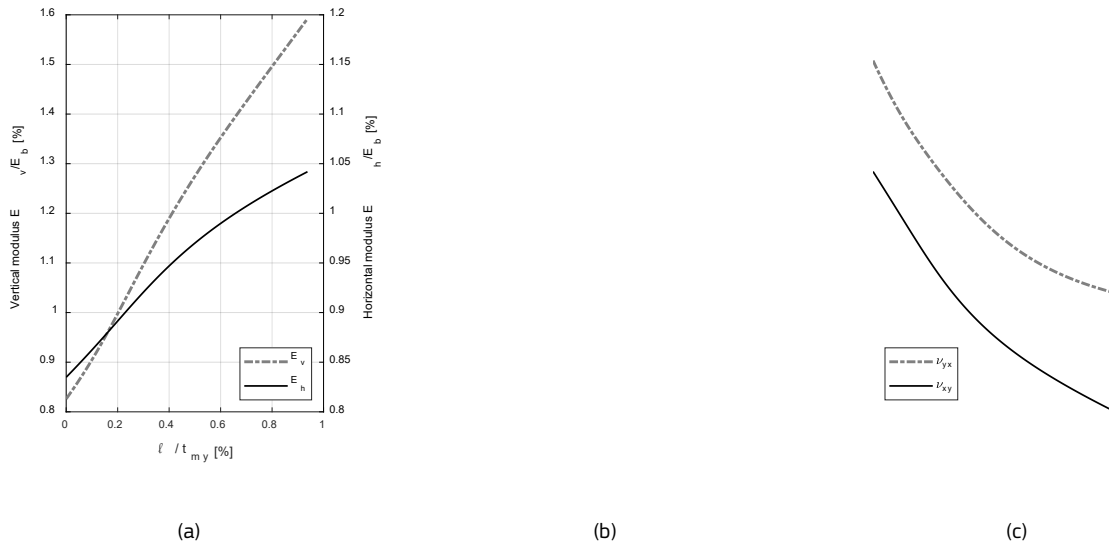
The wall used as a benchmark problem represents a specimen tested at the University of Patras, Greece (Papanicolaou et al., 2011). The wall is 1.17 m long, 1.20 m high and 0.095 m thick with an aspect ratio close to unity. The in-plane dimensions of the homogeneous solid bricks are 0.195×0.060 m ($t_{bx} \times t_{by}$) and the wall is single-leaf (i.e. the bricks are 0.095 m thick). The mortar thickness varies slightly in the two directions: $t_{m,x} = 0.0195$ m and $t_{m,y} = 0.0160$ m. The mechanical properties of the constituent materials needed for GREHM are summarised in Table 2. The shear moduli of brick units and mortar can be found 610 MPa and 290 MPa respectively.

Table 2. Properties of brick units and mortar joints for GREHM.

	Size (tx×ty) [m]	Elastic modulus (E) [GPa]	Poisson ratio (ν) -
Brick units	0.195×0.060	1.4	0.15
Mortar joints	0.0195×0.0160	0.7	0.20

The application of GREHM is carried out as follows: (i) for the estimation of the homogenised elastic moduli in the vertical E_v and the horizontal E_h directions Equations (7) and (8) are applied respectively; (ii) for the estimation of the homogenised shear modulus G Equation (9b) is applied; (iii) finally for the estimation of the Poisson's ratio ν_{yx} and ν_{xy} Equations (11a,b) are applied. As already mentioned in these equations the 'gradient' dimension (\bullet) is given by Equation (4b). A number of internal lengths are assumed ranging from 0 to t_{my} . The application of these equations and the influence of the internal length is depicted in Figure 10. Obviously, it is not a linear influence, with an increasing trend for the elastic moduli and a decreasing one for the Poisson ratio.

Figure 10. The influence of the internal length normalised against the thickness of mortar joints on (a) the horizontal and vertical elastic moduli and (b) the shear modulus (normalised against the brick elastic modulus) and, (c) the Poisson's ratio of the homogenised model.



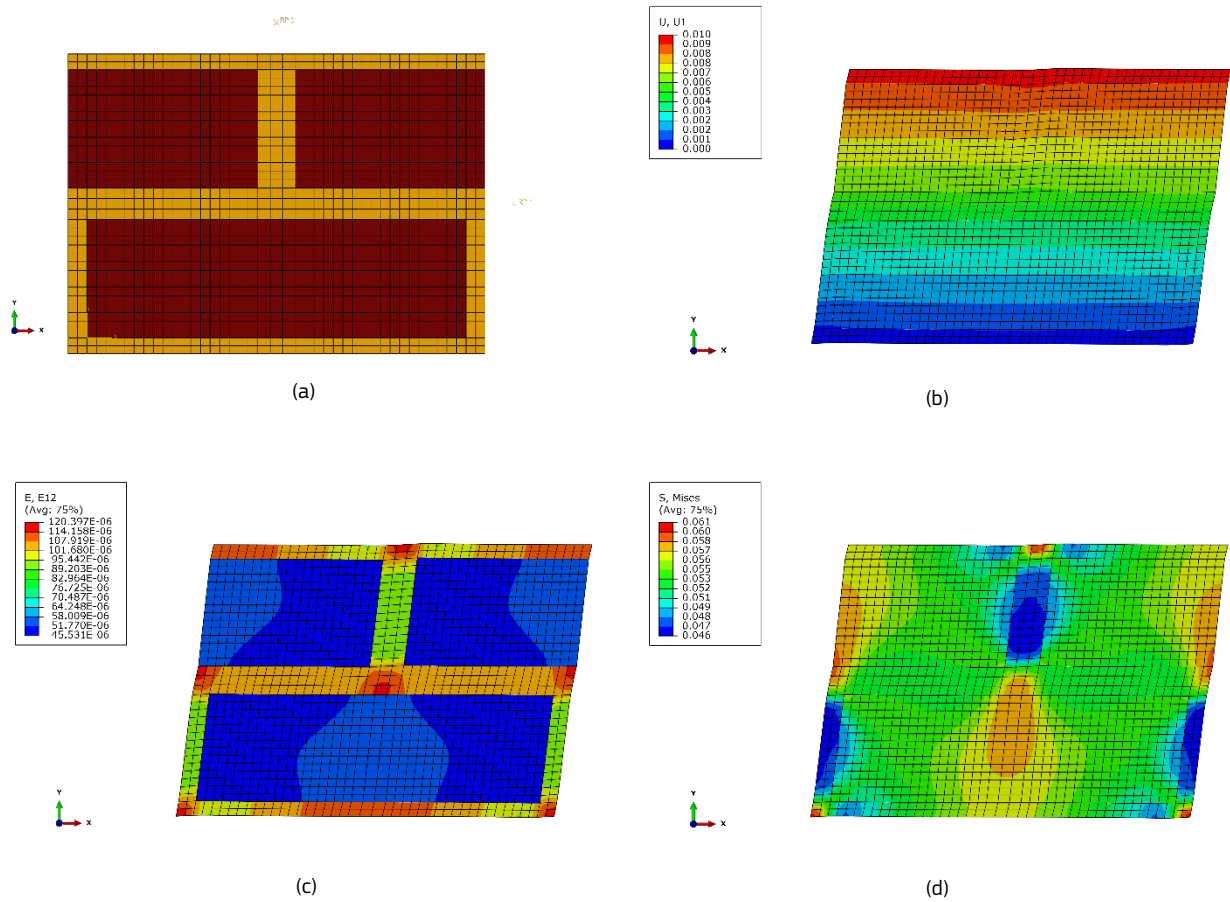
Source: (L. A. S. Kouris et al., 2020).

The estimation of the elastic properties of the considered wall is then, carried out using FE models (Anthoine, 1995) and compared with the previous results of the homogenised properties. In all the analyses the CPS4R four node plane stress element is used. The FEs representing the mortar joints and the bricks are fully connected between them (using nodal constraints) not allowing for any sliding at the interfaces. To this end a RSE with a rectangular pattern for \mathbf{T} (see also Figure 5) is selected and is presented in Figure 11 where red are the elements of brick units and orange those of the mortar. The mesh of the RSE is performed using rectangle (close to square) elements of size 8×8 mm approximately. The selection of this RSE essentially simplifies the periodic conditions on the boundaries (PCBs) around the RSE to the following ones:

$$\begin{aligned}
\delta_{x,right} - \delta_{x,left} &= \Delta_x \in R \ \& \ \delta_{x,right} = 0 \\
\delta_{y,bottom} - \delta_{y,top} &= \Delta_y \in R \ \& \ \delta_{y,bottom} = 0 \\
\delta_{y,right} - \delta_{y,left} &= \Delta_y \in R \ \& \ \delta_{y,right} = 0 \\
\delta_{x,bottom} - \delta_{x,top} &= \Delta_x \in R \ \& \ \delta_{x,bottom} = 0
\end{aligned}
\tag{12a,b,c,d}$$

where δ_x , δ_y are the displacements in x and y axis at the right, left, bottom and top boundaries of the RSE. The displacements $\Delta_x = 0.01$ mm and $\Delta_y = 0.01$ mm are applied to estimate the horizontal and vertical elastic modulus E_h and E_v and the Poisson's ratio ν_{xy} and ν_{yx} respectively using the PBCs given in Equations (12a,b). For the shear homogenised modulus G the PBCs expressed in Equations (12c,d) on the boundaries are applied with a horizontal displacement $\Delta_x = 0.01$ mm. The deformations and the strain and stress states for this latter case are presented in Figure 11. The results in terms of reaction forces (ΣF), stresses (σ , τ) and strains (ϵ , γ) of the RSE for all the loading cases and the respective homogenised resulted orthotropic moduli of E_h , E_v and G and Poisson ratios ν_{xy} , ν_{yx} are summarised in Table 3.

Figure 11. The FE model of the RSE: (a) model, (b) shear displacements, (c) shear strain, and (d) shear stress.



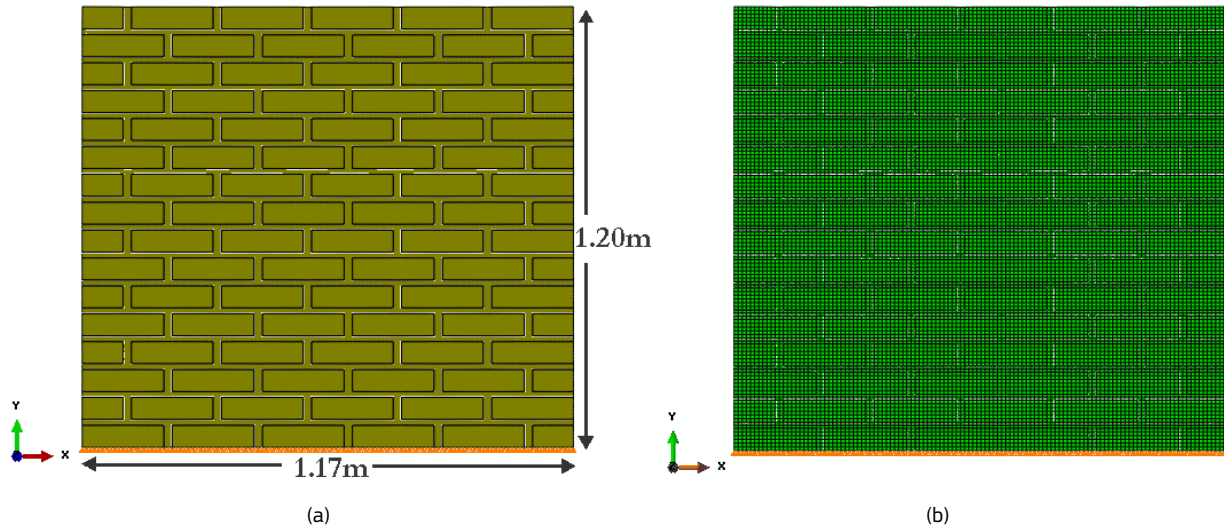
Source: (L. A. S. Kouris et al, 2020).

Table 3. Results from the FE analysis of the RSE and homogenised mechanical properties.

Results & Homogenised properties		Units	Load direction		
			Horizontal	Vertical	Shear
Results from FEA	ΣF	kN	-787.34	1499.59	628.61
	$\epsilon \mid \gamma$	-	4.66E-05	6.58E-05	6.58E-05
	ϵ (transversal)	-	7.61E-06	1.03E-05	-
	$\sigma \mid \tau$	GPa	-0.05	0.07	0.03
Homogenised properties	$E \mid G$	GPa	1169.55	1118.58	468.90
	$(E \mid G)/E_b$	-	0.84	0.80	0.33
	ν	-	0.16	0.16	-

In the FE analysis of RSE the inclusion of the internal length ℓ does not improve the accuracy. Comparing the results of Table 3 with those of GREHM presented in Figure 10 it can be seen that for $\ell = 0$ there is an excellent match: $E_v = 1156.5$ GPa, $E_h = 1168.8$ GPa, $G = 495.34$ GPa, $\nu_{xy} = 0.16$ and $\nu_{yx} = 0.16$ and the relevant differences 3%, 0%, 5%, 0% and 0%.

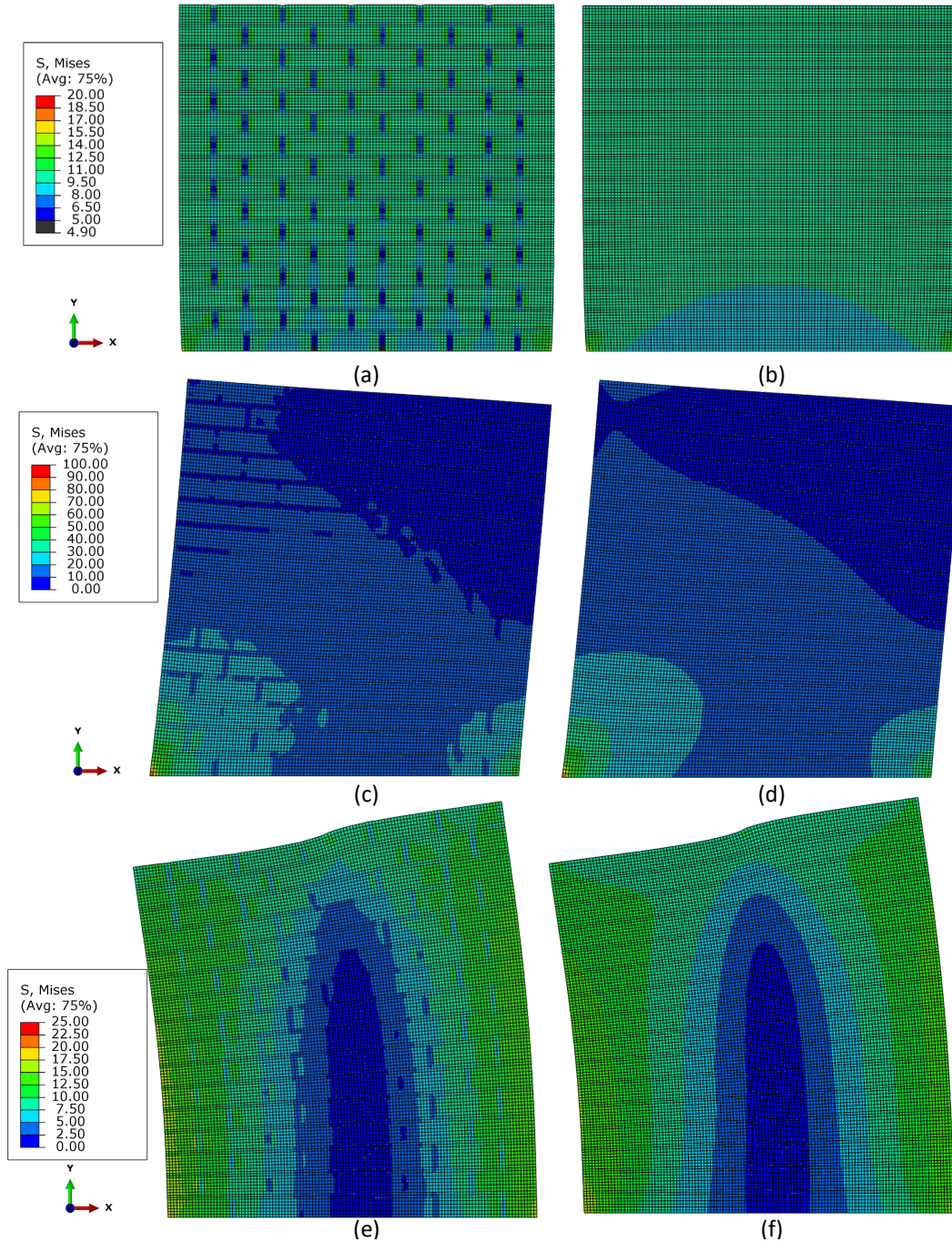
Figure 12. FEM of the wall: (a) the wall configuration, (b) mesh of the wall.



Source: (L. A. S. Kouris et al., 2020).

The influence of the internal length is also examined in a global analysis of a FE wall model. The wall is shown in Figure 12a. The brick pattern of the wall is not symmetric in the horizontal and the vertical direction: there are $5 \frac{1}{2}$ bricks in the horizontal courses and 16 vertical courses in total (Figure 12a).

Figure 13. Comparison between the (Mises) stress field in kPa of the distinct-properties model Γ_d (on the left) and GREHM model Γ_h (on the right) for a vertical (a,b), horizontal (c,d) and moment (e,f) load.



Source: (L. A. S. Kouris et al., 2020).

A first FE model, called the 'distinct' one Γ_d , comprises different (classical) elastic plane elements for brick and mortar bed and head joints shown in Figure 12b. The bricks have been meshed using 6×20 elements whereas the mortar using 2×20 and 8×2 elements for the bed and the head joints respectively using a mesh dimension approximately equal to $\frac{1}{2}$ of the mortar joint thickness. The elements are fully connected. The wall is restrained at its base to represent the experimental conditions. The previously defined homogenised properties are used throughout the homogenised FE model $\Gamma_h(\ell)$, using various internal lengths ℓ to compare its influence on the analysis. The stress and deformed state of Γ_d FE model is presented in the left side of

Figure 13 for a number of different external loadings p : (i) an evenly distributed vertical load 100kPa on the top (p_1), (ii) a lateral load of 100kPa applied on the vertical left side of the wall (p_2) and, (iii) an in-plane moment produced by a vertical distributed load inverting sign at the middle of the wall, i.e. 100 kN/m and -100 kN/m at the top (p_3), all applied statically. The Von Mises stress state is presented in kPa. It can be observed that the brick units being the stiffer material attract higher stresses. This is more dominant in the first loading case.

Next, a second FE model Γ_h is run but in this case applying GREHM: all plane elements of Γ_h have the same homogenised properties. A number of internal lengths ℓ ranging from 0 to 20 mm are assumed and hence, the respective models are generated $\Gamma_h(\ell)$. The same loads as previously are applied to all $\{\Gamma_h(\ell), \ell [0,20\text{mm}]\}$. The stress and deformed state of $\Gamma_h(\ell=0)$ are presented on the right of Figure 13 where it is seen that comparing the two stress states the homogenised model smooths out the distinct one.

A displacement approach is followed to compare the two models: the displacements of the model Γ_d with the distinct properties for the materials are assumed the correct values, and the error is estimated from the deviation of the respective displacements of the models with the GREHM properties $\Gamma_h(\ell)$ for the same loading conditions.

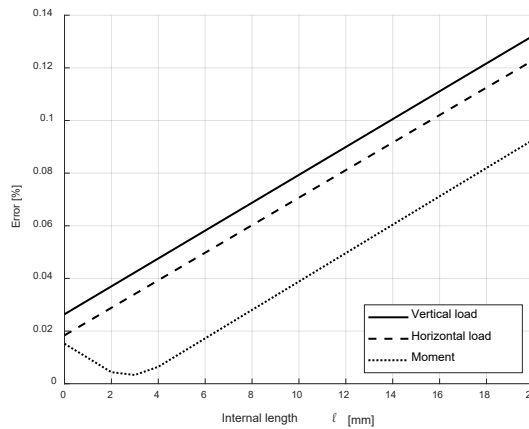
The error $e(\ell, p)$ between the nodal displacements j ($j = 1:n$) on the free boundaries of the distinct ($\delta_j^d(p)$) and the GREHM ($\delta_j^h(\ell, p)$) models is defined as follows:

$$e(\ell, p) = \frac{1}{n} \sum_{j=1}^n \left| \frac{\delta_j^d(p) - \delta_j^h(\ell, p)}{\delta_j^d(p)} \right| \quad (13)$$

Therefore, the error $e(\ell, p)$ is defined as the averaged summation of the errors between the respective displacements of the two models, i.e. $e(\ell, p) = \sum_j \epsilon_j$ for ℓ, p and $\epsilon_j \Gamma$ where j is a node on the free boundary of the wall $S = \partial\Gamma_{\epsilon \neq 0}$.

In Figure 14 the error $e(\ell, p)$ vs. the assumed internal length of each analysis for the three external loads p_1 , p_2 and p_3 is plotted. Interestingly the inclusion of the non-local length can increase the accuracy of the analysis for the moment load. In fact, the application of a vertical load changing sign in the middle of the top side of the wall creates a local singularity. An internal length ℓ around 4 mm can improve the estimation of the displacements in this case. For the other loading conditions the non-local parameter does not decrease the error. This would be expected for classical linear elastic FE models as has been already mentioned. For $\ell = 0$ the maximum error for all the loading conditions does not exceed 0.03%.

Figure 14. The influence of the internal length on the accuracy of the model for three different loading conditions.



3.4.2 Comparison with analytical homogenisation models

A review of the closed-form homogenisation models can be found in (Taliercio, 2014). Here a comparison is made between the proposed GREHM and three other models: the (Pande et al., 1989) model, and two other recent models (Di Nino and Luongo, 2019; Taliercio, 2014). The expression proposed in codes for the elastic modulus will be shown in a following section and compared with GREHM.

Table 4. Experimental testing of masonry walls: main parameters of brick units and mortar joints (continued).

Exp. Campaign	E_b [MPa]	$t_{b,y}$ [mm]	$t_{b,x}$ [mm]	w^* [mm]	E_m [MPa]	$t_{m,y}$ [mm]	$t_{m,x}$ [mm]	ℓ [mm]	E_{exp} [MPa]	E_v [MPa]	f_{exp} [MPa]
¹ BRE1	1530	55	250	110	1545	10	10	8	2035	2067	13.5
¹ BRE2	1530	55	250	110	1365	10	10	12	2310	2280	13.2
² BOF1	1122	61	257	126	149	13	13	3	743	743	2.9
² BOF2	1122	61	254	125	149	13	13	3.2	767	762	3.1
² BOF3	1122	61	258	126	149	13	13	3.4	785	780	3.0
² BOF4	1224	49	265	129	143	13	13	6.7	1120	1121	2.5
² BOF5	1224	49	259	125	143	13	13	6.7	1091	1121	2.8
² BOF6	2215	46	251	131	143	13	13	5.1	1225	1220	2.7
³ DRO1	4200	45	290	140	125	10	10	1	729	738	12.0
³ DRO2	4200	45	290	140	225	10	10	1	1181	1195	13.7
⁴ FRT1	7500	40	65	40	220	20	20	3	878	874	9.0
⁴ FRT2	7500	40	65	40	220	10	10	3	1938	2000	3.9
⁵ GUM1	3372	75	230	105	5450	12.5	14	15	4824	4883	8
⁵ GUM2	3372	75	230	105	7083	12.5	14	19	5232	5248	9.4
⁵ GUM3	3372	75	230	105	8568	12.5	14	17	5024	5068	12.2
⁶ HOS	12930	36	123	60	3270	10	10	0.2	8000	8064	18.2
⁷ LL01	13595	140	290	70	7976	10	10	7	15047	15060	20.4
⁷ LL02	13595	140	290	70	5102	10	10	0.1	10958	12284	12.3
⁷ LL03	4003	140	290	45	7976	10	10	40	6042	5999	14.4
⁷ LL04	4003	140	290	45	5102	10	10	40	5964	5998	11.1

¹(Brenchich et al., 2008), ²(Boffill et al., 2019), ³(Drougkas et al., 2016), ⁴(Furtmüller and Adam, 2011), ⁵(Gumaste et al., 2007), ⁶(Hossain et al., 1997), ⁷(Llorens et al., 2019) * w is the wall thickness.

Experimental campaigns of masonry prisms and wallettes tested in vertical loading were collected from the literature. Herein those relevant tests that presented the material characterisation data needed for the application of GREHM, namely the mechanical properties of both the brick units and mortar, were selected and

the relative experimental values of the vertical elastic modulus E_{exp} and the compressive strength f_{exp} are presented in Table 4 and Table 5 (ten different experimental campaigns resulted in 23 different masonry types). The calibrated value of ℓ to achieve the highest possible consistency with the experimental values and the vertical homogenised modulus E_v according to GREHM are also provided.

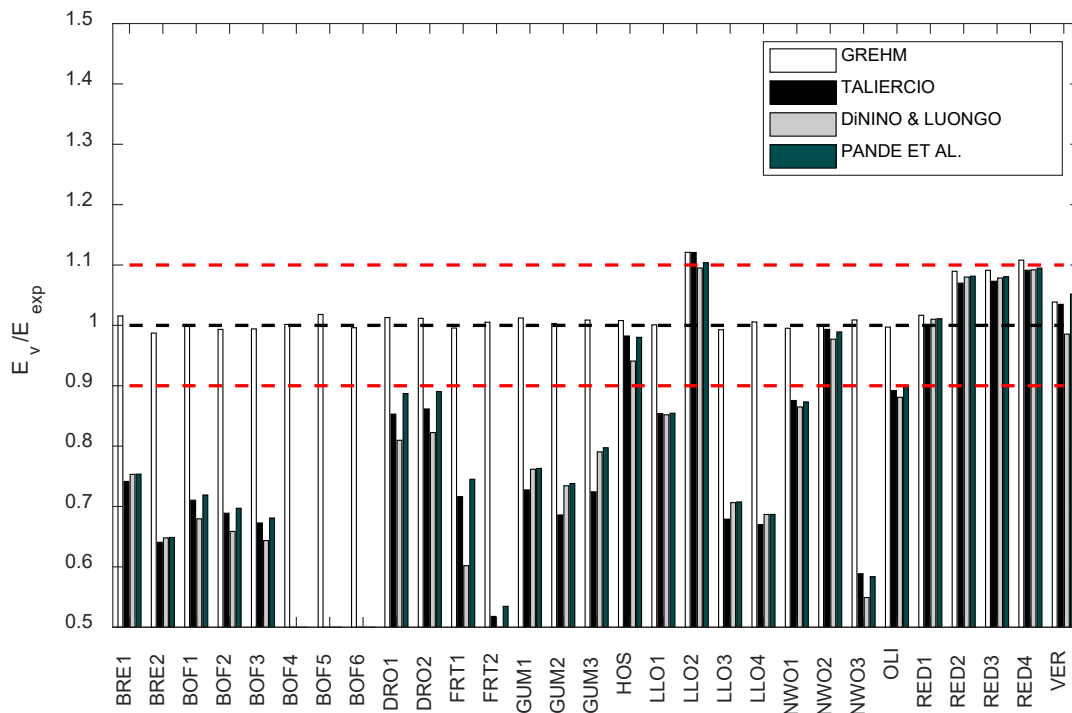
Table 5. Experimental testing of masonry walls: main parameters of brick units and mortar joints.

⁸ NW01	8490	72	224	106	3900	10	10	2	8410	8370	13.5
⁸ NW02	8490	72	224	106	3450	10	10	0	7210	7206	11.5
⁸ NW03	8490	72	224	106	750	10	10	4	6610	6670	10.6
⁹ OLI	12000	45	285	130	4200	10	10	1.1	10000	9972	28.6
¹⁰ RED1	8000	100	305	143	6600	6	6	0.1	7800	7930	3.2
¹⁰ RED2	8000	100	305	143	6600	12	12	0.1	7200	7846	3.3
¹⁰ RED3	8000	100	305	143	6600	20	20	0.1	7100	7748	3.5
¹⁰ RED4	8000	100	305	143	6600	30	30	0.1	6900	7646	3.6
¹¹ VER	16700	52	210	100	2100	13	13	0.1	6800	7063	-

⁸(Nwofor, 2012), ⁹(Oliveira et al., 2007), ¹⁰(Reddy et al., 2009), ¹¹(Vermeltfoort et al., 2007).

* w is the wall thickness.

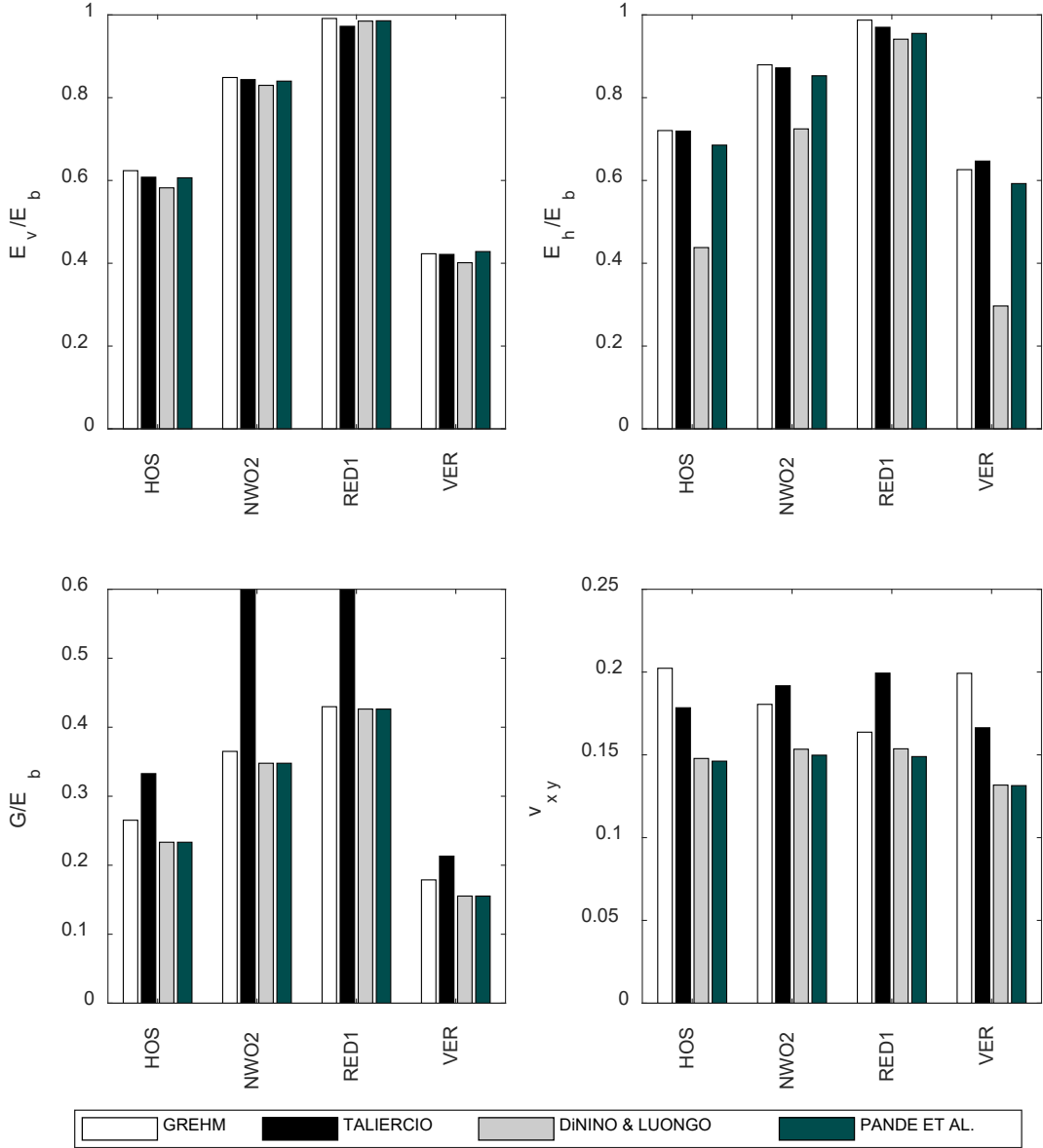
Figure 15. Comparison of vertical elastic modulus E_v between the proposed GREHM and the models of (Taliercio, 2014), (Di Nino and Luongo, 2019), and (Pande et al., 1989) for the considered experimental values E_{exp} : the red dashed lines at $\pm 10\%$.



The comparison of the models is presented by means of the ratio between the analytical E_v to the experimental E_{exp} elastic modulus in the vertical direction (data given in Table 4 and Table 5), as illustrated in Figure 15. The homogenised properties applying GREHM can be estimated fast using the normalised graphs of

Figure 6-Figure 8. It is noted that the limits of the vertical axis of Figure 12 have been kept between 50% and 150% for better readability although a higher difference appeared in some cases. In general the proposed GREHM is more precise while the other models estimate lower values of the elastic modulus. The total error (i.e. root of the sum of squares over the total number of samples) across the 23 experimental tests is 0.74% for GREHM, 5.70% for (Di Nino and Luongo, 2019), 5.47% for (Taliercio, 2014) and 5.22% for (Pande et al., 1989).

Figure 16. A comparison between GREHM and the models of Taliercio (Taliercio, 2014), Di Nino and Luongo (Di Nino and Luongo, 2019), and Pande et al. (Pande et al., 1989) for the elastic modulus in the horizontal direction E_h , the shear modulus G and the Poisson ratio ν_{xy} .



Source: (L. A. S. Kouris et al., 2020).

As can be seen in Figure 12 for the specimens HOS (Hossain et al., 1997), NWO2 (Nwofor, 2012), RED1 (Reddy et al., 2009) and VER (Vermeltoort et al., 2007) (see Table 4 and Table 4 for the details of the tests) all the models estimate very similar values. In particular for those tests the estimation of the internal length ℓ becomes minimum and a further comparison between the models is shown in Figure 16 for the elastic modulus in the horizontal direction E_h , the shear modulus G and the Poisson ratio ν_{xy} . This is a purely

analytical comparison of the homogenised values as these quantities had not been measured in relevant tests. As can be seen GREHM appears to give slightly higher values for E_v for the first three tests and for the fourth one it is (Pande et al., 1989) to be higher. This tendency remains generally also for the other quantities apart from the shear modulus G where (Taliercio, 2014) increases. This comparison shows a general consistency between the models for these experiments.

4 Numerical simulations and analyses of reinforced masonry with TRM

Traditional and cultural heritage buildings need advanced models for seismic analysis and strengthening. A model for reinforced masonry with TRM should consider all the constituents and their interactions. URM piers in general can fail due to crushing or rupture of the units and/or the mortar or, due to failure of their cohesion. The external coat of the TRM interacts with masonry and complicated bonding and interaction phenomena among them appear and numerous damage modes can occur. An FE model to be able to describe them converts the partial differential equations (PDEs) into matrix analyses. Two approaches there are to solve the matrices: (i) the implicit method based on the inversion of stiffness matrices to get the displacements and, (ii) the explicit method based on the inversion of mass matrices to get the accelerations. The former method is an iterative solution where each step solution depends on the previous one and suits for static or, time-independent problems. The latter method is also an iterative method but contrary to the previous, the solution of each step is used to define the displacements of the next step. Therefore, such an approach needs smaller time steps and suits well for dynamic loads, or time-dependent problems. The former method has the merit of being unconditionally stable while, the latter demands less computational effort as the mass matrix being diagonal is easily invertible and suits for highly non-linear problems. In this simulation approach two models are developed: an implicit model for quasi static problems and an explicit model for dynamic loading. Below the developed methods are presented and analyses are carried out.

Box 6. Implicit and explicit models

Two simulation approaches are proposed here for modelling traditional and cultural heritage buildings: (i) an implicit one for quasi-static loads, and (ii) an explicit one for dynamic loads. The former method has the merit of being unconditionally stable while, the latter demands less computational effort as the mass matrix being diagonal is easily invertible and suits for highly non-linear problems.

4.1 Implicit simulation of TRM reinforced masonry

4.1.1 Description of the model

In this modelling approach some simplifications are necessary to reduce the complexity of the simulation to an affordable cost. First of all, the masonry is treated using its homogenised properties taking advantage of the model of the previous chapter. Then, the interaction between the textile and the reinforcing mortar is macroscopically simulated using macro-indices to reflect the bonding behaviour of the textile in the TRM. This is a deliberate choice to keep the numerical problem in an affordable implicit analysis cost and to avoid the exact description of properties which otherwise would need profound investigation. For a more detailed description the reader is referred to the paper (Kouris et al., 2023).

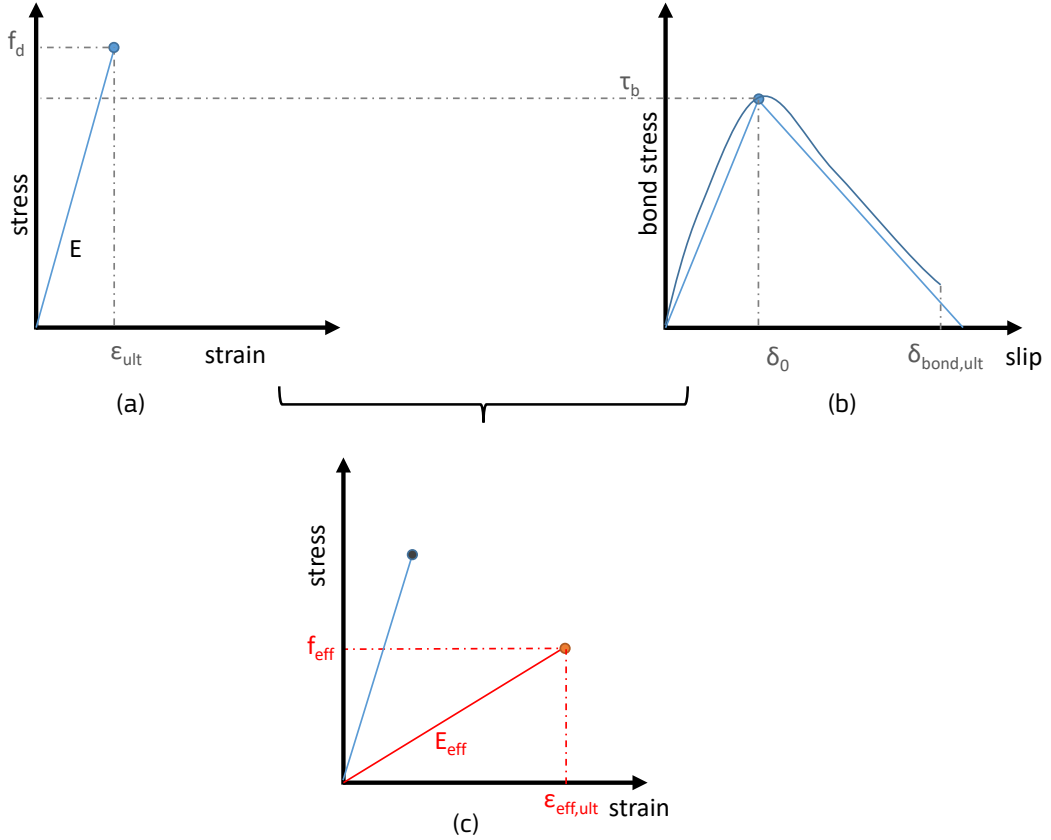
4.1.1.1 Parameters of TRM layers

The reinforcing layer of TRM is applied externally on either or both sides of a wall. The response a TRM coat defined in coupon tests is generally assumed to be trilinear (Kouris and Triantafillou, 2018) as shown in Figure 2, where the three subsequent phases I, II_a and II_b are characterised by the moduli E_1 , E_2 ($=0$) and E_3 .

The textile in the mortar is simulated using rebar sub-elements. These sub-element stiffnesses are overlaid onto the parent mortar elements in which they reside, but do not have separated degrees of freedom, and therefore have strain compatibility with the mortar. In reality however, this is not the case, as a slip bond occurs between yarns and the matrix and in the macro-scale this local-scale loss of bonds appears as reduced stiffness and strength of the textile. Although the bond behaviour has been the focus of several recent experimental and analytical studies e.g. (Carozzi et al., 2017; Larrinaga et al., 2014; Raoof et al., 2016; Veljkovic et al., 2020) the topic still remains open and the applications of an implicit model would be dramatically limited by the increased complexity of all the interfacial properties, let alone the testing procedures needed to define them. Hence, to take into account the non-directly simulated local slip phenomena macro-factors are introduced limiting the elastic modulus and the strength of the textile. These macro-indices are defined in three steps (Figure 17): first, the textile stress-strain behaviour is simplified into a linear behaviour (Figure 17a). The actual and complex interaction process between filaments, yarns, and the matrix takes place together with an uneven stress distribution of the fibres microscopically; all these interactions result in several micro-cracking and micro-debonding phenomena (Kouris and Triantafillou, 2018) which in the macro-scale appear as a telescopic debonding. Then, the macroscopic slip is simulated as a

bilinear curve (Askouni and Papanicolaou, 2019, 2017) as shown in Figure 17b. A thorough description of the several steps that the debonding undergoes with increasing load can be found in (D'Antino et al., 2014).

Figure 17. The modelling approach for bond slip phenomena in TRM: (a) a linear textile response, (b) a bilinear bonding response, and (c) the effective linear textile response.



Source: (Kouris et al., 2023).

In the third step, the macroscopic slip δ_{bond} is turned into a strain ε_{bond} using the fibre length L : $\varepsilon_{bond} = \delta_{bond} / L$. The effective strain of the fibre ε_{eff} is the sum of the linear one and ε_{bond} . Therefore, the effective elastic modulus and the effective strength of the textile can be defined as follows:

$$\begin{aligned} \varepsilon_{eff} &= \varepsilon + \varepsilon_{bond} \\ E_{eff} &= \frac{\sigma}{\varepsilon_{eff}} \\ f_{eff} &= E_{eff} \cdot \varepsilon_{eff,ult} \end{aligned} \quad (14).$$

In Equation (14) the ultimate strain is denoted as $\varepsilon_{eff,ult}$ and is the minimum of the sums:

$$\varepsilon_{eff,ult} = \min\{\varepsilon_{ult} + \varepsilon_{bond} | \varepsilon + \varepsilon_{bond,ult}\} \quad (15)$$

where the ultimate strains ε_{ult} and $\varepsilon_{bond,ult} = \delta_{bond,ult} / L$ are defined in Figure 17a and b respectively. Applying these empirical rule the loss of the cohesion and the consequent slip of the textile inside the reinforcing mortar is included within an effective elastic modulus and strength of the textile representing both phenomena: this schematically is shown in Figure 17c.

The Drucker-Prager plasticity model is used to simulate the compressive non-linear behaviour of the mortar. The model allows an isotropic hardening and softening of materials under compression. The evolution of the yield surface with non-linear deformation is defined based on the uniaxial compression yield stress, of the masonry assemblage. In this criterion, flow stress ratio R , dilation angle ψ , and friction angle β , need to be defined. The linear yield surface in the DP plasticity model is expressed as

$$F = t - \sigma_H \tan\beta - d$$

$$t = \frac{1}{2}q \left[1 + \frac{1}{R} - \left(1 - \frac{1}{R} \right) \left(\frac{r}{Q} \right)^3 \right] \quad (16a,b)$$

where in Eq. (16) σ_H stand for the hydrostatic pressure equal to 1/3 of the sum of the normal stresses in the 3 directions and q for the von Mises equivalent stress defined as follows:

$$q = \sqrt{\frac{3}{2} (\Sigma : \Sigma)}$$

$$\Sigma = \sigma + p I \quad (17)$$

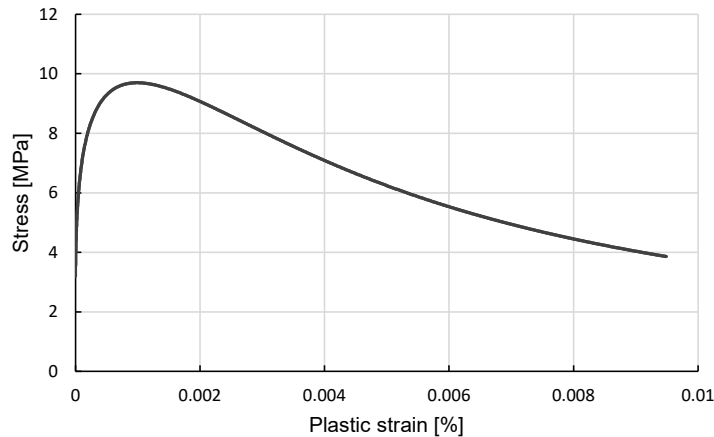
$$r = \left(\frac{9}{2} \Sigma \cdot \Sigma : \Sigma \right)^{\frac{1}{3}}$$

Finally, in Eq. (17) Σ is the deviatoric stress tensor and p the hydrostatic stresses.

4.1.1.2 Parameters of masonry

The FEM of masonry comprises masonry blocks representing the RVEs interconnected through interfaces. Each RVE is modelled using the homogenised properties: the elastic one derived using the GREHM and a concrete plastic-damage model (Lubliner et al., 1989). The latter plasticity law despite the fact that it has been developed specifically for concrete, it can be also used well for masonry or other brittle materials, with different plasticity and damage behaviour in compression and tension. For the uniaxial compression behaviour a law proposed for masonry specifically (Kaushik et al., 2007) is adopted and introduced in pairs of axial plastic strain ϵ_p vs. compressive stress σ . as shown in Figure 18.

Figure 18. The stress-plastic strain curve of masonry.



Source: (Kouris et al., 2023).

Therefore, the key parameters needed to define in the model are: (i) the elastic moduli and the Poisson's ratios, (ii) the dilation angle, ψ , in the p–q plane (estimated as 15 degrees), (iii) the flow potential eccentricity, ϵ (assumed equal to 0), (iv) the ratio of initial equibiaxial compressive yield stress to initial uniaxial

compressive yield stress (estimated equal to 1.16 i.e. the default value), (v) the ratio of the second stress invariant on the tensile meridian to that on the compressive meridian (assumed as 2/3), and (vi) the viscosity parameter (assumed equal to 10^{-6}). Moreover, the post-cracking behaviour in tension and the tensile fracture energy is estimated from a sensitivity analysis of a URM pier. The FEM comprises masonry blocks representing the RVE interconnected through interfaces. The cohesive elements in the interfaces are introduced using the command `*Contact Pair` where the surfaces in contact are defined and their properties. Details about the properties of the contact surfaces are specified below using the command `*Surface Interaction` followed by the out-of-plane thickness (defined as 1 m).

The dilatancy angle of masonry is the ratio of the perpendicular displacement to the one parallel to the joints for a wall in shear load. It controls the amount of plastic volumetric strain developed during plastic shearing and is assumed constant during plastic yielding. However, the dilation phenomena in masonry are complex related to the asperity and roughness of the developed cracks in mortar joints due to shearing loads (Stupkiewicz and Mróz, 2001). The dilatancy angle is not constant during loading (Stupkiewicz and Mróz, 2001) and it has been shown that for extensive and cyclic shear loads to tend to zero (Lourenço and Ramos, 2004). Therefore, the angle of dilation ψ can be intuitively related to the angle of internal friction ϕ . For non-cohesive soils (i.e. sand, gravel) with the angle of internal friction $\phi > 30^\circ$ the value of dilation angle can be estimated as $\psi = \phi - 30^\circ$. A negative value of dilation angle is acceptable only for rather loose sands. The value of $\psi = 0$ corresponds to the volume preserving deformation while in shear.

The Drucker-Prager plasticity model is used to simulate the compressive non-linear behaviour of the mortar of the reinforcement. The model allows the isotropic hardening and softening of materials under compression. The adopted modelling approach requires the definition of the properties of the interface between the RVEs. The friction between the masonry prisms is defined equal to 0.7 kPa introduced and the slip tolerance is the default value 0.005. The behaviour of interfaces when overlapped is determined as hard (`*Surface Behavior`).

The cohesive behaviour is ruled through the traction separation stiffness: the elastic part of the response is governed by the stiffness in the normal plane K_{nn} and the stiffnesses in two perpendicular shear planes K_{ss} and K_{tt} . The respective values have been estimated from the experimental results and are equal to 4MPa/m, 40MPa/m and 40MPa/m. The response is before any damage is linear and after reaching the damage criterion is linearly decreased related to the scalar variable d as follows:

$$\mathbf{t} = \begin{Bmatrix} t_n \\ t_s \\ t_t \end{Bmatrix} = (1 - d) \begin{bmatrix} K_{nn} & 0 & 0 \\ 0 & K_{ss} & 0 \\ 0 & 0 & K_{tt} \end{bmatrix} \begin{Bmatrix} \delta_n \\ \delta_s \\ \delta_t \end{Bmatrix} = (1 - d) \mathbf{K} \cdot \boldsymbol{\delta} \quad (18).$$

The maximum stress criterion is adopted to characterise damage initiation:

$$\max \left\{ \frac{t_n}{t_n^0}, \frac{t_s}{t_s^0}, \frac{t_t}{t_t^0} \right\} = 1 \quad (19).$$

In Eq. (19) the tractions do not regard the compressive stresses (negative sign) on the fracture behaviour of the joints in the normal direction. Regarding the properties of the stiffness matrix of Eq. (18) these should correspond to the RVE's elastic properties as during the elastic response there is not relative movement at the interfaces. Using the RVE and given that the interfaces have no thickness the following simple homogenisation rule can be applied:

$$K_{nn} = \frac{E_u E_m}{t_m (E_u - E_m)} \quad (20)$$

where E_u , E_m are the elastic moduli of the units and the mortar and t_u is the thickness of the mortar joints.

4.1.2 Calibration of the model for out-of-plane loads

Applying the proposed FE model the specimens of the experimental campaign made by (Kariou et al., 2018) are modelled and a calibration of the slippage and bond loss of the textile is carried out. An 8-node reduced integration 3D FE element, namely the C3D8R element is used to model masonry elements, while the TRM is modelled using 3D shell elements with 4 nodes, namely the S4 element. Masonry blocks representing the RVEs are interconnected through interfaces. Attention is paid to match the location of nodes to improve the performance of interfaces.

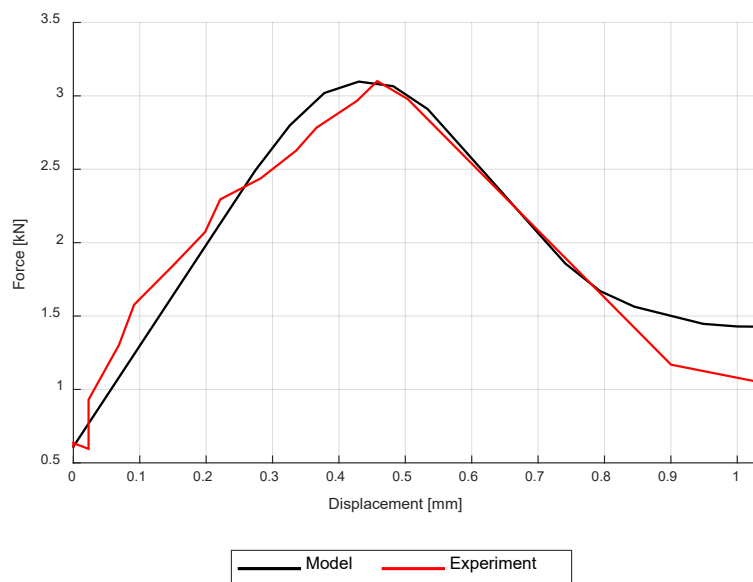
The specimens are discretised refinedly with FEs of close to unity aspect ratios to ensure accurate representation of stresses and strains. The specimens were supported by steel plates and rollers, with "zero" resistance to uplift and very high compression stiffness. The model does not consider the subgrade stiffness and instead a full restraint of the vertical DOFs along the support line is applied. Finally, a displacement-controlled load is applied directly to the nodes of the specimen instead of the steel plate.

4.1.2.1 Calibration of masonry properties

The parameters of the proposed model which were not experimentally found are fine-tuned carrying out a sensitivity analysis with the out-of-plane response of the control double-wythe specimen made of unreinforced masonry. The control specimen of single-wythe unreinforced masonry failed in its own weight (Kariou et al., 2018).

The post-cracking behaviour in tension is assumed to be related to the tensile strength equal to 0.5MPa while the tensile fracture energy equal to 0.25kN/m (Lourenço, 2000) was found precise. Furthermore, however, a dilation angle $\psi = 15^\circ$ was found to correlate well with the experimental results. Standard values for the other parameters are found alright: (i) the flow potential eccentricity, $\epsilon = 0$, (ii) the ratio of initial equibiaxial compressive yield stress to initial uniaxial compressive yield stress equal to 1.16, (iii) the ratio of the second stress invariant on the tensile meridian to that on the compressive equal to 2/3, and (iv) the viscosity parameter equal to 10^{-6} .

Figure 19. Comparison of the out-of-plane response of the unreinforced double wythe specimen with the analytical model.



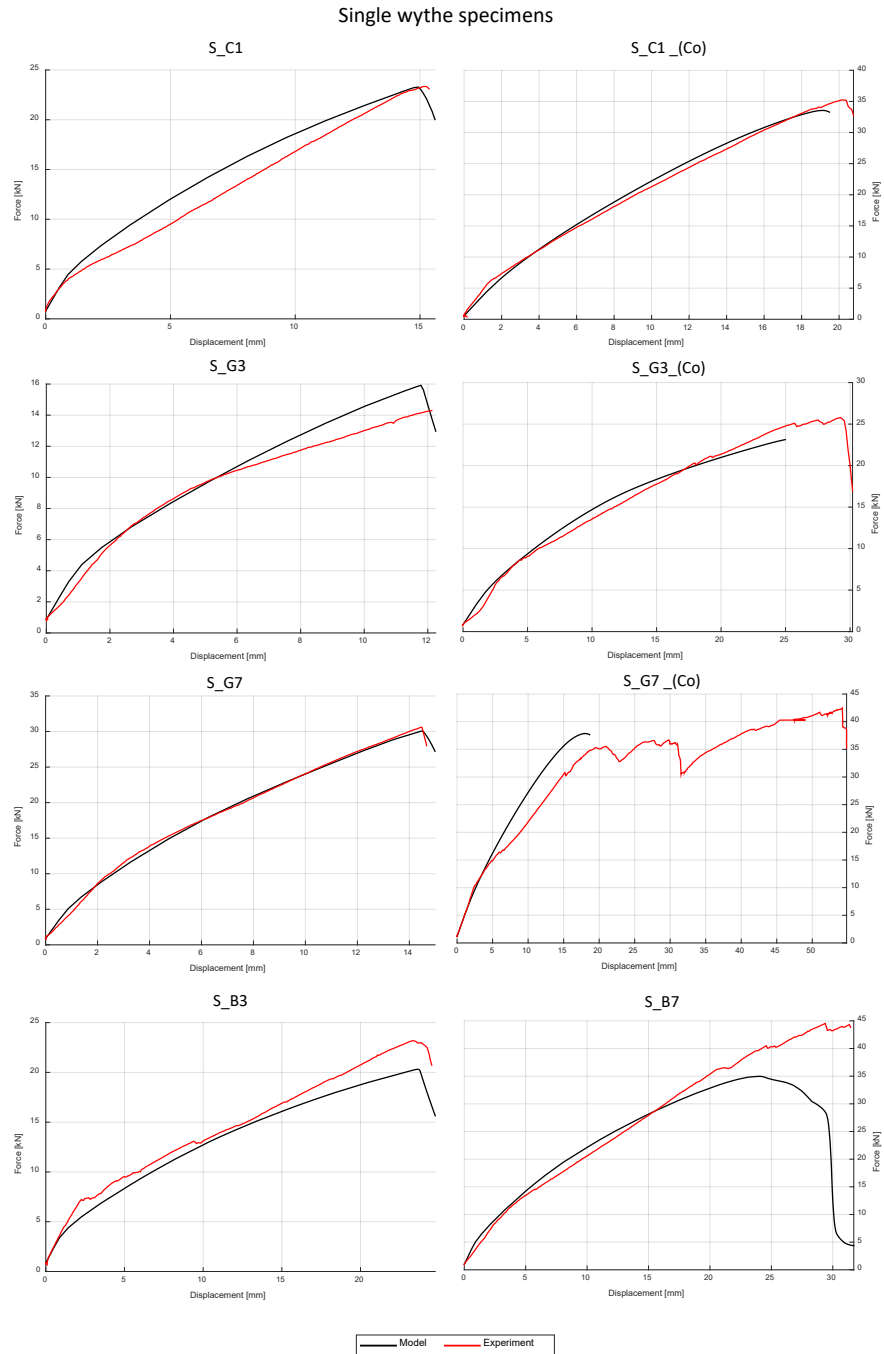
Source: (Kouris et al., 2023).

The comparison with the experimental response shown a very good agreement both in terms of strength and displacements. The softening behaviour is also captured sufficiently well (Figure 19).

4.1.2.2 Calibration of the textile bond behaviour

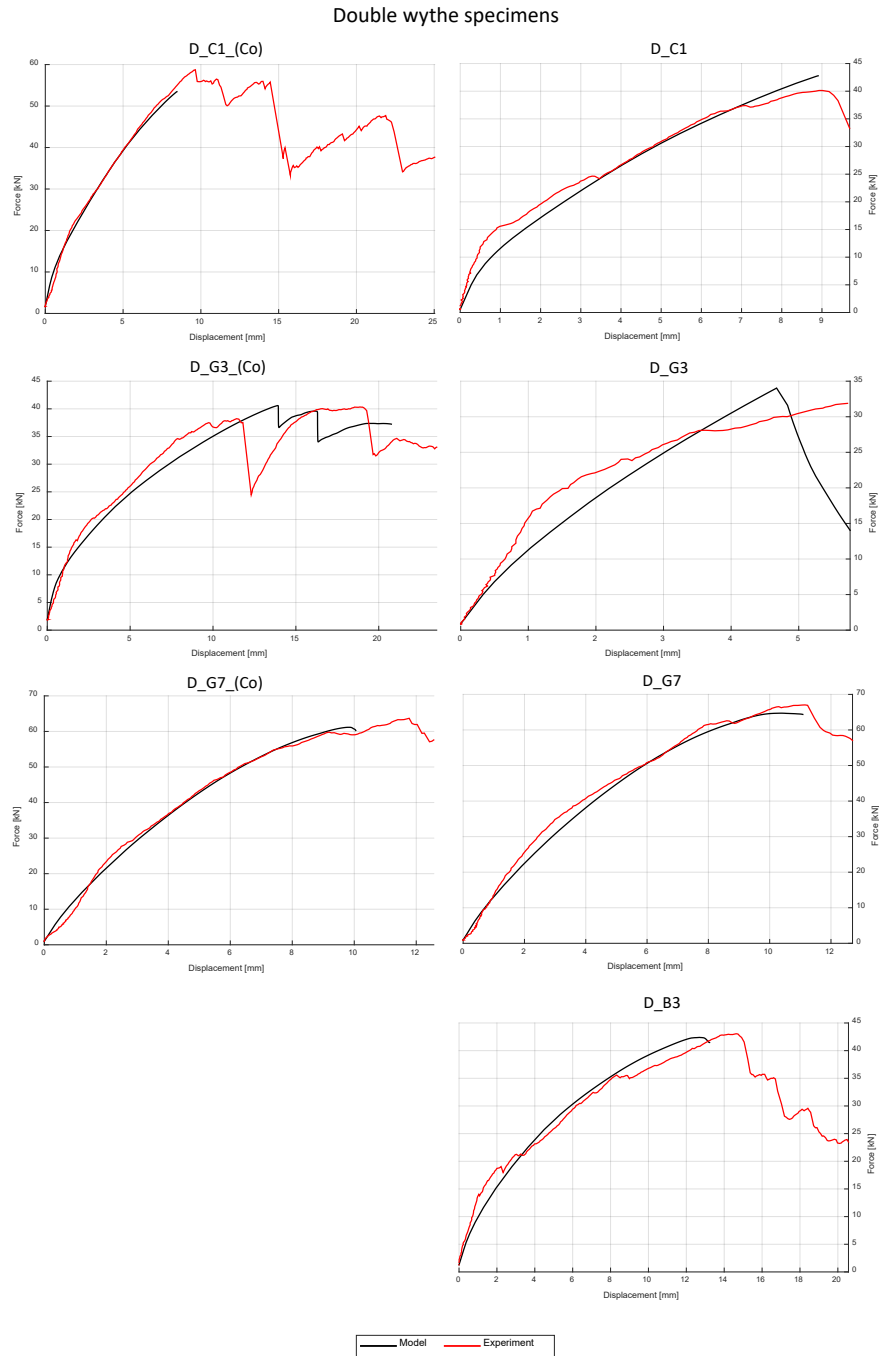
The elastic modulus E_T and the strength $f_{y,T}$ of TRM are calibrated using the experimental results. The effective properties of TRM reflect the simplifications of the simulation regarding the failure modelling; the failure of the bond between the textile and the matrix and the failure of the cohesion of the matrix have not been modelled. The effective properties of S TRM can account for these two failure modes.

Figure 20. Comparison of the out-of-plane response of the reinforced single wythe specimen with the analytical model.



Source: (Kouris et al., 2023).

Figure 21. Comparison of the out-of-plane response of the reinforced double wythe specimen with the analytical model.



Source: (Kouris et al., 2023).

4.1.3 Empirical equations for the reduction coefficients

Using the proposed model, the elastic modulus and the textile strength should be treated with their effective values depending on the bonding slip and the effective total strain (Eq. (14)). The imperfect bonding allows the textile to slip in the matrix up to the total loss of cohesion. This telescopic slippage (Banholzer et al., 2006) is mainly influenced by the external treatment of the textiles (coating) and the impregnation of the textile yarn with the surrounding inorganic matrix (Alecci et al., 2016). In addition to the latter the placement

of the textile can influence the bonding (Bertolesi et al., 2014). The impregnation as well as the placement of the textile are factors with a random nature. It should be noted that a slippage between the substrate and masonry is not commonly observed (D'Antino et al., 2014).

Apart from the external coating of the yarns the geometric and material parameters of the textile and the matrix which control the bonding are: (i) the radius r of the yarns, (ii) the distance w between the yarns number of layers, (iii) the thickness of the layer, (iv) the perpendicular distance between the yarns h , (v) the elastic moduli of the textile E_t and the matrix E_{mtx} , (vi) the tensile strength of the textile and the matrix, (vii) the number of layers, (viii) the volumetric ratio of the textile in matrix and (ix) the stress of the textile σ_t . The correlation coefficients of these parameters with the effective ratios of the elastic modulus and tensile strength of the textile reveal the most important ones which are included in the following unitless three coefficients:

$$\alpha = \frac{\sigma_t}{f_t}$$

$$\beta = \frac{\pi \cdot r^2}{w \cdot h_L} = \frac{t_{nom} \cdot No}{t_{coat}} \quad (21a,b,c)$$

$$\gamma = \frac{E_{mtx}}{E_t}$$

where No is the number of layers and t_{coat} is the total thickness of the TRM jacket. The relationship defining the ratio of the effective textile elastic modulus $E_{t,eff}$ and bonding slip follows the shape of the bond-slip model of embedded steel reinforcement in reinforced concrete structures (CEB-FIB, 2011):

$$\Omega_E = \frac{E_{t,eff}}{E_t}, \Omega_f = \frac{f_{t,eff}}{f_t} \quad (22a,b)$$

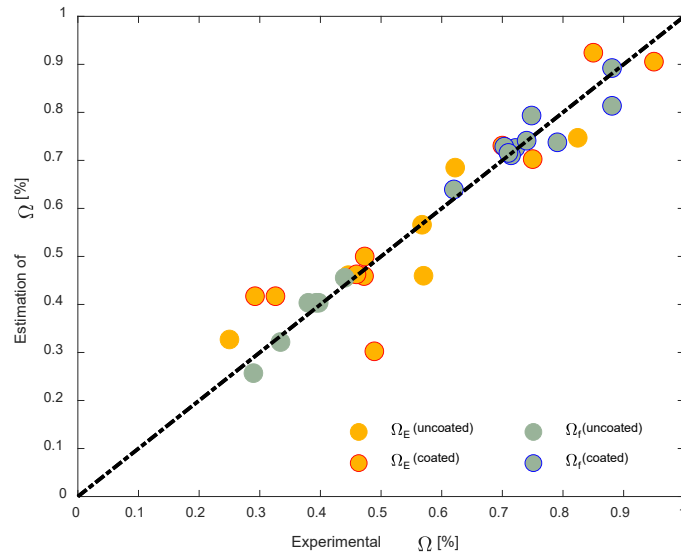
$$\Omega_{E,f} = 1 - \left(1 - e^{-p_1 \alpha^{-p_2 \beta}}\right) \ln \gamma^{-p_3}$$

where Ω is the reduction coefficient and p_1 , p_2 and p_3 coefficients given in. The comparison of the empirical model and the calibrated experimental values is shown in Figure 22 where a good performance of the selected reduction function is noted.

The coefficients of the empirical equations are given in Table 6. In this table the goodness-of-fit metrics, i.e. the R^2 and the p-values are provided. The empirical model is found to converge effectively with the data achieving robust determination values ($R^2 > 0.8$ and $p < 0.01$).

The variation of the empirical equation is easier interpreted in the 2D plots vs. the α , β coefficients. The empirical equation is bounded and for the experimental carbon and matrix properties this variation is between 0.3 and 0.9 as presented in Figure 24a. Obviously, the higher the tension that a fibre can sustain the higher would Ω_E be and consequently, as α increases the Ω_E coefficient increases. Moreover, the thinner nominal thickness (and respectively the yarn) the less influence has the tensile stress. This can be attributed to the degree of impregnation of the yarn; if the roving is thick then, it is made of several fibres and the degree of impregnation of the surrounding matrix in the inner fibres is low resulting in an uneven stress state. Due to this stress distribution, in Figure 24b it is seen that low stress receives a smoother variation of Ω_E in regard to the radius of the yarn whereas for high stresses the Ω_E coefficient degrades quickly.

Figure 22. Experimental vs. estimated values of Ω .



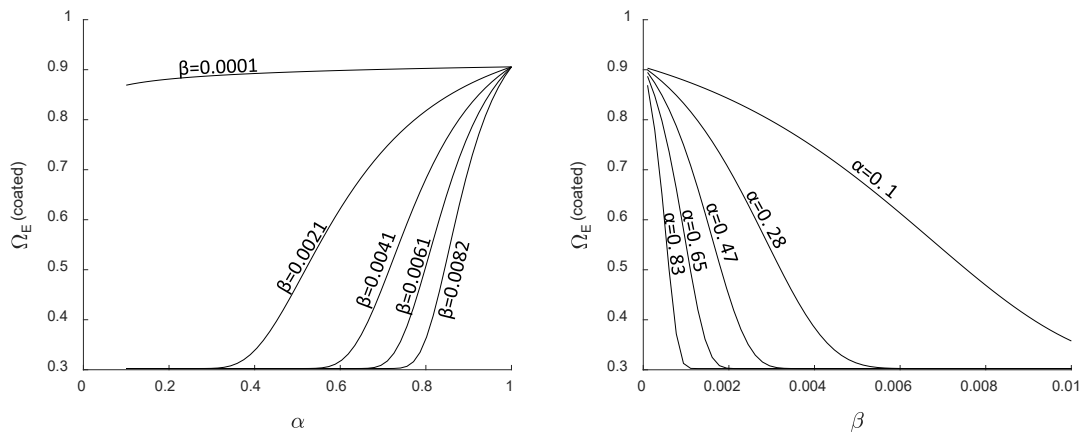
Source: (Kouris et al., 2023).

Table 6. Calibrated coefficients p_1 , p_2 , p_3 and regression metrics of the empirical Eq. (22) (Kouris et al., 2023).

	p_1	p_2	p_3	R^2	p-value
Ω_E (uncoated)	0.63	559	0.12	0.85	$3 \cdot 10^3$
Ω_E (coated)	0.15	1557	0.12	0.84	$2 \cdot 10^3$
Ω_f (uncoated)	2.34	2000	0.13	0.93	$2 \cdot 10^3$
Ω_f (coated)	3.35	277	0.06	0.94	$1 \cdot 10^3$

Source: (Kouris et al., 2023)

Figure 23. The variation of Ω_E vs. α and β coefficients.



4.1.4 Analyses for out-of-plane quasi-static loads

The parametric analysis investigates the effectiveness of a large range of textiles and matrices as reinforcing materials for out-of-plane loads which was not possible to consider in the experimental campaign. To this end, textiles with a varying strength from as low as 100 MPa to 2500 MPa (effective strength values) are applied to the masonry piers. The key parameter is the mechanical reinforcement ratio ω which varies largely (from 0.05 to 1) whereas in the experimental campaign varied from 0.03 to 0.43 as shown in Table 7.

Table 7. Experimental parameters.

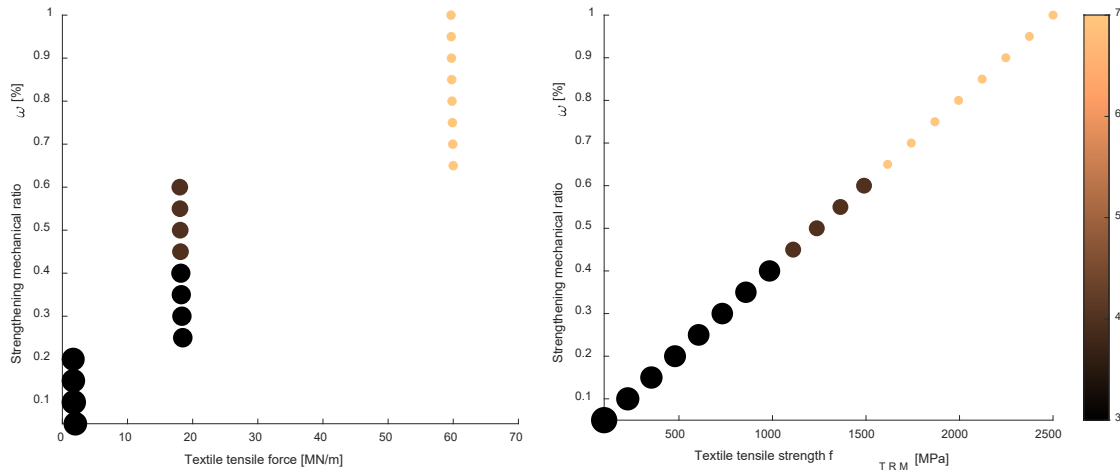
Specimen	Jacket thickness	ρ_w	ω_t	Max Force	Max displacement
	[mm]	[%]		[kN]	[mm]
S_C1	3	0.095%	0.35	23.4	15.6
S_C1_(Co)	5	0.095%	0.35	35.3	20.8
S_G3	4	0.129%	0.19	14.3	12.2
S_G3_(Co)	7	0.129%	0.19	25.8	30
S_G7	8	0.300%	0.43	30.6	14.7
S_G7_(Co)	9	0.300%	0.43	42.5	55
S_B3_(Co)	9	0.108%	0.15	23.2	24.7
S_B7_(Co)	13	0.253%	0.35	44.5	32.1
D_C1	3	0.045%	0.17	40.1	9.7
D_C1_(Co)	5	0.045%	0.17	58.8	14.9
D_G3	4	0.061%	0.09	32	5.8
D_G3_(Co)	7	0.061%	0.09	40.4	28.8
D_G7	8	0.143%	0.03	67.1	12.8
D_G7_(Co)	9	0.143%	0.21	63.8	16.2
D_B3_(Co)	9	0.052%	0.07	43.1	16.7
D_B7_(Co)	13	0.120%	0.17	66.2	13.6

Source: (Kariou et al., 2018).

The textile volumetric ratio varies also up to 0.49% whereas in the experimental campaign the corresponding values ranged up to 0.3 %. Each textile has its own texture with varying filament, roving and yarn areas, distances etc. The textile tensile force per metre versus the strengthening mechanical ratios is plotted in Figure 24. The reinforcement mechanical ratio ω is realised applying 20 different combinations of: (i) textile fibre strength f_{TRM} (as well as elastic modulus), (ii) yarn areas, and (iii) number of layers as shown in Figure 24.

Obviously, lower strength textiles resemble those made from natural fibres and have thicker yarns while, higher number of layers (e.g. 3 or more) are more common for composite textiles.

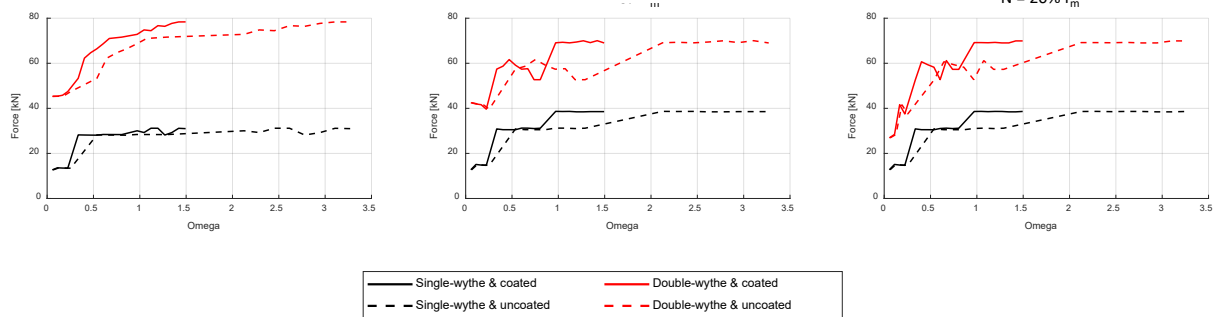
Figure 24. Textile properties for parametric analyses with varying mechanical ratios combining a range of textile strengths, yarn area (area of the points), and number of layers (colour of the points, see colourbar).



Source: (Kouris et al., 2023).

Moreover, the axial load is included in the investigation. The axial load has not been considered in the experiments due to increased set-up complexity, but real piers carry gravity loads. Therefore, two levels of axial loads are considered: (i) 10% of the axial pier capacity and, (ii) 20% of the axial pier capacity as common masonry buildings can exhibit. In this parametric analysis the piers configuration remains as the one of the experimental campaign to serve as reference for validation.

Figure 25. Maximum vertical load of piers out-of-plane loaded for 3 levels of vertical load: (a) $N = 0$, (b) $N = 10\% f_m$, and (c) $N = 20\% f_m$.



Source: (Kouris et al., 2023).

For the previous parameters and employing the proposed FE model, a parametric analysis is carried out. To estimate the nominal elastic modulus and the textile strength from their effective values Eq. (22) is applied. The results of the analyses are summarised in Figure 25: small variations for the three levels of axial load can be seen. For the single-wythe piers the axial load can lead to a slightly higher capacity for heavily strengthened jackets with ω higher than 1. Obviously, uncoated textiles add lower capacity to the piers. Generally, even low strength textiles (e.g. made from natural fibres) resulting to as low values of ω as 0.05 to

0.1 approximately can add a substantial increase of the out-of-plane pier capacity which can be around 5 times the capacity of the unstrengthened pier without axial load. The out-of-plane capacity increases with ω but then, it reaches a plateau value which does not alter substantially. This value for the single-wythe piers is 0.25 approximately for the uncoated textiles and 0.5 for the coated ones and for the double-wythe piers the respective values are 0.5 and 1 approximately.

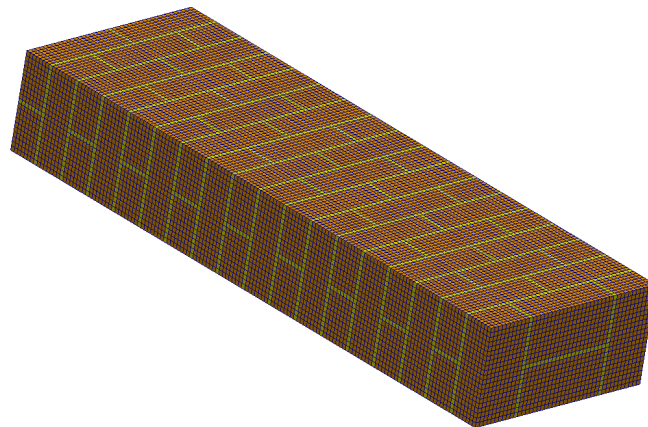
4.2 Explicit simulation of TRM reinforced masonry

4.2.1 Parameters of the model

An explicit model is also developed for the cases where the nature of the load is dynamic. The reader is referred to (L. A. Kouris et al., 2020) for more details on this topic. The FE simulations were carried out using the explicit finite element solver EUROPLEXUS (EUROPLEXUS, 2019) jointly developed by the French Commissariat à l'Energie Atomique et aux Energies Alternatives (CEA Saclay) and the European Commission's Joint Research Centre (JRC Ispra). The main application domain of the software is numerical simulation of fast transient phenomena including non-linear effects, such as explosions and impacts in complex three-dimensional fluid structure systems and therefore, suits perfectly for the masonry blast analysis applied here.

The numerical model of the masonry wall was discretized by 8-node linear brick elements with reduced integration to avoid locking phenomena. A uniform element size of 1cm was opted for to also resolve the mortar joints, see Figure 26. The TRM layer has been modelled with 4-node shell elements with 6 DOFs per node, 4 integration points in the plane and 5 integration points through the thickness. A similar element size of 1cm has been employed for the TRM layer which is sharing common nodes with the masonry wall in order to take into account the bonding between the two different components. The specimen was constrained along the vertical direction (parallel to the load) at the support locations. For the quasi-static tests the load has been implemented somewhat faster (constant velocity of 0.05m/s), using time scaling which implies that the simulation ran during a shorter time interval than the duration of the physical process of the test. Time scaling increases the strain rates in the structure, therefore rate-sensitivity has been deactivated from the constitutive model.

Figure 26. Numerical model of the masonry wall.



Source: (L. A. Kouris et al., 2020).

The mortar and the bricks exhibit a brittle behaviour, therefore a three-invariant cap model with mixed hardening has been used (Kristoffersen et al., 2018). It includes strain rate sensitivity and isotropic damage, and has been successfully employed in previous studies representing concrete structures (Guilbaud, 2015). For the TRM layer a Von Mises material law has been used, where elasto-plasticity with isotropic hardening is implemented via a radial return algorithm.

Failure was modelled using element erosion (element excluded from the calculation for the remaining period) that is triggered when all the integration points in the respective element reach a critical value related with the constitutive law. For the brittle material law, the volumetric plastic strain has been used as a failure criterion, while the threshold has been defined after appropriate parametric studies. For the TRM, a criterion based upon the principal strains has been engaged. The criterion is active when the hydrostatic stress is positive (traction), while when the hydrostatic stress is negative (compression) failure is inactive.

4.2.2 Calibration of the model

The numerical model and the assumptions described in Section 3 are applied to the masonry single and double wythe specimens of the experimental campaign presented in Section 2 to calibrate the effective material properties. The calibrated material properties for both specimens retrofitted with a carbon TRM layer are presented in Table 8 and Table 9. It is noted that a uniform weight is applied to all materials as the analysis is explicit. Masonry and mortar joints are modelled using a concrete NL material law applying a Drucker-Prager strain threshold (EUROPLEXUS, 2019).

Table 8. Material parameters for brittle constitutive law.

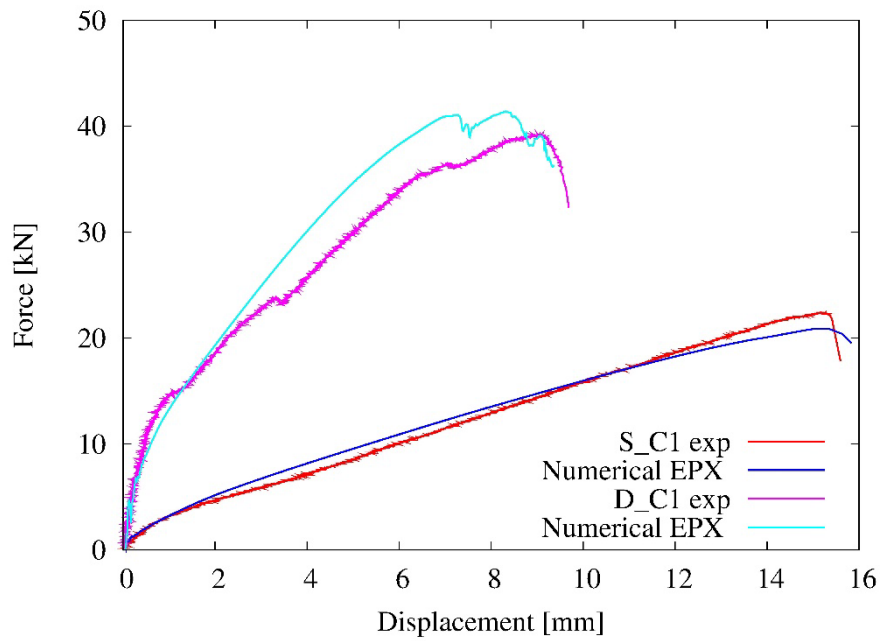
Material	Density [kg/m ³]	Young modulus [GPa]	Poisson ratio	Compressive strength [MPa]	Tensile strength [MPa]	Volumetric strain threshold
Brick	2000	6	0.3	15	1.5	0.2
Mortar	1800	0.4	0.2	5	0.5	0.1

Table 9. Effective material parameters for the carbon TRM layer.

Density [kg/m ³]	Young modulus [GPa]	Poisson ratio [-]	Elastic limit [MPa]	Ultimate stress [MPa]	Ultimate strain [%]
3650	225	0.2	250	1600	1.5

The calibration of the effective material parameters for the carbon textile is shown in Table 9 and the comparison between analytical and experimental results are presented in Figure 27 where an excellent matching is observed. Failure is calibrated with high accuracy in both cases as well as the initial stiffness. A reasonably small variation of the stiffness is observed for the double wythe masonry specimen which can be attributed to local aleatory bonding imperfections.

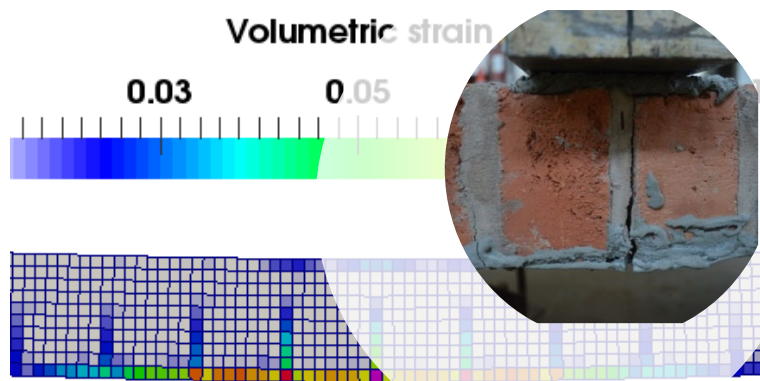
Figure 27. Comparison between experimental results of single (S_C1) and double wythe (D_C1) masonry and numerical model (EPX).

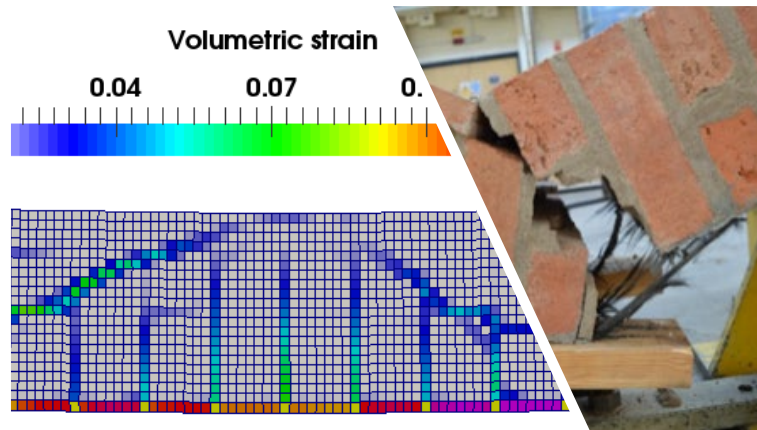


Source: (L. A. Kouris et al., 2020)

Moreover, comparing the failure mode and the crack propagation among the experimental specimens and the numerical models show a reasonably accurate coincidence as depicted in Figure 28.

Figure 28. Failure mode of experimental specimens and analytical representation.



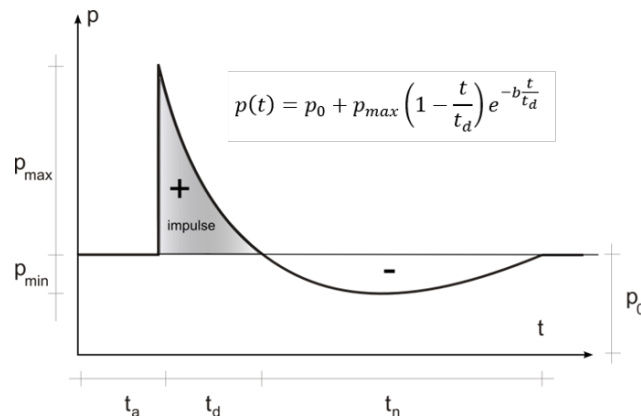


Source: (L. A. Kouris et al., 2020)

4.2.3 Analysis for dynamic loading from explosions

An idealized form of a blast pressure-time curve at a certain distance from the detonation point and without intermediate obstacles is presented in Figure 3. The shock wave first reaches the point under consideration at the arrival time t_a (which includes the time of the detonation itself). The pressure reaches its maximum value p_{max} (peak-overpressure) almost instantly and starts decaying until it reaches the ambient pressure p_0 (in most cases the atmospheric pressure) within time t_d , called the positive phase duration. The pressure continues to drop below the ambient pressure reaching its minimum value p_{min} , and then starts to rise again reaching the ambient pressure within time t_n , known as the negative phase duration. The exponential decay of the pressure-time history is represented through the modified Friedlander equation (Baker, 1983), that describes the rate of decrease of the blast pressure values. Depending on the distance of the obstacle from the detonation point and the mass of the explosive charge, the desired parameters (time of arrival, pressure magnitudes, duration and impulses) can be defined using the graphs included in (Kingery and Bulmash, 1984).

Figure 29. Idealized form of pressure-time history due to explosion (Friedlander equation (Baker, 1983)).



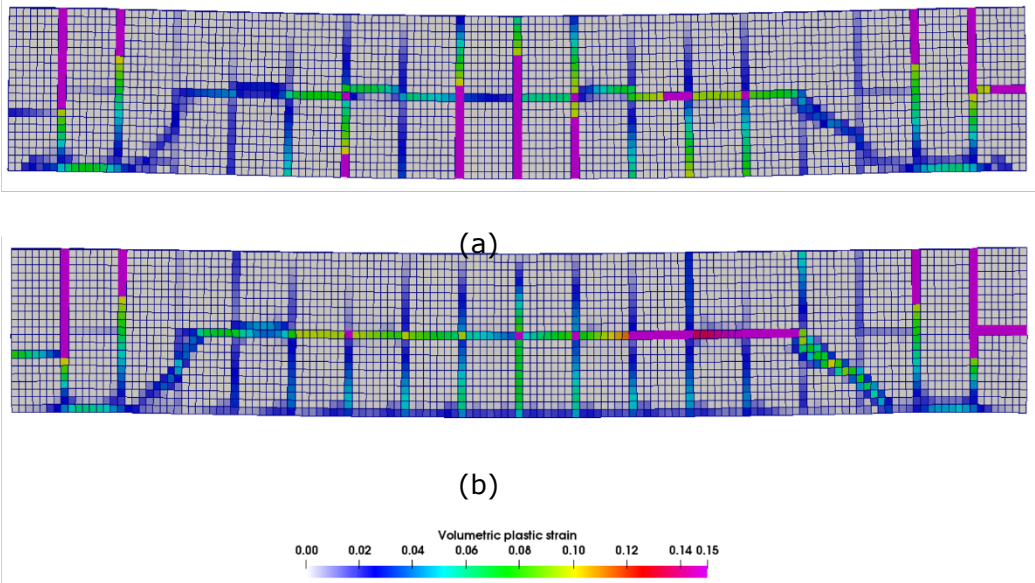
Source: (L. A. Kouris et al., 2020)

A hemispherical blast wave produced from a 80 kg TNT charge at a standoff distance of 5m has been considered to impinge the upper surface of the wall. This scenario implies a Hopkinson-Cranz scaled distance of $1.16 \text{ m/kg}^{1/3}$ according to the following Equation:

$$Z = R/\sqrt[3]{W} \quad (23)$$

where R is the standoff distance and W is the charge mass.

Figure 30. Damage states for: (a) unreinforced masonry, and (b) retrofitted masonry with TRM.



Source: (L. A. Kouris et al., 2020).

The materials comprising the masonry wall behave differently under impulsive loading when compared to static or quasi-static loading, due to the effect of the increased strain-rates. Figure 30 presents the comparison of the masonry wall response under blast loading with and without TRM enhancement. The magenta coloured zones indicate the eroded elements after reaching their maximum limit. More accurate representation of the crack propagation needs finer discretisation, but the current one is sufficient to extract qualitative conclusions.

The additional TRM layer appears to prevent the extensive cracking of the mortar. In fact, the opening of the mortar bed joints in the middle zone due to tensile failure is prevented allowing for an additional masonry arch mechanism to develop which, however, is still far from high plastic strains. This additional arch mechanism appears with a moderate diagonal cracking and a compression zone in the middle mortar head joints. Moreover, this mechanism relieves part of the stress and strain tension at the supports.

Monitoring of the number of the failed elements for each case, reveals that the TRM enhanced wall has 20% less eroded elements that is a clear indication of damage reduction. The TRM is not exfoliated, keeping together the individual components of the wall, a characteristic that can contribute towards the reduction of the potential flying debris and their lethal consequences, and thus, increase substantially the safety of the structure.

5 Assessment of the combined retrofitting in city scale

This chapter investigates the application of the combined energy and seismic retrofitting on masonry buildings at a city level across different locations in Europe with a range of combinations of seismic hazard and climatic conditions and assesses its potential benefits. For a broader analysis including other types of buildings the reader is referred to (Pohoryles et al., 2020) and for RC buildings specifically to (Pohoryles and Bournas, 2021). Indeed, in the following study the focus is only on masonry buildings but when the losses are estimated at a city level the total building stock is considered. Representative existing masonry buildings from various construction periods have been selected reflecting typical building characteristics from a thermal and structural point of view and the targets for energy and seismic retrofitting were determined for four climatic and seismic zones. The retrofitting scheme combining thermal and structural upgrade for the building envelope is applied to reach the respective performance targets close to those set by modern codes. The buildings' energy demand and seismic safety before and after retrofitting are assessed for the different climatic and seismic scenarios, leading to a large-scale assessment of the building stock using a combined metric, namely the *expected annual loss*.

5.1 Studied cities and buildings' population

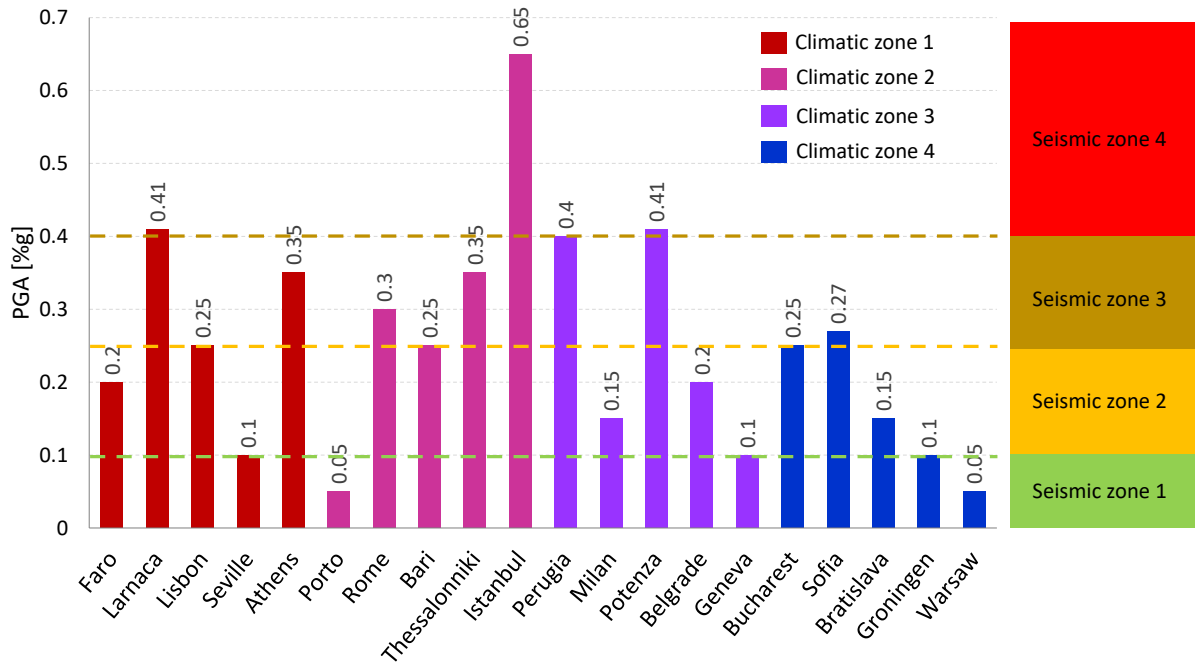
Twenty European cities located in areas of different seismic hazard and climatic conditions were selected as case study locations to investigate the impact of the combined energy and seismic retrofitting. Those cities are grouped in four climatic and seismic zones. As shown in Table 10, the climatic zones were classified by heating degree-days (HDD), a weather-based index representing the difference between a base temperature and a day's mean temperature. A base temperature of 18°C was chosen to calculate the HDD values for this study. The outdoor air temperature was adopted from EnergyPlus (US Department of Energy, 2010) generated from a period of climate record of 30 years.

Table 10. Matrix of case study cities by seismic risk (PGA) and climatic condition (HDD).

	HDD			
PGA	HDD≤1200	1200<HDD≤2200	2200<HDD≤3000	3000<HDD≤4000
PGA ≤ 0.10	Seville	Porto	Milan/Geneva	Bratislava/Warsaw/ Groningen
0.10 < PGA ≤ 0.25	Faro	Bari	Belgrade	Bucharest
0.25 < PGA ≤ 0.40	Lisbon/Athens	Rome/Thessaloniki	Perugia	Sofia
PGA >0.40	Larnaca	Istanbul	Potenza	

The seismic zones were defined on the basis of the expected peak ground acceleration (PGA) for a return period of 475 years (10% exceedance in 50 years). Gas extraction induced earthquakes in Groningen area were also considered assuming a PGA value of 0.1g (Dost et al., 2017). The values vary from as low as 0.05g to 0.65g (Pagani et al., 2018) divided in four zones from low to high seismicity as illustrated in . For each climatic zone there is at least one city in each seismic zone apart from the coldest zone (3000<HDD≤4000) where no city exists in Europe with high seismic hazard (PGA >0.40).

Figure 31. The seismic hazard in PGA values (%g) per city.

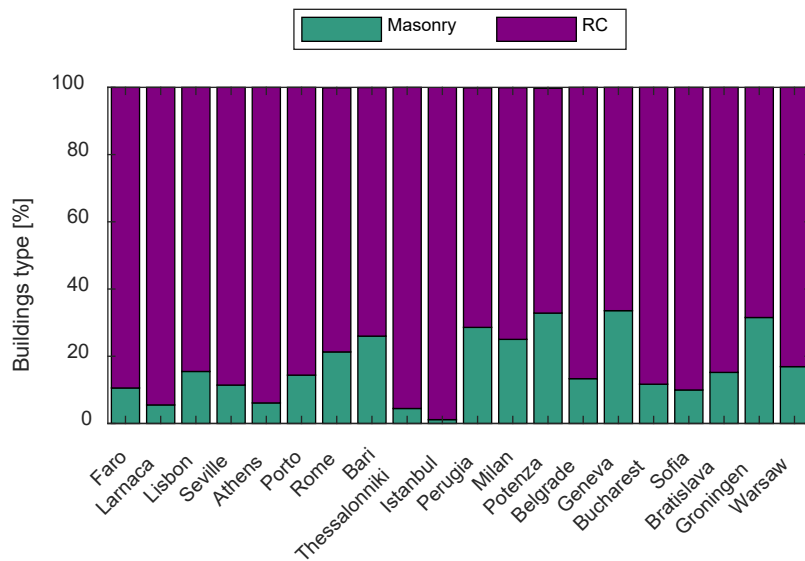


The residential sector constitutes the major share (75%) of the EU building stock. In many European countries over half of the residential building stock was built before the 1970s and hence does not comply with modern energy efficiency and seismic safety requirements. Low to mid-rise stone and brick masonry buildings constitute the typical masonry traditional buildings widespread in historical areas of Europe, with very limited construction of reinforced concrete (RC) structures before 1945. Most of RC buildings were constructed after the 1960s. Between 1945-1960 there is a transitional period for constructions moving from the traditional masonry to the new RC until the overwhelming prevail of the latter after 60s. During this period brick masonry and RC buildings is assumed to be evenly proportioned.

Representative masonry building typologies need to be defined to assess the impact of combined seismic and energy retrofitting for the European building stock. In the literature, the classification of structures is typically different for describing the building stock based on either its energy or seismic performance. Generally, the key parameters for both energy and seismic performance of buildings are: (i) the construction period, (ii) the main structural system or material (e.g. RC, masonry, steel, wood etc.) and, (iii) the geometric dimensions (e.g. number of storeys). Here, as the focus is only masonry buildings, the building stock is classified into low and medium-rise according to their number of storeys, grouped typically into 1-2 and 2-4. High-rise buildings with more than 5-6 storeys have a very small proportion and in this analysis are neglected. In terms of energy performance, the U-values of envelope elements varies with the material. Regarding the material of masonry structures, typically a distinction between stone-masonry and brick-masonry is made, which can classify the buildings into different age groups necessary to gather information from building inventories. Fired bricks are known since the antiquity; however, its mass production has been initiated during the industrialisation era. In this regard, the majority of the existing brick-masonry buildings were erected after the beginning of the 20th century. In this regard the year 1900 is assumed as the margin between the two age groups, assuming that the existing stone-masonry buildings were built before this time. In reality, however, there can be found mixed types of masonry buildings (e.g. stone-masonry ground floor and upper storeys from brick-masonry) and exceptions from the age assumption should be expected.

Data on the building stock for each case study location is obtained by two main sources. On the one hand the number of dwellings or average useful floor space constructed by decade is obtained from the respective Census data of 2011. Cities with historical centres have a large proportion between 20-30% of masonry structures (e.g. Perugia, Potenza, but also Groningen and Geneva), classified as stone- and low and mid-rise brick masonry buildings (Figure 32).



Figure 32. Relative proportion of masonry and RC building per location.



On the other hand NERA project provides data on building height which allowed for a discretization of buildings into low to mid-rise masonry buildings. As shown in Table 11, for the masonry building categories, low-rise and mid-rise buildings made of stone or clay brick masonry are defined.

The floor area of 8 x 18 m is chosen to be globally representative, as the selected buildings are theoretical in nature and their geometrical characteristics represent broadly the average of the building stock, similar to other large-scale studies on the building stock. Typical traditional masonry buildings do not have a constant storey-height and respectively the size of openings decreases along their height. Lower storeys tend to have a higher inter-storey height than typical RC structures. An average height of 4 m for the ground floor is assumed here and window dimensions equal to 1.0 x 1.90 m, resulting in glazing 18.3% for low-rise and mid-rise masonry buildings.

Table 11. Parameters of the case study masonry buildings.

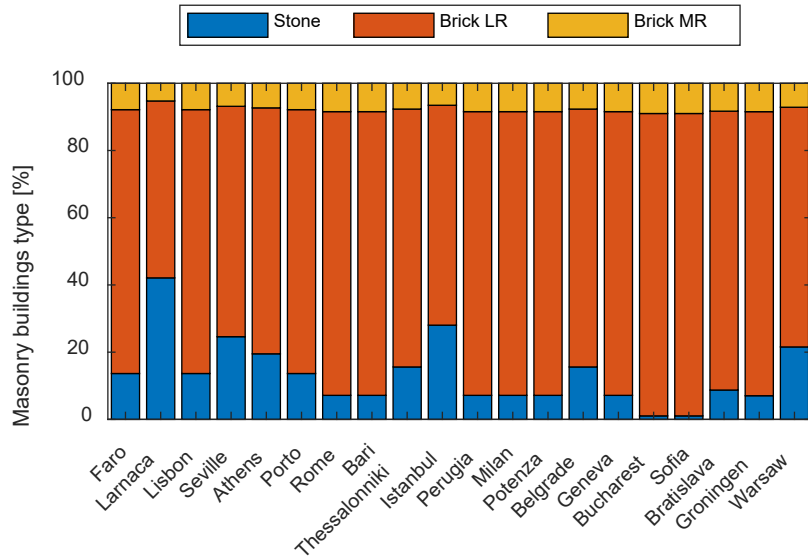
Elevation		Low-Rise stone or brick	Mid-Rise brick
Sketch			
Plan	m ²	8 x 18	8 x 18
Tot. floor area	m ²	288	576
No. of storeys		2	4
Storey height	m	4 (first) / 3.30	4 (first) / 3.10
Total height	m	9.60	15.90

Source: (Pohoryles et al., 2020)

The relative proportion of the masonry building types in terms of their building height or material (stone or brick masonry) aggregated from the NERA project is shown in Figure 33. Among the building envelope components, the walls and windows typically represent the major share of the overall energy loss, so this study focuses on these elements. Considering the extensive variations over the years and from country to

country, five different typical external wall types were selected representing the different time periods, as illustrated in Table 13.

Figure 33. Relative proportion of masonry building types per location.



The characteristics of the external walls of masonry buildings have been based on seismic vulnerability and energy studies of existing masonry buildings. While typically the thickness of the walls in masonry buildings varies along their height especially for mid-rise structures, here, average values have been considered, actually 30 cm for solid brick walls and 45 cm for stone walls. Stone walls are generally multi-leaf and an assumption of 60% stone and 40% mortar is made. The U-values in Table 12 are compared to the range of U-values of external wall elements in EU residential buildings based on the data collected in for the respective time periods.

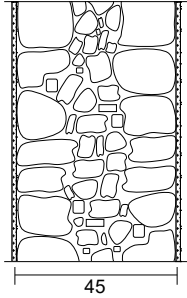
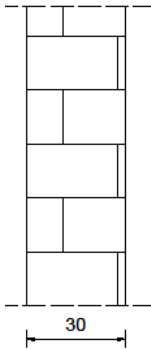
A key parameter of the thermal performance of buildings is the thermal transmittance of its envelope elements (U-value in W/m²/K). In Table 12, the U'-values, i.e. the U-value considering any thermal bridges, are shown for the selected envelope types. These were calculated using Eq. (24) after evaluating the effect of different thermal bridges in HEAT2, a two-dimensional heat transfer simulation software following ISO 10211 and ISO 10077-2 standards:

$$U' = U + \frac{\sum \psi \cdot l}{A} \text{ [W/(m}^2\text{K)]} \quad (24)$$

where U is the thermal transmittance of the building envelope element (exterior walls), A the area of the building envelope element (in m²) and $\sum \psi \cdot l$ the sum of all products of thermal bridge ψ -values (thermal transmittance of the linear thermal bridge in W/(mK)) and the lengths of thermal bridges. The ψ -values corresponding to the internal dimensions of the thermal bridge cross-section were considered. For masonry buildings, the majority of linear thermal bridges are generated by the geometry of the buildings, such as external masonry walls intersections (corners), internal masonry wall intersections with external masonry wall, while only a few are generated by combining different thermal conductive materials such as wooden floor intersection with external masonry wall and wooden window frame and masonry wall connection.

It can be observed that higher ψ -values are generated by wall-roof and wall-floor intersection and in the upper part of the windows, but generally the highest impact in the recalculation of the walls U-value is generated by the wall - floor intersection due to the length of this thermal bridge type, especially in the case of mid and high-rise buildings.

Table 12. Wall characteristics of the masonry buildings.

Period	Material	Type	Section	U (W/m ² K)	EU-range
1900-1960	Brick masonry	Single-leaf		1.30 - 2.24	0.9 - 2.5
Pre-1945	Stone masonry	Multi-leaf		2.15	0.9 - 2.4

5.2 Energy performance

Normally, an energy renovation project would encompass a variety of interventions including changes in HVAC system, adding renewable energy sources or shading devices; however, here the renovation targets are set in terms of the U-value of the envelope elements in order to reduce transmission heat losses. National energy performance legislations typically recommend U-values for different envelope elements (exterior walls, windows, roofs) to be achieved by newly built or renovated structures. The values for all case study locations are shown in Table 13 and are used to define U-value targets for the retrofit solution. In countries where U-value requirements for retrofitting of existing buildings are not available, the requirements for new built structures were taken, as illustrated in the last column of Table 13. Average U-values target values were considered in each climatic zone of the twenty climate zones selected. In a very recent study (Veljkovic et al., 2023), a hybrid tool combining artificial neural networks and building physics approach was developed to calculate the space heating energy demand was calculated for the whole EU residential sector.

The windows were also upgraded by means of airtight frames and glass with low solar heat gain coefficient (SHGC) of 0.55. Replacing the existing windows has substantial effects on decreasing the infiltration heat losses by increasing the overall airtightness of the building. Therefore, the number of air changes was decreased from 1.0 to 0.60 h⁻¹ corresponding to moderate shielded buildings with medium airtightness. The energy demand for space heating (HED) and cooling (CED) per conditioned floor area (kWh/m²) across the different locations of the case-study buildings was estimated by means of dynamic energy simulations in EnergyPlus (US Department of Energy, 2010). Details of the simulations can be found in (Pohoryles et al., 2020). It is noted that, system losses, auxiliary energy, hot water, and lighting energy use are conservatively assumed not to change between the existing and retrofitted states. The primary energy use and associated equivalent-CO₂ emissions are calculated from heating and cooling demands. The heating and cooling demands are multiplied by the respective total primary energy factors (f_{Ptot}) and converted in equivalent operational CO₂ emissions (k_{CO_2e} in g/kWh). These are obtained by multiplying the primary energy factors and equivalent operational CO₂ emission factors of different energy sources with the relative proportions of different energy sources used for heating and cooling based on the energy mix of the relevant countries from the 2015 residential profiles (ISO, 2017). The energy costs were transformed into *estimated annual losses* (EAL_e) using the next equation:

Table 13. Target U-values in each case-study location.

Zone	City	U-values [W/m ² K]								New existing*	build /
		Walls		Roof		Floor on ground		Windows			
1	Larnaca	0.85	0.75	0.75	0.61	0.75	0.68	3.80	3.10	N+R	
	Lisbon	0.80		0.70		0.70		2.80		N	
	Athens	0.50		0.45		0.45		3.00		N	
	Seville	0.82		0.45		0.82		3.10		N+R	
	Faro	0.80		0.70		0.70		2.80		N	
2	Bari	0.40	0.50	0.38	0.42	0.42	0.46	2.60	2.52	N	
	Porto	0.70		0.60		0.50		2.40		N	
	Rome	0.36		0.32		0.36		2.40		N	
	Saloniki	0.45		0.40		0.40		2.80		N	
	Istanbul	0.60		0.40		0.60		2.40		N+R	
3	Perugia	0.34	0.40	0.30	0.33	0.33	0.39	2.20	2.07	N	
	Milan	0.34		0.30		0.33		2.20		N	
	Potenza	0.36		0.32		0.36		2.40		N	
	Belgrade	0.40		0.40		0.40		1.50		N+R	
	Geneva	N/A		N/A		N/A		N/A		-	
4	Bucharest	0.56	0.35	0.20	0.22	0.22	0.30	1.30	1.40	N	
	Groningen	0.20		0.20		0.29		1.65		N+R	
	Sofia	0.35		0.28		0.40		1.70		N	
	Bratislava	0.32		0.20		0.40		1.40		N	
	Warsaw	0.23		0.20		0.25		1.10		N+R	

*N- requirements for new buildings

N+R – same requirements for both new and retrofitted buildings

Source: (Pohoryles et al., 2020)

$$EAL_E = \frac{\text{annual heating+cooling cost}}{\text{total building value}} [\%] \quad (25).$$

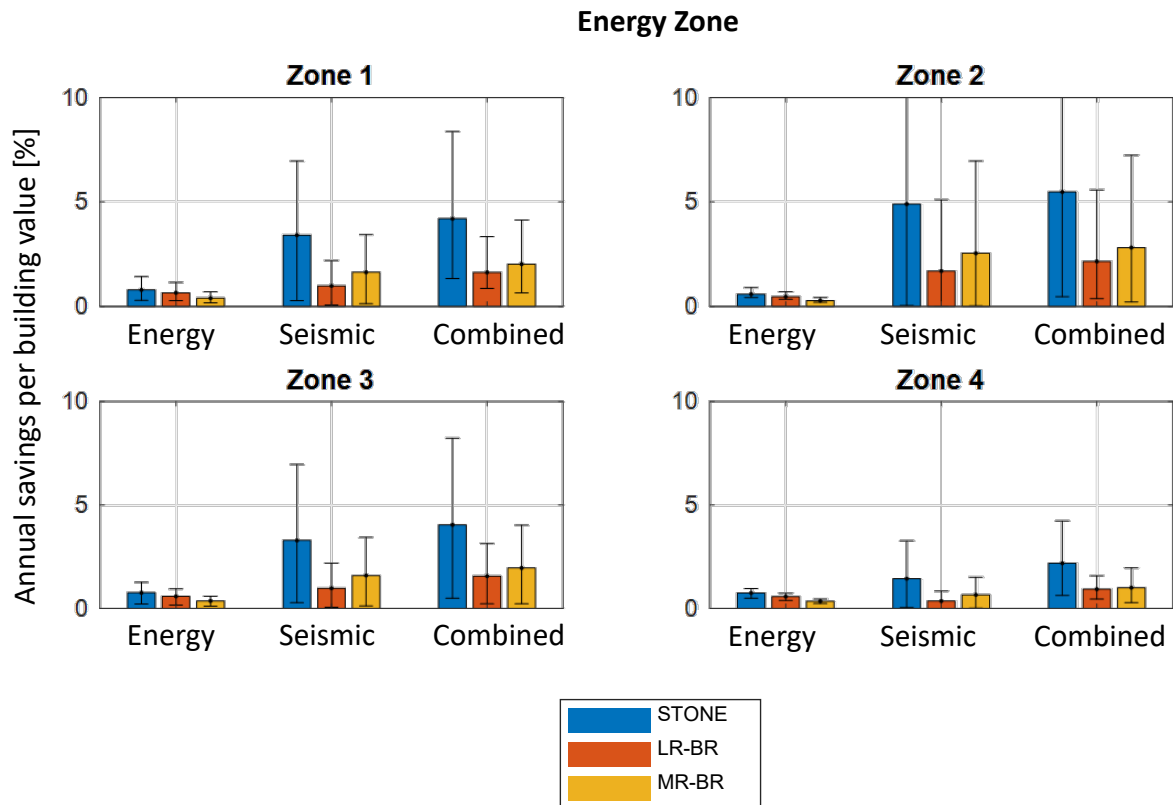
The EAL_E is obtained by dividing the heating and cooling energy costs per m^2 of each building type by the current average building prices per m^2 at each location. The energy costs are calculated based on the annual heating and cooling energy consumptions multiplied by the energy prices in the selected case study locations from (Eurostat, 2020a, 2020b). The current building prices per m^2 are evaluated from (NUMBEO, 2019). The annual energy savings due to retrofitting are then expressed as the difference in EAL_E before and after retrofitting, again as a percentage of the total building value. Note that the building value would potentially increase because of retrofitting. As this is difficult to precisely quantify, it is conservatively ignored from the analysis. The EAL_E 's are averaged over the considered energy zones and presented in Figure 34. As expected the savings are higher for the colder zones.

The savings due to the energy retrofit are given as the difference of the initial annual losses ($EAL_{j,i}$ and $j = E$) and the losses after retrofit application ($EAL_{j,r}$ and $j = E$) as in Eq. 27:

$$\Delta EAL_j = EAL_{j,i} - EAL_{j,r} [\%] \quad (27)$$

where j stands for type of retrofit (E for energy retrofit, S for seismic and C for a combined one). The ΔEAL_E 's are averaged over the considered cities and presented in Figure 34 per energy zone. It is seen that the energy savings do not vary remarkably as different targets have been set for the U values of each zone (Table 13).

Figure 34. Expected annual savings (%) after retrofitting per energy zone: (i) energy, (ii) seismic, and (iii) combined.



5.3 Seismic performance

Strengthening structures using TRM has been shown to improve their seismic performance considerably in various experimental studies on masonry walls or masonry-infilled RC frames, e.g. summarised by the authors in (Kouris and Triantafillou, 2018; Koutas et al., 2019; Pohoryles and Bournas, 2020). Despite this clear evidence the retrofitted buildings were not assumed to achieve the behaviour of modern high-code reinforced masonry buildings (RMB), but instead a conservative improvement in performance of a lower category in terms of seismic design level is assumed after receiving seismic retrofitting (Table 14). Therefore, URM buildings achieve a performance after the TRM-retrofitting which is assumed to be that of low- (for stone walls) or medium-code (for brick walls) RBM buildings.

Table 14. Target seismic design level of the seismic retrofit scheme.

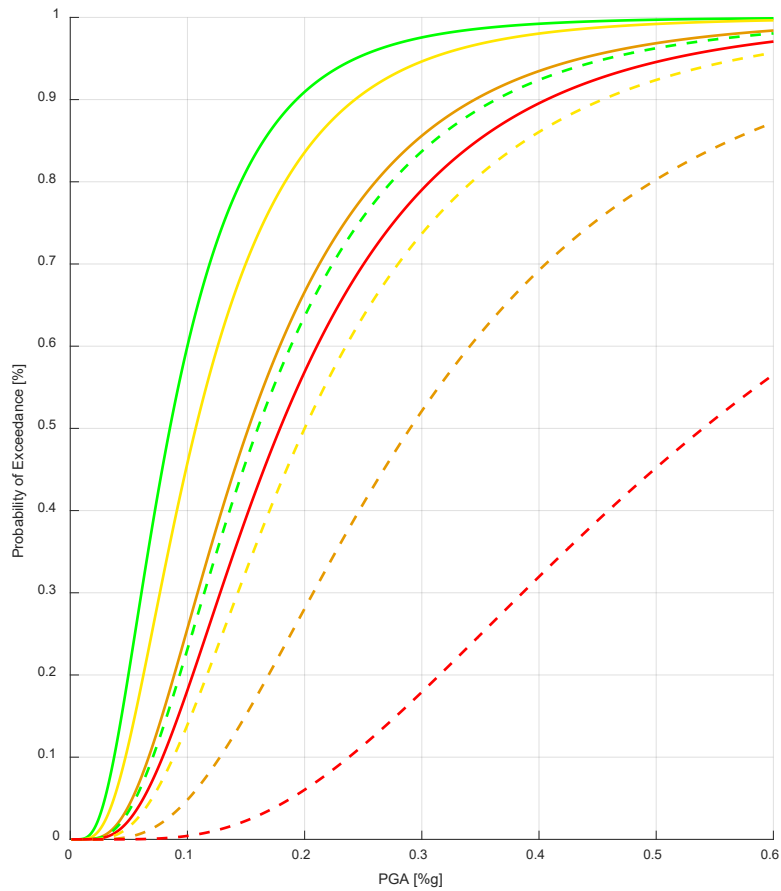
Material	Current design level	Target design level
Stone	URM (stone)	RBM (low)
Brick	URM (brick)	RBM (medium)

The *expected annual loss* due to seismic events (EAL_s) was evaluated applying the performance based methodology (Ellingwood et al., 2007; Kappos et al., 2007; Kouris and Kappos, 2015). Rather than using a deterministic approach with specific mechanical characteristics of the building materials, the next steps are followed to consider the typical spread of material characteristics for the different construction periods:

- First, fragility functions are used to determine the probability of reaching a certain level of damage (or damage state DS) for a certain level of earthquake intensity, presented in terms of PGA to be compatible with the intensity of seismic hazard at each location (Table 10).
- The defined damage levels are associated to a monetary loss as a fraction of the existing building value, by means of a damage-to-loss function specific for masonry and RC structures.
- The fragility curves and damage-to-loss functions are then combined to give the vulnerability curve of the specific building type, i.e. the monetary loss (as a percentage of the building value) vs. the selected intensity measure (PGA).
- The annual probability of exceedance (PE) in PGA values is defined based on the seismic hazard at each location.
- The annual probability of exceedance of loss (in % of building value) is the combination of the annual probability of exceedance of a certain PGA with the intensity to loss curve.
- The *expected annual seismic loss* (EAL_s) is finally the integral of the latter function.

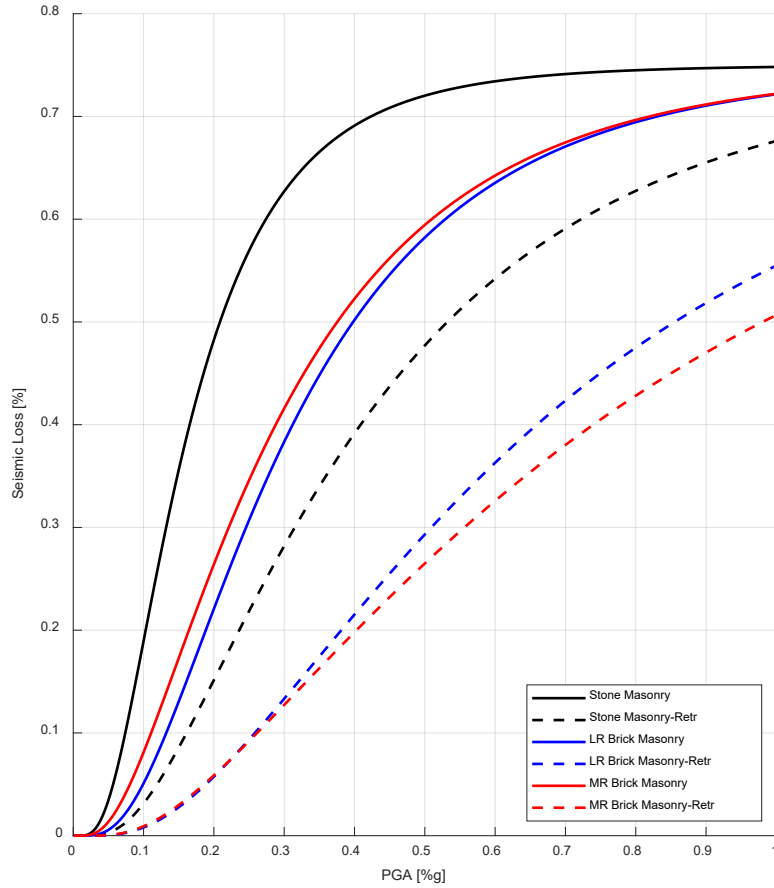
Typical fragility functions for the european building stock with four DS (ranging from 'no damage' to 'collapse') for the chosen stone (Ahmad et al., 2011) and brick (FEMA, 2003) unreinforced masonry were selected according to their age, number of storeys (low and mid-rise) and building material (stone, brick). The proposed fragility curves of the RBM buildings from HAZUS (FEMA, 2003) were adopted to represent the target performance. The fragility curves for the four damage states of stone masonry low rise before and after retrofitting based on the aforementioned assumptions are illustrated in Figure 35.

Figure 35. Fragility curves for four damage states of stone URM and RMB (dashed lines) buildings.



The damage-to-loss functions were selected from the literature (Kappos et al., 2006). Note that this loss is based on the cost of repair for the specific damage states and is always less than or equal to the replacement cost, i.e. the value of the building. Other losses that can be associated to earthquakes, such as human losses and the social impact are however not considered, as the scope of this study focuses only on buildings and the assumption of repair costs alone renders more conservative results. The vulnerability curves of the buildings types (unreinforced and strengthened) according to the previous assumptions are shown in Figure 36 where a ceiling value equal to 0.75 has been assumed for the losses.

Figure 36. Vulnerability curves for stone and low/medium rise brick masonry buildings and their strengthened counterparts.

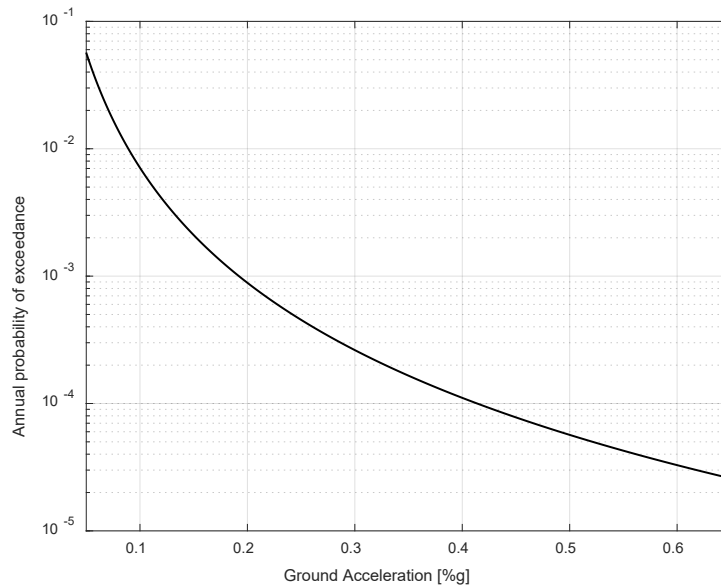


The annual rate of exceedance H of a reference PGA can be assumed to vary according to (CEN, 1998):

$$H(a_{gR}) \cong k_0 \cdot a_{gR}^{-k} \quad (26)$$

where the proposed value for k is 3 and k_0 can be computed based on the a_{gR} that corresponds to a probability of exceedance of 10% in 50 years, i.e. the values of PGAs in Table 10. For example the annual probability of exceedance for Milan, Italy of the PGA = 0.15g (10% probability of exceedance in 50 years) is 0.002 approximately which is equal to 1/475 i.e. the inverse of the return period (Figure 37). The savings are higher for the zone with higher hazard. The EAL_S 's are averaged over the considered energy zones and presented in Figure 34. Seismic savings for colder climatic zones are lower due to a lower seismic hazard ().

Figure 37. Annual probability of exceedance vs. ground acceleration for Milan.



The EAL_s 's are averaged over the considered energy zones and presented in Figure 34.

5.4 Combined performance

The combined losses are defined as the sum of the energy and the seismic ones $EAL_c = EAL_E + EAL_s$ (Bournas, 2018). The impact of the renovation strategy in terms of cost benefits for each seismic zone is evaluated by comparing the savings in terms of energy costs and seismic losses with the initial investment costs by means of assessing the payback periods, calculated using Eq. 28.

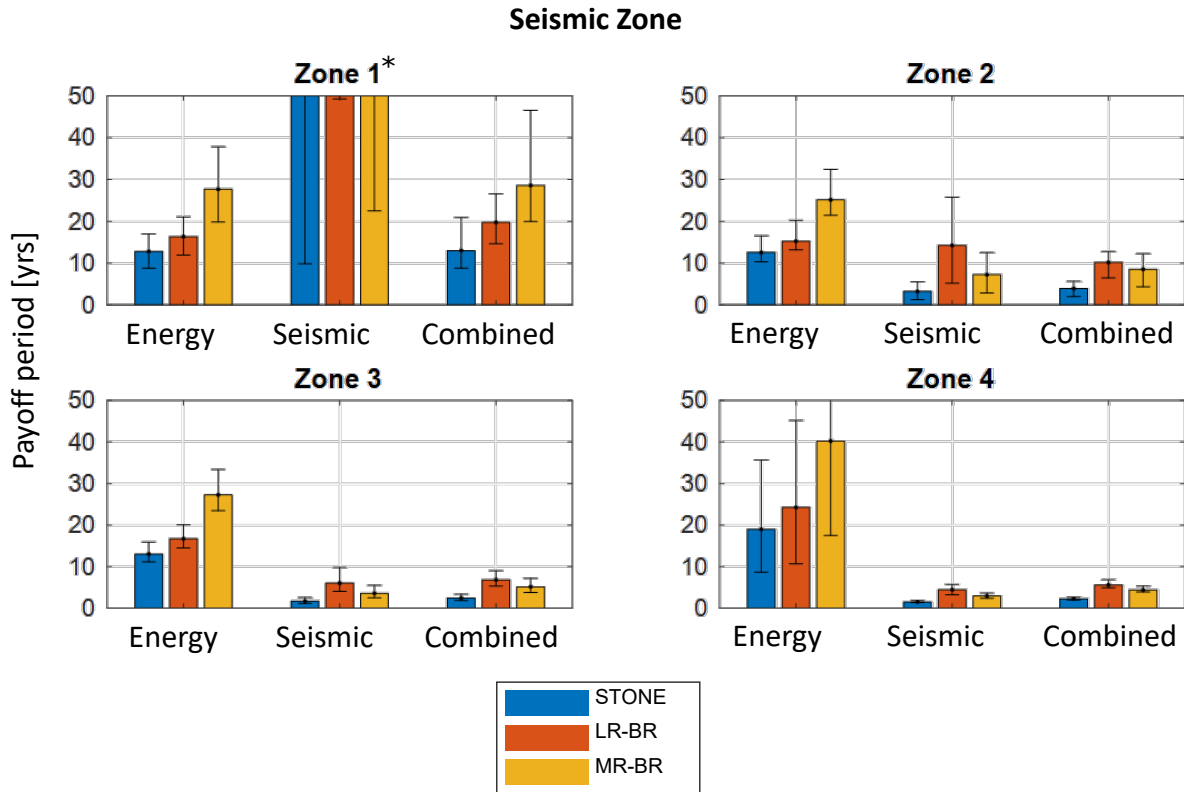
The indicative payback period of the retrofitting interventions can be calculated as the ratio of the assumed costs of the retrofit (with respect to the non-retrofitted building) to the annual cost savings:

$$t_{payback} = \frac{\text{Retrofit cost}_k / \text{building value}}{\Delta EAL_k} [\text{years}] \quad (28)$$

where k corresponds to the respective values of the energy, seismic or combined retrofit, depending on the evaluation. Details about the assumptions of the building values can be found in (Pohoryles et al., 2020). It is worth noting that the cost estimations do not precisely consider the spatial variation in the case study cities but reflect gross current mean trends. The payback periods are estimated for the energy, the seismic and the combined retrofitting and averaged over the seismic zone in Figure 38. The exact values of payback periods should be considered with caution, as average gross cost estimations have been made and may considerably change depending on the global economy crisis and other financial conditions.

As mentioned initially, the effect of combined seismic and energy retrofitting is evaluated in this study and seismic risk mitigation should be considered according to the new Energy Performance of Buildings Directive (EU Council and EU Parliament, 2010). The plots in Figure 38 allow to assess whether a combined retrofit is worthwhile compared to an energy retrofit alone for each building type and seismic zone. The payback periods of separate seismic and energy interventions are also indicated. The results shown herein indicate important trends regarding the benefits of combined retrofit interventions. Obviously, for vulnerable buildings in high seismicity locations the payoff period for the seismic retrofitting shortens considerably. The combined retrofit achieves a shorter payback period, less than 10 years, for the cities with higher seismicity and extends to the same level with the energy retrofit for low seismicity zones. It is interesting to note that a combined retrofit is beneficial for masonry buildings already from zone 2, that is in cities with low to medium seismic hazard ($0.10g < PGA \leq 0.25g$).

Figure 38. Payback periods in years per seismic zone: (i) energy, (ii) seismic, and (iii) combined.

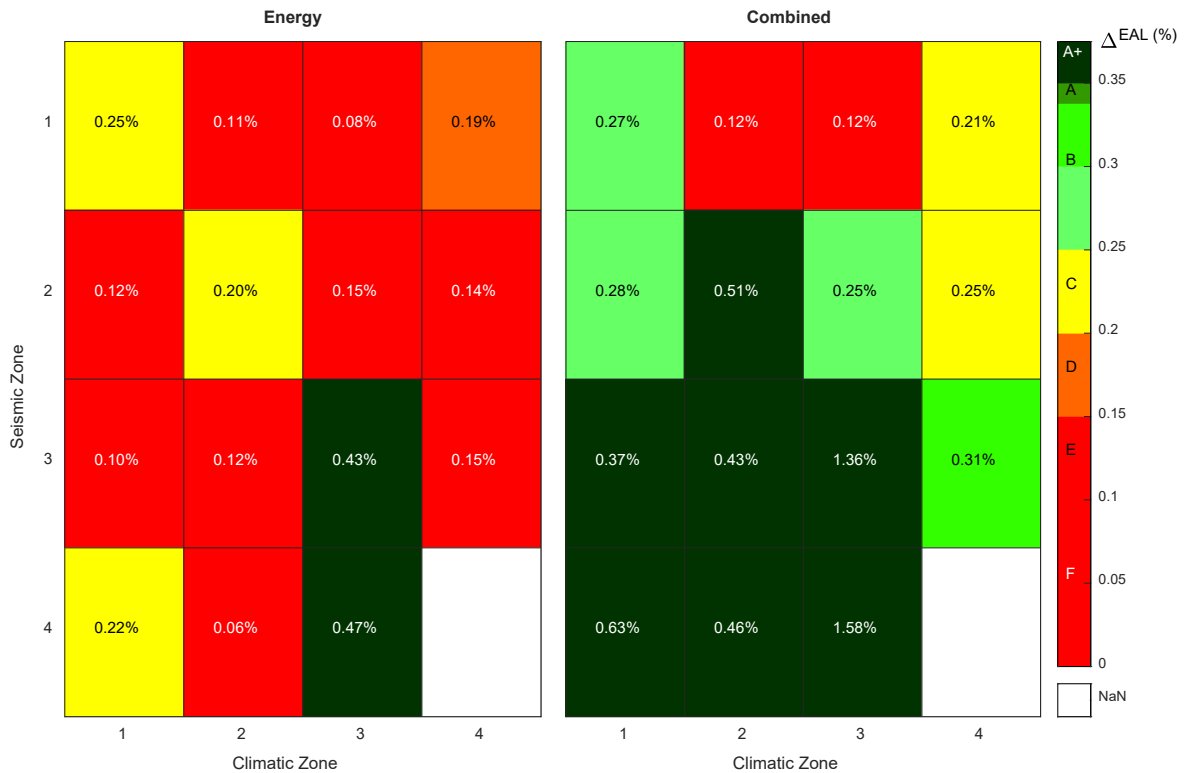


* The payoff periods for stone, low-rise and mid-rise masonry buildings in zone 1 are 73, 176 and 166 years respectively.

Therefore, for locations of low seismicity (seismic zones 1 and 2), the benefit of adding seismic retrofitting is generally limited (only for stone-masonry buildings noticeable) and the payback periods are rather similar for energy retrofitting alone and the combined retrofitting scenario for all masonry structures. However, when assessing locations in zones of medium to high seismicity (seismic zones 3 to 4), the benefits of providing simultaneously the seismic and energy retrofitting are illustrated, as in these zones the importance of seismic loss reduction becomes more critical than the energy savings alone. The benefits are particularly important for stone-masonry buildings, as losses due to energy costs and due to seismic events can be significantly reduced. Even for seismic zone 2, with low seismic hazard, the combined retrofit payback period is reduced for the oldest masonry buildings. It should be highlighted that for zones in which seismic retrofit is essential (i.e. above seismic zone 2), implementing the seismic intervention at separate times from the energy retrofit, would lead to longer payback periods.

The benefits of a simultaneous seismic and energy retrofitting of the building stocks in all case study locations are compared to a mere energy retrofitting in their 2030 state assuming a renovation rate 3% per year only for masonry structures. By this year and with this rate all masonry buildings will have been renovated in the considered cities. In this study the total building population is considered for the estimation of losses and the reader is referred to (Pohoryles et al., 2020) regarding the current RC building stock which is assumed not to be involved in the retrofitting process. The classification from A+ to F is done in terms of expected savings ΔEAL (in % of the building value) by 2030 in respect to the 2011 state and allows an insight onto the effect of different retrofitting scenarios in various seismic risk and climatic conditions. Values of ΔEAL_C above 0.35% correspond to a category A+, while a value below 0.075% of expected savings corresponds to an F rating with intermediate categories A, B, C, D and E (Calvi et al., 2016) (Figure 39).

Figure 39. Average classification in terms of ΔEAL of the building stock across all seismic and climatic zones by 2030 assuming a renovation rate of masonry buildings 3% for a merely energy or a combined retrofitting.



As shown in Figure 39, the increase in seismic risk (going from seismic zone 1 to 4) within the same climatic zone, leads to an increase of the ΔEAL due to the corresponding increase in the seismic ΔEAL_s . In spite of the relatively small percentage of masonry buildings in the cities (Figure 32) the benefit from a combined retrofit of masonry buildings can be remarkable as can be noticed from the change of savings category for several combinations of seismic and climatic zones in respect to the energy retrofit. Carrying out a simultaneous upgrading of masonry buildings, cities with moderate to high seismicity (seismic zones 3 and 4) achieve an A+ or A category of savings.

Box 7. Implementation of a simultaneous seismic + energy retrofitting of buildings in Europe

The investigation of the implementation of a simultaneous seismic and energy retrofitting of buildings in cities across Europe yielded the EAL's and payback periods. The trend that this investigation reveals, is that cities with old masonry buildings in high seismicity areas will be substantially benefitted from a simultaneous retrofitting rather than a merely energy retrofitting. The payback period of such a refurbishment investment for URM buildings will be remarkably shorter.

6 Conclusions

The emerging need to upgrade and protect traditional masonry buildings both in terms of structural and thermal retrofit, required also by current EU and/or national legislation, is addressed in this report by exploring the potential of integrating seismic and energy retrofitting for masonry buildings. More specifically seismic retrofitting in the form of TRM jacketing is simultaneously with thermal insulation materials. To allow for a wider investigation of such an integrated system, analytical models were developed and showed that the hybrid system can highly benefit cities with high seismicity.

Initially, a homogenisation model, in the form of a set of closed-form expressions, was proposed to estimate the in-plane elastic and shear moduli and the Poisson's ratios in two orthogonal directions. Gradient homogenisation model (GREHM) was developed introducing an internal non-local length to account for the micro-structure of multiphase masonry and the respective local phenomena that take place in reality in the identified RSEs for the horizontal and the vertical directions (i.e. parallel and perpendicular to the bed joints). The gradient elasticity was opted for it can address phenomena such as discontinuities and cracks appearing in masonry in local scale. The internal length was found a significant parameter that can affect the accuracy of the model when compared with experimental results. A value for the internal length is proposed to be used where there are no other data calibrated on the available experimental data.

Moreover, an implicit model for simulating the out-of-plane behaviour of TRM-strengthened walls has been presented, which by including an empirical rule for the debonding of the textile reinforcement avoids complex further simulations in micro and macro scale. Using this simplified modelling methodology, a parametric analysis was carried out where a variation of textiles has been used. Textiles with low strength capacity (e.g. natural fibres) to rather strong ones (e.g. composite fibres) with varied number of layers and yarn dimensions were applied to investigate their potential in reinforcing masonry for out-of-plane loads. The analysis shows that TRM jackets can effectively enhance the out-of-plane capacity of walls. Even when natural fibres are used (e.g. low capacity fibres) a substantial out-of-plane capacity is recorded which becomes much higher increasing the fibres strength. The axial load increases substantially the out-of-plane capacity of the walls when the prevailing failure mode is the textile damage.

Furthermore, a model for masonry strengthened walls with TRM has been developed in an explicit FE code. The material models of the simulation have been calibrated using static out-of-plane experiments. Unreinforced and retrofitted masonry piers using one layer of carbon textile in inorganic cement-based matrix (TRM) have been exposed to blast loads. Application of one layer of TRM (using carbon textile in inorganic matrix) can substantially increase the capacity against impact and blast loads.

The current low renovation rates of buildings make it challenging to meet the ambitious EU climate and energy targets at 2030 and 2050. The effect of a combined retrofit of the European building stock allow for an implementation of an increased renovation rate which was shown not only to meet the emission reduction targets, but also to be economically feasible, as reduced losses from energy costs and seismic damage make the renovation strategies more viable. Looking at payback periods for the combined energy and seismic retrofit investment of old traditional stone-masonry buildings, integrated interventions showed financial benefits over energy retrofitting alone for high seismicity areas. The growing emphasis on cross-sectoral approaches shows their potential to provide comprehensive solutions to complex challenges. As integrated approaches evolve, further research is needed to ensure renovation strategies increase seismic resilience, improve indoor environments, enhance energy efficiency, and minimize life-cycle impacts. Developing and using low-carbon technologies will be crucial for achieving decarbonized buildings and advancing climate neutrality by 2050.

References

- Ahmad, N., Crowley, H., Pinho, R., 2011. Analytical Fragility Functions for Reinforced Concrete and Masonry Buildings and Buildings Aggregates of Euro-Mediterranean Regions –UPAV methodology.
- Aifantis, E.C., 2003. Update on a class of gradient theories, *Mechanics of Materials*. Elsevier. [https://doi.org/10.1016/S0167-6636\(02\)00278-8](https://doi.org/10.1016/S0167-6636(02)00278-8)
- Aifantis, E.C., 1992. On the role of gradients in the localization of deformation and fracture. *Int. J. Eng. Sci.* 30, 1279–1299. [https://doi.org/10.1016/0020-7225\(92\)90141-3](https://doi.org/10.1016/0020-7225(92)90141-3)
- Akintayo, O.T., Papadopoulos, P.G., Aifantis, E.C., 2012. A note on gradient truss models. *Int. Rev. Mech. Eng.* 6, 691–697.
- Alecci, V., De Stefano, M., Luciano, R., Rovero, L., Stipo, G., 2016. Experimental Investigation on Bond Behavior of Cement-Matrix-Based Composites for Strengthening of Masonry Structures. *J. Compos. Constr.* 20, 04015041. [https://doi.org/10.1061/\(ASCE\)CC.1943-5614.0000598](https://doi.org/10.1061/(ASCE)CC.1943-5614.0000598)
- Anastaselos, D., Giama, E., Papadopoulos, A.M., 2009. An assessment tool for the energy, economic and environmental evaluation of thermal insulation solutions. *Energy Build.* 41. <https://doi.org/10.1016/j.enbuild.2009.06.003>
- Anthoine, A., 1995. Derivation of the in-plane elastic characteristics of masonry through homogenization theory. *Int. J. Solids Struct.* 32, 137–163. [https://doi.org/10.1016/0020-7683\(94\)00140-R](https://doi.org/10.1016/0020-7683(94)00140-R)
- Askes, H., Aifantis, E.C., 2011. Gradient elasticity in statics and dynamics: An overview of formulations, length scale identification procedures, finite element implementations and new results. *Int. J. Solids Struct.* 48, 1962–1990. <https://doi.org/10.1016/j.ijsolstr.2011.03.006>
- Askes, H., Morata, I., Aifantis, E.C., 2008. Finite element analysis with staggered gradient elasticity 86, 1266–1279. <https://doi.org/10.1016/j.compstruc.2007.11.002>
- Askouni, P.D., Papanicolaou, C. (Corina) G., 2019. Textile Reinforced Mortar-to-masonry bond: Experimental investigation of bond-critical parameters. *Constr. Build. Mater.* 207, 535–547. <https://doi.org/10.1016/j.conbuildmat.2019.02.102>
- Askouni, P.D., Papanicolaou, C.G., 2017. Experimental investigation of bond between glass textile reinforced mortar overlays and masonry: the effect of bond length. *Mater. Struct. Constr.* 50. <https://doi.org/10.1617/s11527-017-1033-7>
- Augenti, N., Parisi, F., Prota, A., Manfredi, G., 2011. In-Plane Lateral Response of a Full-Scale Masonry Subassemblage with and without an Inorganic Matrix-Grid Strengthening System. *J. Compos. Constr.* 15, 578–590. [https://doi.org/10.1061/\(ASCE\)CC.1943-5614.0000193](https://doi.org/10.1061/(ASCE)CC.1943-5614.0000193)
- Babaeidarabad, S., Caso, F. De, Nanni, A., 2014a. Out-of-Plane Behavior of URM Walls Strengthened with Fabric-Reinforced Cementitious Matrix Composite. *J. Compos. Constr.* 18, 04013057. [https://doi.org/10.1061/\(ASCE\)CC.1943-5614.0000457](https://doi.org/10.1061/(ASCE)CC.1943-5614.0000457)
- Babaeidarabad, S., De Caso, F., Nanni, A., 2014b. URM Walls Strengthened with Fabric-Reinforced Cementitious Matrix Composite Subjected to Diagonal Compression. *J. Compos. Constr.* 18, 04013045. [https://doi.org/10.1061/\(ASCE\)CC.1943-5614.0000441](https://doi.org/10.1061/(ASCE)CC.1943-5614.0000441)
- Baek, E., Pohoryles, D.A., Kallioras, S., Bournas, D.A., Choi, H., Kim, T., 2022. Innovative seismic and energy retrofitting of wall envelopes using prefabricated textile-reinforced concrete panels with an embedded capillary tube system. *Eng. Struct.* 265, 114453. <https://doi.org/10.1016/J.ENGSTRUCT.2022.114453>
- Baker, W.E. (Wilfred E., 1983. *Explosion hazards and evaluation*. Elsevier Scientific Pub. Co.
- Bakis, C.E., Bank, L.C., Brown, V.L., Cosenza, E., Davalos, J.F., Lesko, J.J., Machida, A., Rizkalla, S.H., Triantafyllou, T.C., 2002. Fiber-Reinforced Polymer Composites for Construction—State-of-the-Art Review. *J. Compos. Constr.* 6, 73–87. [https://doi.org/10.1061/\(ASCE\)1090-0268\(2002\)6:2\(73\)](https://doi.org/10.1061/(ASCE)1090-0268(2002)6:2(73))

- Banholzer, B., Brockmann, T., Brameshuber, W., 2006. Material and bonding characteristics for dimensioning and modelling of textile reinforced concrete (TRC) elements. *Mater. Struct.* 39, 749–763. <https://doi.org/10.1617/s11527-006-9140-x>
- Bellini, A., Mazzotti, C., 2017. A review on the bond behavior of FRP composites applied on masonry substrates. *RILEM Tech. Lett.* 2, 74–82. <https://doi.org/10.21809/rilemtechlett.2017.40>
- Belmouden, Y., Lestuzzi, P., 2009. An equivalent frame model for seismic analysis of masonry and reinforced concrete buildings. *Constr. Build. Mater.* 23, 40–53. <https://doi.org/DOI:10.1016/j.conbuildmat.2007.10.023>
- Benedetti, A., 2019. In Plane Behaviour of Masonry Walls Reinforced with Mortar Coatings and Fibre Meshes. *Int. J. Archit. Herit.* 13, 1029–1041. <https://doi.org/10.1080/15583058.2019.1618972>
- Bertolesi, E., Carozzi, F.G., Milani, G., Poggi, C., 2014. Numerical modeling of Fabric Reinforce Cementitious Matrix composites (FRCM) in tension. *Constr. Build. Mater.* 70, 531–548. <https://doi.org/10.1016/j.conbuildmat.2014.08.006>
- Bilotta, A., Ceroni, F., Lignola, G.P., Prota, A., 2017. Use of DIC technique for investigating the behaviour of FRCM materials for strengthening masonry elements. *Compos. Part B Eng.* 129, 251–270. <https://doi.org/10.1016/j.compositesb.2017.05.075>
- Boffill, Y., Blanco, H., Lombillo, I., Villegas, L., 2019. Assessment of historic brickwork under compression and comparison with available equations. *Constr. Build. Mater.* 207, 258–272. <https://doi.org/10.1016/J.CONBUILDMAT.2019.02.083>
- Bournas, D.A., 2018. Concurrent seismic and energy retrofitting of RC and masonry building envelopes using inorganic textile-based composites combined with insulation materials: A new concept. *Compos. Part B Eng.* 148, 166–179. <https://doi.org/10.1016/j.compositesb.2018.04.002>
- Brameshuber, W., 2016. Manufacturing methods for textile-reinforced concrete, in: *Textile Fibre Composites in Civil Engineering*. Elsevier, pp. 45–59. <https://doi.org/10.1016/B978-1-78242-446-8.00004-5>
- Brencich, A., Corradi, C., Gambarotta, L., 2008. Eccentrically loaded brickwork: Theoretical and experimental results. *Eng. Struct.* 30, 3629–3643. <https://doi.org/10.1016/j.engstruct.2008.05.010>
- Calvi, G.M., Sousa, L., Ruggeri, C., 2016. Energy efficiency and seismic resilience: A common approach, in: *Multi-Hazard Approaches to Civil Infrastructure Engineering*. Springer International Publishing, pp. 165–208. https://doi.org/10.1007/978-3-319-29713-2_9
- Carozzi, F.G., Bellini, A., D’Antino, T., de Felice, G., Focacci, F., Hojdys, Ł., Laghi, L., Lanoye, E., Micelli, F., Panizza, M., Poggi, C., 2017. Experimental investigation of tensile and bond properties of Carbon-FRCM composites for strengthening masonry elements. *Compos. Part B Eng.* 128, 100–119. <https://doi.org/10.1016/j.compositesb.2017.06.018>
- Castellazzi, L., Paci, D., Zangheri, P., Maduta, C., Economidou, M., Riveiro Serrenho, T., Zancanella, P., Ringel, M., Valentova, M., Tsemekidi Tzeiranaki, S., 2022. Assessment of first long-term renovation strategies under the Energy Performance of Building Directive (Art. 2a), EUR 31309 EN, Publications Office of the European Union, Luxembourg, 2022, ISBN 978-92-76-58990-7, doi:10.2760/535845, JRC128067.
- CEB-FIB, 2011. Model Code 2010 - First complete draft - Volume 1, First complete draft - Volume 1. <https://doi.org/10.1002/9783433604090.ch6>
- CEN, 1998. Eurocode 8, design of structures for earthquake resistance. Part 1: general rules, seismic actions and rules for buildings. *Eur. Stand. NF EN 1*.
- Cevallos, O.A., Olivito, R.S., Codispoti, R., Ombres, L., 2015. Flax and polyparaphenylene benzobisoxazole cementitious composites for the strengthening of masonry elements subjected to eccentric loading. *Compos. Part B Eng.* 71, 82–95. <https://doi.org/10.1016/j.compositesb.2014.10.055>

- Chen, S.-Y., Moon, F.L., Yi, T., 2008. A macroelement for the nonlinear analysis of in-plane unreinforced masonry piers. *Eng. Struct.* 30, 2242–2252. <https://doi.org/10.1016/j.engstruct.2007.12.001>
- D’Antino, T., Carloni, C., Sneed, L.H., Pellegrino, C., 2014. Matrix-fiber bond behavior in PBO FRM composites: A fracture mechanics approach. *Eng. Fract. Mech.* 117, 94–111. <https://doi.org/10.1016/j.engfracmech.2014.01.011>
- De Santis, S., Carozzi, F.G., de Felice, G., Poggi, C., 2017. Test methods for Textile Reinforced Mortar systems. *Compos. Part B Eng.* 127, 121–132. <https://doi.org/10.1016/j.compositesb.2017.03.016>
- De Santis, S., Casadei, P., De Canio, G., de Felice, G., Malena, M., Mongelli, M., Roselli, I., 2016. Seismic performance of masonry walls retrofitted with steel reinforced grout. *Earthq. Eng. Struct. Dyn.* 45, 229–251. <https://doi.org/10.1002/eqe.2625>
- Del Zoppo, M., Di Ludovico, M., Balsamo, A., Prota, A., 2019. In-plane shear capacity of tuff masonry walls with traditional and innovative Composite Reinforced Mortars (CRM). *Constr. Build. Mater.* 210, 289–300. <https://doi.org/10.1016/j.conbuildmat.2019.03.133>
- Di Nino, S., Luongo, A., 2019. A simple homogenized orthotropic model for in-plane analysis of regular masonry walls. *Int. J. Solids Struct.* 167, 156–169. <https://doi.org/10.1016/j.IJSOLSTR.2019.03.013>
- Donnini, J., Corinaldesi, V., Nanni, A., 2016. Mechanical properties of FRM using carbon fabrics with different coating treatments. *Compos. Part B Eng.* 88, 220–228. <https://doi.org/10.1016/j.compositesb.2015.11.012>
- Dost, B., Ruigrok, E., Spetzler, J., 2017. Development of seismicity and probabilistic hazard assessment for the Groningen gas field. *Geol. En Mijnbouw/Netherlands J. Geosci.* 96. <https://doi.org/10.1017/njg.2017.20>
- Drougkas, A., Roca, P., Molins, C., 2016. Compressive strength and elasticity of pure lime mortar masonry. *Mater. Struct.* 49, 983–999. <https://doi.org/10.1617/s11527-015-0553-2>
- Düreth, C., Weck, D., Böhm, R., Thieme, M., Gude, M., Henkel, S., Wolf, C.H., Biermann, H., 2020. Determining the Damage and Failure Behaviour of Textile Reinforced Composites under Combined In-Plane and Out-of-Plane Loading. *Materials* 13, 4772. <https://doi.org/10.3390/ma13214772>
- Economidou, M., Todeschi, V., Bertoldi, P., D’Agostino, D., Zangheri, P., Castellazzi, L., 2020. Review of 50 years of EU energy efficiency policies for buildings. *Energy Build.* 225, 110322. <https://doi.org/10.1016/j.enbuild.2020.110322>
- Ellingwood, B.R., Celik, O.C., Kinali, K., 2007. Fragility assessment of building structural systems in Mid-America. *Earthq. Eng. Struct. Dyn.* 36, 1935–1952. <https://doi.org/10.1002/eqe.693>
- EU Council, EU Parliament, 2010. DIRECTIVE 2010/31/EU on the energy performance of buildings.
- European Commission, 2024. Energy performance of buildings (recast). European Parliament legislative resolution of 12 March 2024 on the proposal for a directive of the European Parliament and of the Council on the energy performance of buildings (recast). Texts adopted.
- European Commission, 2023. Key facts on energy and EU buildings. *Energy Energy Perform. Build.* Dir. URL https://energy.ec.europa.eu/topics/energy-efficiency/energy-efficient-buildings/energy-performance-buildings-directive_en
- European Commission, 2020. Communication from the Commission to the European Parliament, the Council, the European Economic and Social Committee and the Committee of the regions: Renovation Wave for Europe - greening our buildings, creating jobs, improving lives (No. COM(2020) 662). Brussels.
- European Commission, 2019. Communication from the Commission to the European Parliament, the Council, the European Economic and Social Committee and the Committee of the Regions: The European Green Deal (No. COM(2019) 640). Brussels.

- European Commission, 2018. Directive (EU) 2018/844 of the European Parliament and of the Council of 30 May 2018 amending Directive 2010/31/EU on the energy performance of buildings and Directive 2012/27/EU on energy efficiency.
- European Parliament, 2021. Regulation (EU) 2021/1119 of the European Parliament and of the Council of 30 June 2021 establishing the framework for achieving climate neutrality and amending Regulations (EC) No 401/2009 and (EU) 2018/1999 (European Climate Law).
- EUROPLEXUS, 2019. Commissariat à l’Energie Atomique & European Commission - JRC [WWW Document]. User Man. URL <http://www-epx.cea.fr/>
- Eurostat, 2020a. Gas prices by type of user [WWW Document]. URL <https://ec.europa.eu/eurostat/web/products-datasets/-/ten00118> (accessed 11.15.20).
- Eurostat, 2020b. Electricity prices [WWW Document]. URL https://appsso.eurostat.ec.europa.eu/nui/show.do?dataset=nrg_pc_204&lang=en (accessed 11.15.20).
- Filippidou, F., Jimenez Navaro, J.P., 2019. Achieving the cost-effective energy transformation of Europe’s buildings, EUR 29906 EN, Publications Office of the European Union, Luxembourg, 2019, ISBN 978-92-76-12394-1, doi:10.2760/278207, JRC117739.
- Formisano, A., Florio, G., Landolfo, R., Mazzolani, F.M., 2015. Numerical calibration of an easy method for seismic behaviour assessment on large scale of masonry building aggregates. *Civ.-Comp* 80, 116–138. <http://dx.doi.org/10.1016/j.advengsoft.2014.09.013>
- Furtmüller, T., Adam, C., 2011. Numerical modeling of the in-plane behavior of historical brick masonry walls. *Acta Mech.* 221, 65–77. <https://doi.org/10.1007/s00707-011-0493-z>
- Gattesco, N., Boem, I., 2017. Characterization tests of GFRM coating as a strengthening technique for masonry buildings. *Compos. Struct.* 165, 209–222. <https://doi.org/10.1016/j.compstruct.2017.01.043>
- Gkournelos, P.D., Azdejković, L.D., Triantafillou, T.C., 2022. Innovative and Eco-friendly Solutions for the Seismic Retrofitting of Natural Stone Masonry Walls with Textile Reinforced Mortar: In- and Out-of-Plane Behavior. *J. Compos. Constr.* 26, 04021061. [https://doi.org/10.1061/\(ASCE\)CC.1943-5614.0001173](https://doi.org/10.1061/(ASCE)CC.1943-5614.0001173)
- Gkournelos, P.D., Triantafillou, T.C., Bournas, D.A., 2020. Integrated Structural and Energy Retrofitting of Masonry Walls: Effect of In-Plane Damage on the Out-of-Plane Response. *J. Compos. Constr.* 24. [https://doi.org/10.1061/\(ASCE\)CC.1943-5614.0001066](https://doi.org/10.1061/(ASCE)CC.1943-5614.0001066)
- Gries, T., Raina, M., Quadflieg, T., Stolyarov, O., 2016. Manufacturing of textiles for civil engineering applications, *Textile Fibre Composites in Civil Engineering*. <https://doi.org/10.1016/B978-1-78242-446-8.00002-1>
- Guilbaud, D., 2015. Damage plastic model for concrete failure under impulsive loadings XIII International Conference on Computational Plasticity. Fundamentals and Applications, in: Oñate, E., Owen, D.R.J., Peric, D., Chiumenti, M. (Eds.), XIII International Conference on Computational Plasticity. Fundamentals and Applications COMPLAS XIII . Barcelona, Spain , pp. 1031–1042.
- Gumaste, K.S., Nanjunda Rao, K.S., Venkatarama Reddy, B. V., Jagadish, K.S., 2007. Strength and elasticity of brick masonry prisms and wallettes under compression. *Mater. Struct.* 40, 241–253. <https://doi.org/10.1617/s11527-006-9141-9>
- Habibi, M., Laperrière, L., Hassanabadi, H.M., 2019. Effect of moisture absorption and temperature on quasi-static and fatigue behavior of nonwoven flax epoxy composite. *Compos. Part B Eng.* 166, 31–40. <https://doi.org/10.1016/j.compositesb.2018.11.131>
- Harajli, M., ElKhatib, H., San-Jose, J.T., 2010. Static and Cyclic Out-of-Plane Response of Masonry Walls Strengthened Using Textile-Mortar System. *J. Mater. Civ. Eng.* 22, 1171–1180. [https://doi.org/10.1061/\(ASCE\)MT.1943-5533.0000128](https://doi.org/10.1061/(ASCE)MT.1943-5533.0000128)
- Hassani, B., Hinton, E., 1998. A review of homogenization and topology optimization I—homogenization theory for media with periodic structure. *Comput. Struct.* 69, 707–717. [https://doi.org/10.1016/S0045-7949\(98\)00131-X](https://doi.org/10.1016/S0045-7949(98)00131-X)

- Hossain, M.M., Ali, S.S., Azadur Rahman, M., 1997. Properties of masonry constituents. *J. Civ. Eng.* 25, 135–155.
- ICC Evaluation Service, 2013. Acceptance criteria for masonry and concrete strengthening using fiber-reinforced cementitious matrix (FRCM) composite systems AC434.
- Indirli, M., Kouris, L.A.S., Formisano, A., Borg, R.P., Mazzolani, F.M., 2013. Seismic damage assessment of unreinforced masonry structures after the Abruzzo 2009 earthquake: The case study of the historical centers of L'Aquila and Castelvechio Subequo. *Int. J. Archit. Herit.* 7, 536–578. <https://doi.org/10.1080/15583058.2011.654050>
- Ismail, N., Ingham, J.M., 2016. In-plane and out-of-plane testing of unreinforced masonry walls strengthened using polymer textile reinforced mortar. *Eng. Struct.* 118, 167–177. <https://doi.org/10.1016/j.engstruct.2016.03.041>
- Ismail, N., Ingham, J.M., 2014. Polymer textiles as a retrofit material for masonry walls. *Proc. Inst. Civ. Eng. - Struct. Build.* 167, 15–25. <https://doi.org/10.1680/stbu.11.00084>
- ISO, 2017. ISO 52000-1:2017 Energy performance of buildings — Overarching EPB assessment — Part 1: General framework and procedures. ISO.
- Jelle, B.P., 2011. Traditional, state-of-the-art and future thermal building insulation materials and solutions - Properties, requirements and possibilities. *Energy Build.* <https://doi.org/10.1016/j.enbuild.2011.05.015>
- Kadam, S.B., Singh, Y., Li, B., 2015. Out-of-plane behaviour of unreinforced masonry strengthened using ferrocement overlay. *Mater. Struct. Constr.* 48, 3187–3203. <https://doi.org/10.1617/s11527-014-0390-8>
- Kakoulaki, G., Maduta, C., Tsionis, G., Zangheri, P., Bavetta, M., 2023. Identification of vulnerable EU regions considering asbestos presence and seismic risk. EUR 31550 EN, Publications Office of the European Union, Luxembourg, 2023, ISBN 978-92-68-04254-0, doi:10.2760/652785, JRC133139.
- Kallioras, S., Bournas, D., Smirolfo, F., Giongo, I., Piazza, M., Molina, F.J., 2024. Cross-laminated timber for seismic retrofitting of RC buildings: Substructured pseudodynamic tests on a full-scale prototype. *Earthq. Eng. Struct. Dyn.* e4222. <https://doi.org/10.1002/eqe.4222>
- Kappos, A.J., Lekidis, V., Panagopoulos, G., Sous, I., Theodulidis, N., Karakostas, C., Anastasiadis, T., Salonikios, T., Margaris, B., 2007. Analytical estimation of economic loss for buildings in the area struck by the 1999 Athens earthquake and comparison with statistical repair costs. *Earthq. Spectra* 23, 333–355. <https://doi.org/10.1193/1.2720366>
- Kappos, A.J., Panagopoulos, G., Panagiotopoulos, C., Penelis, G., 2006. A hybrid method for the vulnerability assessment of R/C and URM buildings. *Bull. Earthq. Eng.* 4, 391–413. <https://doi.org/10.1007/s10518-006-9023-0>
- Kariou, F.A., Triantafyllou, S.P., Bournas, D.A., Koutas, L.N., 2018. Out-of-plane response of masonry walls strengthened using textile-mortar system. *Constr. Build. Mater.* 165, 769–781. <https://doi.org/10.1016/j.conbuildmat.2018.01.026>
- Kaushik, H.B., Rai, D.C., Jain, S.K., 2007. Stress-Strain Characteristics of Clay Brick Masonry under Uniaxial Compression. *J. Mater. Civ. Eng.* 19, 728–739. [https://doi.org/10.1061/\(ASCE\)0899-1561\(2007\)19:9\(728\)](https://doi.org/10.1061/(ASCE)0899-1561(2007)19:9(728))
- Kingery, C.N., Bulmash, G., 1984. Air blast parameters from TNT spherical air burst and hemispherical surface burst. US Army Ballistic Research Laboratory technical report ARBRL-TR 02555. Defence Technology Information Center, Ballistic Research Laboratory, Aberdeen Proving Ground, Maryland.
- Kouris, L.A., Valsamos, G., Triantafyllou, S., Karlos, V., Pohoryles, D.A., Bournas, D.A., Larcher, M., Casadei, F., 2020. Protection of masonry structures against explosions applying layers of textile reinforced mortar, in: Papadrakakis, M., Fragiadakis, M., Papadimitriou, C. (Eds.), *Proceedings of the International Conference on Structural Dynamic, EUROLYN*. Athens, pp. 2573–2584. <https://doi.org/10.47964/1120.9209.20157>
- Kouris, L.A.S., Borg, R.P., Indirli, M., 2010. The L'Aquila Earthquake, April 6th, 2009: a review of seismic damage mechanisms, in: Mazzolani, F.M. (Ed.), *COST ACTION C26: Urban Habitat*

- Constructions under Catastrophic Events - Proceedings of the Final Conference. Taylor & Francis Group, London, pp. 673–681.
- Kouris, L.A.S., Bournas, D.A., Akintayo, O.T., Konstantinidis, A.A., Aifantis, E.C., 2020. A gradient elastic homogenisation model for brick masonry. *Eng. Struct.* 208, 110311. <https://doi.org/10.1016/j.engstruct.2020.110311>
- Kouris, L.A.S., Kappos, A.J., 2015. Fragility curves and loss estimation for traditional timber-framed masonry buildings in Lefkas, Greece, in: *Computational Methods in Applied Sciences*. Springer Netherland, pp. 199–233. <https://doi.org/10.1007/978-3-319-16130-3-8>
- Kouris, L.A.S., Kappos, A.J., 2012. Detailed and simplified non-linear models for timber-framed masonry structures. *J. Cult. Herit.* 13, 47–58. <https://doi.org/10.1016/j.culher.2011.05.009>
- Kouris, L.A.S., Meireles, H., Bento, R., Kappos, A.J., 2014. Simple and complex modelling of timber-framed masonry walls in Pombalino buildings. *Bull. Earthq. Eng.* 12, 1–27. <https://doi.org/10.1007/s10518-014-9586-0>
- Kouris, L.A.S., Triantafyllou, T.C., 2018. State-of-the-art on strengthening of masonry structures with textile reinforced mortar (TRM). *Constr. Build. Mater.* 188, 1221–1233. <https://doi.org/10.1016/j.conbuildmat.2018.08.039>
- Kouris, L.A.S., Triantafyllou, S.P., Bournas, D.A., Kariou, F.A., 2023. Empirical Equations for Modelling Yarn–Mortar Debonding in TRM-Strengthened Masonry Walls Subjected to Out-of-Plane Loading. *Buildings* 14, 32. <https://doi.org/10.3390/buildings14010032>
- Koutas, L., Triantafyllou, T., Bousias, S., 2014. Analytical Modeling of Masonry-Infilled RC Frames Retrofitted with Textile-Reinforced Mortar. *J. Compos. ...* 19, 1–14. [https://doi.org/10.1061/\(ASCE\)CC.1943-5614.0000553](https://doi.org/10.1061/(ASCE)CC.1943-5614.0000553).
- Koutas, L.N.L.N., Tetta, Z., Bournas, D.A.D.A., Triantafyllou, T.C.T.C., 2019. Strengthening of Concrete Structures with Textile Reinforced Mortars: State-of-the-Art Review. *J. Compos. Constr.* 23, 03118001. [https://doi.org/10.1061/\(ASCE\)CC.1943-5614.0000882](https://doi.org/10.1061/(ASCE)CC.1943-5614.0000882)
- Krevaikas, T.D., Triantafyllou, T.C., 2005. Computer-aided strengthening of masonry walls using fibre-reinforced polymer strips. *Mater. Struct. Constr.* 38, 93–98. <https://doi.org/10.1617/14116>
- Kristoffersen, M., Hauge, K.O., Valsamos, G., Børvik, T., 2018. Blast loading of concrete pipes using spherical centrally placed C-4 charges. *EPJ Web Conf.* 183. <https://doi.org/10.1051/epjconf/201818301057>
- Lagomarsino, S., Penna, A., Galasco, A., Cattari, S., 2013. TREMURI program: An equivalent frame model for the nonlinear seismic analysis of masonry buildings. *Eng. Struct.* 56, 1787–1799. <https://doi.org/10.1016/j.engstruct.2013.08.002>
- Larrinaga, P., Chastre, C., Biscaia, H.C., San-José, J.T., 2014. Experimental and numerical modeling of basalt textile reinforced mortar behavior under uniaxial tensile stress. *Mater. Des.* 55, 66–74. <https://doi.org/10.1016/j.matdes.2013.09.050>
- Llorens, J., Llorens, M., Chamorro, M.A., Soler, J., 2019. Experimental Behavior of Brick Masonry under Uniaxial Compression on Parallel-to-Face Brick. Single-Leaf Case Study. *Int. J. Archit. Herit.* 1–15. <https://doi.org/10.1080/15583058.2018.1503361>
- Longo, F., Lassandro, P., Moshiri, A., Phatak, T., Aiello, M.A., Krakowiak, K.J., 2020. Lightweight geopolymer-based mortars for the structural and energy retrofit of buildings. *Energy Build.* 225. <https://doi.org/10.1016/j.enbuild.2020.110352>
- Lourenço, P.B., 2000. Anisotropic softening model for masonry plates and shells. *J. Struct. Eng. N. Y.* N 126, 1008–1016. [https://doi.org/10.1061/\(ASCE\)0733-9445\(2000\)126:9\(1008\)](https://doi.org/10.1061/(ASCE)0733-9445(2000)126:9(1008))
- Lourenço, P.B., Ramos, L.F., 2004. Characterization of cyclic behavior of dry masonry joints. *J Struct Eng* 130, 779–786. [https://doi.org/10.1061/\(ASCE\)0733-9445\(2004\)130:5\(779\)](https://doi.org/10.1061/(ASCE)0733-9445(2004)130:5(779))
- Lubliner, J., Oliver, J., Oller, S., Oñate, E., 1989. A plastic-damage model for concrete. *Int. J. Solids Struct.* [https://doi.org/10.1016/0020-7683\(89\)90050-4](https://doi.org/10.1016/0020-7683(89)90050-4)
- Maduta, C., D’Agostino, D., Tsemekidi-Tzeiranaki, S., Castellazzi, L., Melica, G., Bertoldi, P., 2023. Towards climate neutrality within the European Union: Assessment of the Energy Performance of Buildings Directive implementation in Member States. *Energy Build.* 301, 113716. <https://doi.org/10.1016/j.enbuild.2023.113716>

- Maduta, C., Melica, G., D'Agostino, D., Bertoldi, P., 2022. Towards a decarbonised building stock by 2050: The meaning and the role of zero emission buildings (ZEBs) in Europe. *Energy Strategy Rev.* 44, 101009. <https://doi.org/10.1016/j.esr.2022.101009>
- Maio, R., Vicente, R., Formisano, A., Varum, H., 2015. Seismic vulnerability of building aggregates through hybrid and indirect assessment techniques. *Bull. Earthq. Eng.* <https://doi.org/10.1007/s10518-015-9747-9>
- Makashev, K., Triantafyllou, S.P., Thermou, G.E., Tizani, W., 2023. Bond behaviour of light and heavy carbon fibre TRM to masonry interfaces. *Constr. Build. Mater.* 400, 132508. <https://doi.org/10.1016/J.CONBUILDMAT.2023.132508>
- Marcari, G., Basili, M., Vestroni, F., 2017. Experimental investigation of tuff masonry panels reinforced with surface bonded basalt textile-reinforced mortar. *Compos. Part B Eng.* 108, 131–142. <https://doi.org/10.1016/j.compositesb.2016.09.094>
- Martins, A., Vasconcelos, G., Figueiro, R., Cunha, F., 2015. Experimental assessment of an innovative strengthening material for brick masonry infills. *Compos. Part B Eng.* 80, 328–342. <https://doi.org/10.1016/j.compositesb.2015.06.012>
- Mechtcherine, V., Schneider, K., Brameshuber, W., 2016. Mineral-Based Matrices for Textile-Reinforced Concrete, *Textile Fibre Composites in Civil Engineering.* <https://doi.org/10.1016/B978-1-78242-446-8.00003-3>
- Mousavi, S.M., Aifantis, E.C., 2016. Dislocation-based gradient elastic fracture mechanics for in-plane analysis of cracks. *Int. J. Fract.* 202, 93–110. <https://doi.org/10.1007/s10704-016-0143-5>
- NUMBEO, 2019. Europe: Prices by City of Price per Square Meter to Buy Apartment in City Centre (Buy Apartment Price) [WWW Document]. URL https://www.numbeo.com/cost-of-living/region_prices_by_city?itemId=100®ion=150 (accessed 11.15.20).
- Nwofor, T., 2012. Experimental Determination of the Mechanical Properties of Clay Brick Masonry. *Can. J. Environ. Constr. Civ. Eng.* 3, 127–145.
- Oliveira, D. V., Lourenço, P.B., Roca, P., 2007. Cyclic behaviour of stone and brick masonry under uniaxial compressive loading. *Mater. Struct.* 39, 247–257. <https://doi.org/10.1617/s11527-005-9050-3>
- Olivito, R.S., Cevallos, O.A., Carrozzini, A., 2014. Development of durable cementitious composites using sisal and flax fabrics for reinforcement of masonry structures. *Mater. Des.* 57, 258–268. <https://doi.org/10.1016/J.MATDES.2013.11.023>
- Olivito, R.S., Codispoti, R., Cevallos, O.A., 2016. Bond behavior of Flax-FRCM and PBO-FRCM composites applied on clay bricks: Experimental and theoretical study. *Compos. Struct.* 146, 221–231. <https://doi.org/10.1016/j.compstruct.2016.03.004>
- Padalu, P.K.V.R., Singh, Y., Das, S., 2019. Out-of-plane flexural behaviour of masonry wallettes strengthened using FRP composites and externally bonded grids: Comparative study. *Compos. Part B Eng.* 176, 107302. <https://doi.org/10.1016/J.COMPOSITESB.2019.107302>
- Pande, G.N., Liang, J.X., Middleton, J., 1989. Equivalent elastic moduli for brick masonry. *Comput. Geotech.* 8, 243–265. [https://doi.org/10.1016/0266-352X\(89\)90045-1](https://doi.org/10.1016/0266-352X(89)90045-1)
- Papanicolaou, C., Triantafillou, T., Lekka, M., 2011. Externally bonded grids as strengthening and seismic retrofitting materials of masonry panels. *Constr. Build. Mater.* 25, 504–514. <https://doi.org/10.1016/j.conbuildmat.2010.07.018>
- Papanicolaou, C.G., Triantafillou, T.C., Karlos, K., Papathanasiou, M., 2007. Textile-reinforced mortar (TRM) versus FRP as strengthening material of URM walls: in-plane cyclic loading. *Mater. Struct.* 40, 1081–1097. <https://doi.org/10.1617/s11527-006-9207-8>
- Papanicolaou, C.G., Triantafillou, T.C., Papathanasiou, M., Karlos, K., 2008. Textile reinforced mortar (TRM) versus FRP as strengthening material of URM walls: Out-of-plane cyclic loading. *Mater. Struct.* 41, 143–157.
- Parisi, F., Lignola, G.P., Augenti, N., Prota, A., Manfredi, G., 2011. Nonlinear Behavior of a Masonry Subassemblage Before and After Strengthening with Inorganic Matrix-Grid Composites. *J. Compos. Constr.* 15, 821–832. [https://doi.org/10.1061/\(ASCE\)CC.1943-5614.0000203](https://doi.org/10.1061/(ASCE)CC.1943-5614.0000203)

- Penelis, G.G., 2006. An efficient approach for pushover analysis of unreinforced masonry (URM) structures. *J. Earthq. Eng.* 10, 359–379. <https://doi.org/10.1142/S136324690600258X>
- Penna, A., Lagomarsino, S., Galasco, A., 2014a. A nonlinear macroelement model for the seismic analysis of masonry buildings. *Earthq. Eng. Struct. Dyn.* 43, 159–179. <https://doi.org/10.1002/eqe.2335>
- Penna, A., Morandi, P., Rota, M., Manzini, C.F., da Porto, F., Magenes, G., 2014b. Performance of masonry buildings during the Emilia 2012 earthquake. *Bull. Earthq. Eng.* 12, 2255–2273. <https://doi.org/10.1007/s10518-013-9496-6>
- Pohoryles, D.A., Bournas, D.A., 2021. IRESIST+, innovative seismic and energy retrofitting of the existing building stock – Numerical simulations and impact assessment, EUR 30583 EN. <https://doi.org/10.2760/768985>
- Pohoryles, D.A., Bournas, D.A., 2020. Seismic retrofit of infilled RC frames with textile reinforced mortars: State-of-the-art review and analytical modelling. *Compos. Part B Eng.* <https://doi.org/10.1016/j.compositesb.2019.107702>
- Pohoryles, D.A., Bournas, D.A., Da Porto, F., Caprino, A., Santarsiero, G., Triantafillou, T., 2022. Integrated seismic and energy retrofitting of existing buildings: A state-of-the-art review. *J. Build. Eng.* 61, 105274. <https://doi.org/10.1016/j.jobe.2022.105274>
- Pohoryles, D.A., Maduta, C., Bournas, D.A., Kouris, L.A., 2020. Energy Performance of Existing Residential Buildings in Europe: A Novel Approach Combining Energy with Seismic Retrofitting. *Energy Build.* 223, 110024. <https://doi.org/10.1016/j.enbuild.2020.110024>
- Polizzotto, C., 2018. A micromorphic approach to stress gradient elasticity theory with an assessment of the boundary conditions and size effects. *ZAMM Z. Angew. Math. Mech.* 98, 1528–1553. <https://doi.org/10.1002/zamm.201700364>
- Polizzotto, C., 2003. Gradient elasticity and nonstandard boundary conditions. *Int. J. Solids Struct.* 40, 7399–7423. <https://doi.org/10.1016/J.IJSOLSTR.2003.06.001>
- Prota, A., Marcari, G., Fabbrocino, G., Manfredi, G., Aldea, C., 2006. Experimental In-Plane Behavior of Tuff Masonry Strengthened with Cementitious Matrix–Grid Composites. *J. Compos. Constr.* 10, 1081–1097. [https://doi.org/10.1061/\(ASCE\)1090-0268\(2006\)10:3\(223\)](https://doi.org/10.1061/(ASCE)1090-0268(2006)10:3(223))
- Raouf, S.M., Koutas, L.N., Bournas, D.A., 2016. Bond between textile-reinforced mortar (TRM) and concrete substrates: Experimental investigation. *Compos. Part B Eng.* 98, 350–361. <https://doi.org/10.1016/j.compositesb.2016.05.041>
- Reddy, B.V.V., Lal, R., Rao, K.S.N., 2009. Influence of Joint Thickness and Mortar-Block Elastic Properties on the Strength and Stresses Developed in Soil-Cement Block Masonry. *J. Mater. Civ. Eng.* 21, 535–542. [https://doi.org/10.1061/\(ASCE\)0899-1561\(2009\)21:10\(535\)](https://doi.org/10.1061/(ASCE)0899-1561(2009)21:10(535))
- Rossi, M., Bournas, D., 2023. Structural Health Monitoring and Management of Cultural Heritage Structures: A State-of-the-Art Review. *Appl. Sci.* 2023 Vol 13 Page 6450 13, 6450. <https://doi.org/10.3390/APP13116450>
- Ru, C.Q., Aifantis, E.C., 1993. A simple approach to solve boundary-value problems in gradient elasticity. *Acta Mech.*
- Sagar, S.L., Singhal, V., Rai, D.C., Gudur, P., 2017. Diagonal Shear and Out-of-Plane Flexural Strength of Fabric-Reinforced Cementitious Matrix–Strengthened Masonry Wall. *J. Compos. Constr.* 21, 04017016. [https://doi.org/10.1061/\(ASCE\)CC.1943-5614.0000796](https://doi.org/10.1061/(ASCE)CC.1943-5614.0000796)
- Shermi, C., Dubey, R.N., 2017. Study on out-of-plane behaviour of unreinforced masonry strengthened with welded wire mesh and mortar. *Constr. Build. Mater.* 143, 104–120. <https://doi.org/10.1016/j.conbuildmat.2017.03.002>
- Stupkiewicz, S., Mróz, Z., 2001. Modelling of friction and dilatancy effects at brittle interfaces for monotonic and cyclic loading | Stupkiewicz | *Journal of Theoretical and Applied Mechanics. J. Theor. Appl. Mech.* 39, 707–739.
- Taliercio, A., 2014. Closed-form expressions for the macroscopic in-plane elastic and creep coefficients of brick masonry. *Int. J. Solids Struct.* 51, 2949–2963. <https://doi.org/10.1016/j.ijsolstr.2014.04.019>

- Tomazevic, M., 1999. Earthquake-Resistant Design of Masonry Buildings, Series on Innovation in Structures and Construction. Published by Imperial College Press and Distributed By World Scientific Publishing Co. <https://doi.org/10.1142/p055>
- Triantafillou, T.C., 2016. Strengthening of existing masonry structures: concepts and structural behavior, Textile Fibre Composites in Civil Engineering. <https://doi.org/10.1016/B978-1-78242-446-8.00016-1>
- Triantafillou, Thanasis C., 2016. Strengthening of Existing Masonry Structures: Design Models, Textile Fibre Composites in Civil Engineering. <https://doi.org/10.1016/B978-1-78242-446-8.00017-3>
- Triantafillou, T.C., 1998. Strengthening of masonry structures using epoxy-bonded FRP laminates. *J. Compos. Constr.* 2, 96–104.
- Triantafillou, T.C., Karlos, K., Kapsalis, P., Georgiou, L., 2018. Innovative Structural and Energy Retrofitting System for Masonry Walls Using Textile Reinforced Mortars Combined with Thermal Insulation: In-Plane Mechanical Behavior. *J. Compos. Constr.* 22, 04018029. [https://doi.org/10.1061/\(ASCE\)CC.1943-5614.0000869](https://doi.org/10.1061/(ASCE)CC.1943-5614.0000869)
- Triantafillou, T.C., Karlos, K., Kefalou, K., Argyropoulou, E., 2017. An innovative structural and energy retrofitting system for URM walls using textile reinforced mortars combined with thermal insulation: Mechanical and fire behavior. *Constr. Build. Mater.* 133, 1–13. <https://doi.org/10.1016/J.CONBUILDMAT.2016.12.032>
- Tsepoura, K.G., Papargyri-Beskou, S., Polyzos, D., Beskos, D.E., 2002. Static and dynamic analysis of a gradient-elastic bar in tension. *Arch. Appl. Mech.* 72, 483–497. <https://doi.org/10.1007/s00419-002-0231-z>
- US Department of Energy, 2010. EnergyPlus Engineering Reference: The Reference to EnergyPlus Calculations. US Dep. Energy.
- Valluzzi, M.R., da Porto, F., Garbin, E., Panizza, M., 2014. Out-of-plane behaviour of infill masonry panels strengthened with composite materials. *Mater. Struct. Constr.* 47, 2131–2145. <https://doi.org/10.1617/s11527-014-0384-6>
- Veljkovic, A., Carvelli, V., Rezazadeh, M., 2020. Modelling the bond in GFRP bar reinforced concrete thin structural members. *Structures* 24, 13–26. <https://doi.org/10.1016/j.istruc.2019.12.027>
- Veljkovic, A., Pohoryles, D.A., Bournas, D.A., 2023. Heating energy demand estimation of the EU building stock: Combining building physics and artificial neural networks. *Energy Build.* 298, 113474. <https://doi.org/10.1016/J.ENBUILD.2023.113474>
- Vermeltoort, A.T., Martens, D.R.W., van Zijl, G.P.A.G., 2007. Brick–mortar interface effects on masonry under compression This article is one of a selection of papers published in this Special Issue on Masonry. *Can. J. Civ. Eng.* 34, 1475–1485. <https://doi.org/10.1139/L07-067>
- Zangheri, P., Armani, R., Kakoulaki, G., Bavetta, M., Martirano, G., Pignatelli, F., Baranzelli, C., 2020. Building energy renovation for decarbonisation and Covid-19 recovery, EUR 30433 EN, Publications Office of the European Union, Luxembourg, 2020, ISBN 978-92-76-24766-1, doi:10.2760/08629, JRC122143.

List of abbreviations and definitions

DOF	Degree of Freedom
EAL	Expected Annual Losses
EPBD	2010 Energy Performance of Buildings Directive
FE	Finite Element
FRP	Fiber Reinforced Polymer
GREHM	GRadiEnt Homogenisation Model
HDD	Heating Degree-Days
NZEB	Nearly Zero-Energy Buildings
ODE	Ordinary Differential Equation
PDE	Partial Differential Equation
PGA	Peak Ground Acceleration
RSE	Representative Shell Element
RVE	Representative Volume Element
TRM	Textile Reinforced Mortar
URM	UnReinforced Masonry

List of boxes

Box 1. Advantage of TRM over FRP for retrofitting masonry buildings 5

Box 2. Boost EU policies implementation 6

Box 3. TRM strengthened masonry elements 9

Box 4. The thermo-structural hybrid retrofitting of masonry elements10

Box 5. Homogenisation model for masonry walls11

Box 6. Implicit and explicit models29

Box 7. Implementation of a simultaneous seismic + energy retrofitting of buildings in Europe57

List of figures

Figure 1. Seismic plus energy retrofitting system: (a) TRM Jacket + insulation material on a masonry wall; (b) TRM + heating system on the masonry infill of RC framed structure.....	5
Figure 2. Response of TRM in tension: experimental behaviour and trilinear idealisation.	8
Figure 3. The homogenised modelling approach for masonry using the representative volume element; in blue the interaction interfaces.	12
Figure 4. Axial 1-D gradient elastic element.	13
Figure 5. The representative surface element (RSE) of running bond brickwork: (a) on the wall, (b) a close-up.	14
Figure 6. The (normalised) vertical elastic modulus E_v of masonry in respect to t_{my} / t_{by} for various ratios of E_m/E_b and ℓ/t_{my}	17
Figure 8. The (normalised) shear elastic modulus G of masonry in respect to t_{my} / t_{by} for various ratios of E_m/E_b and ℓ/t_{my}	18
Figure 9. The Poisson's ratio ν_{yx} of masonry in respect to t_{my} / t_{by} for various ratios of E_m/E_b and ℓ/t_{my}	19
Figure 10. The influence of the internal length normalised against the thickness of mortar joints on (a) the horizontal and vertical elastic moduli and (b) the shear modulus (normalised against the brick elastic modulus) and, (c) the Poisson's ratio of the homogenised model.....	20
Figure 11. The FE model of the RSE: (a) model, (b) shear displacements, (c) shear strain, and (d) shear stress.	21
Figure 12. FEM of the wall: (a) the wall configuration, (b) mesh of the wall.....	22
Figure 13. Comparison between the (Mises) stress field in kPa of the distinct-properties model Γ_d (on the left) and GREHM model Γ_h (on the right) for a vertical (a,b), horizontal (c,d) and moment (e,f) load.	23
Figure 14. The influence of the internal length on the accuracy of the model for three different loading conditions.	24
Figure 15. Comparison of vertical elastic modulus E_v between the proposed GREHM and the models of (Taliercio, 2014), (Di Nino and Luongo, 2019), and (Pande, Liang, and Middleton, 1989) for the considered experimental values E_{exp} : the red dashed lines at $\pm 10\%$	26
Figure 16. A comparison between GREHM and the models of Taliercio (Taliercio, 2014), Di Nino and Luongo (Di Nino and Luongo, 2019), and Pande et al. (Pande, Liang, and Middleton, 1989) for the elastic modulus in the horizontal direction E_h , the shear modulus G and the Poisson ratio ν_{xy}	27
Figure 17. The modelling approach for bond slip phenomena in TRM: (a) a linear textile response, (b) a bilinear bonding response, and (c) the effective linear textile response.	30
Figure 18. The stress-plastic strain curve of masonry.	31
Figure 19. Comparison of the out-of-plane response of the unreinforced double wythe specimen with the analytical model.....	33
Figure 20. Comparison of the out-of-plane response of the reinforced single wythe specimen with the analytical model.....	34
Figure 21. Comparison of the out-of-plane response of the reinforced double wythe specimen with the analytical model.....	35
Figure 22. Experimental vs. estimated values of Ω	37
Figure 23. The variation of Ω_E vs. α and β coefficients.....	37
Figure 24. Textile properties for parametric analyses with varying mechanical ratios combining a range of textile strengths, yarn area (area of the points), and number of layers (colour of the points, see colourbar). .39	

Figure 25. Maximum vertical load of piers out-of-plane loaded for 3 levels of vertical load: (a) $N = 0$, (b) $N = 10\% f_m$, and (c) $N = 20\% f_m$	39
Figure 27. Comparison between experimental results of single (S_C1) and double wythe (D_C1) masonry and numerical model (EPX).....	42
Figure 28. Failure mode of experimental specimens and analytical representation.....	42
Figure 30. Damage states for: (a) unreinforced masonry, and (b) retrofitted masonry with TRM.	44
Figure 33. Expected annual savings (%) after retrofitting per energy zone: (i) energy, (ii) seismic, and (iii) combined.	51
Figure 34. Fragility curves for stone URM and RMB buildings.	53
Figure 35. Vulnerability curves for stone and low/medium rise brick masonry buildings and their strengthened counterparts.	54
Figure 36. Annual probability of exceedance vs. ground acceleration for Faro.	55
Figure 37. Payback periods in years per seismic zone: (i) energy, (ii) seismic, and (iii) combined.	56
Figure 38. Average combined classification in terms of EAL of the building stock across all seismic and climatic zones.	57

List of tables

Table 1. Material properties: elastic modulus [GPa] and strength [MPa].10

Table 2. Properties of brick units and mortar joints for GREHM.20

Table 3. Results from the FE analysis of the RSE and homogenised mechanical properties.22

Table 4. Experimental testing of masonry walls: main parameters of brick units and mortar joints (continued).
.....25

Table 5. Experimental testing of masonry walls: main parameters of brick units and mortar joints.26

Table 6. Calibrated coefficients p_1 , p_2 , p_3 and regression metrics of the empirical Eq. (22).37

Table 7. Experimental parameters.38

Table 8. Material parameters for brittle constitutive law.41

Table 9. Effective material parameters for the carbon TRM layer.41

Table 10. Matrix of case study cities by seismic risk (PGA) and climatic condition (HDD).45

Figure 31. Relative proportion of masonry and RC building per location.47

Figure 32. Relative proportion of masonry building types per location.48

Table 12. Wall characteristics of the masonry buildings.49

Table 13. Target U-values in each case-study location.50

Table 14. Target seismic design level of the seismic retrofit scheme.52

Getting in touch with the EU

In person

All over the European Union there are hundreds of Europe Direct centres. You can find the address of the centre nearest you online (european-union.europa.eu/contact-eu/meet-us_en).

On the phone or in writing

Europe Direct is a service that answers your questions about the European Union. You can contact this service:

- by freephone: 00 800 6 7 8 9 10 11 (certain operators may charge for these calls),
- at the following standard number: +32 22999696,
- via the following form: european-union.europa.eu/contact-eu/write-us_en.

Finding information about the EU

Online

Information about the European Union in all the official languages of the EU is available on the Europa website (european-union.europa.eu).

EU publications

You can view or order EU publications at op.europa.eu/en/publications. Multiple copies of free publications can be obtained by contacting Europe Direct or your local documentation centre (european-union.europa.eu/contact-eu/meet-us_en).

EU law and related documents

For access to legal information from the EU, including all EU law since 1951 in all the official language versions, go to EUR-Lex (eur-lex.europa.eu).

EU open data

The portal data.europa.eu provides access to open datasets from the EU institutions, bodies and agencies. These can be downloaded and reused for free, for both commercial and non-commercial purposes. The portal also provides access to a wealth of datasets from European countries.

Science for policy

The Joint Research Centre (JRC) provides independent, evidence-based knowledge and science, supporting EU policies to positively impact society



EU Science Hub

[Joint-research-centre.ec.europa.eu](https://joint-research-centre.ec.europa.eu)



Publications Office
of the European Union